Title

EOS: A TIME PROJECTION CHAMBER FOR THE STUDY OF NUCLEUS-NUCLEUS COLLISIONS AT THE BEVALAC

Author

Pugh, H.G.

Publication Date

1986-12-01

LBL-22314
UC-34C

Lawrence Berkeley Laboratory
UNIVERSITY OF CALIFORNIA

EOS: A TIME PROJECTION CHAMBER FOR THE STUDY OF NUCLEUS-NUCLEUS COLLISIONS AT THE BEVALAC

H.G. Pugh, G. Odyniec, G. Rai, and P. Seidl

December 1986

NUCLEAR SCIENCE DIVISION

Prepared for the U.S. Department of Energy under Contract DE-AC03-76SF00098

DISCLAIMER

LBL-22314

EOS*:

A TIME PROJECTION CHAMBER FOR THE STUDY OF NUCLEUS-NUCLEUS COLLISIONS AT THE BEVALAC

H. G. Pugh, G. Odyniec, G. Rai and P. Seidl
Lawrence Berkeley Laboratory
University of California
Berkeley, California 94720

December 1986

*Greek: Goddess of the Dawn. As an acronym, EOS stands for the Equation Of State of nuclear matter. The connection between the two is suggested by the book "EOS, or the Wider Aspects of Cosmogony", by J. H. Jeans, F.R.S., Kegan Paul, Trench, Tribner & Co. Ltd., London, 1931, which explores the relationship between the structure of matter and the creation of the universe.

This work was supported by the Director, Office of Energy Research,
Division of Nuclear Physics of the Office of High Energy and Nuclear Physics
of the U.S. Department of Energy under Contract DE-AC03-76SF00098

LBL-22314

EOS*:

A TIME PROJECTION CHAMBER FOR THE STUDY OF NUCLEUS-NUCLEUS COLLISIONS AT THE BEVALAC

H. G. Pugh, G. Odyniec, G. Rai and P. Seidl
Lawrence Berkeley Laboratory
University of California
Berkeley, California 94720

ABSTRACT

The conceptual design is presented for a detector to identify and measure ($\Delta p/p \simeq 1\%$) most of the 200 or so mid-rapidity charged particles (p, d, t, ^{3}He, ^{4}He, $\pi^\pm$, $K^\pm$) produced in each central nucleus-nucleus collision (Au + Au) at Bevalac energies, as well as K_s^o and Λ^0. The beam particles and heavy spectator fragments are excluded from the detection volume by means of a central vacuum pipe. Particle identification is achieved by a combination of dE/dx measurements in the TPC, and of time-of-flight measurements in a scintillator array. The TPC is single-ended and its end cap is entirely covered with cathode pads (about 25,000 pads and about 1000 anode wires). A non-uniform pad distribution is proposed to accommodate the high multiplicity of particles emitted at forward angles. The performance of the detector is assessed with regard to multihit capability, tracking, momentum resolution, particle identification, Λ^0 reconstruction, space charge effects, field non-uniformity, dynamic range, data acquisition rate, and data analysis rate.

Table of Contents

[†] The appendices referred to in the text are available upon request.

Chapter 1

1. Introduction

1.1. Objectives

The energy regime of the Bevalac is ideal for the study of the equation of state of nuclear matter at high densities. This is important for understanding nuclear matter under extreme conditions that are relevant for astrophysical objects such as supernovae and neutron stars, and because it tests modern relativistic nuclear theories [AA 86].

Within the very large variety of different types of nucleus-nucleus collisions studied at the Bevalac, the central or near-central collisions of heavy nuclei are most relevant to the nuclear matter equation of state. In these an extended fireball of hot, dense nuclear matter is produced which breaks up with emission of a multitude of created mesons and of light nuclear fragments all of which carry information about conditions reached during the high-density phase of the collision. The studies carried out with the Streamer Chamber and the Plastic Ball have demonstrated that the compressional energy stored in the high-density phase influences the number of negative pions emitted in each collision, while the pressure built up at the interface of the colliding nuclei affects the transverse momenta of the heavy particles in the phenomenon called flow, where a preferential direction of emission has been observed.

The production of strange particles – kaons and lambdas – is a relatively rare occurrence, but of great interest, as they are expected to be a sensitive probe of the high density phase of the fireball.

To pursue these studies systematically and to extend them to new areas suggested by theory, a new detector is needed. This should have essentially 4π coverage in solid angle; it should have the capability of unraveling the most complex events; it should permit the identification of each particle produced, and give its momentum. It should tolerate a high event rate and be capable of being triggered to select events of special interest. Finally, it should be designed to accommodate electronic storage of the data in order to facilitate the most rapid data analysis.

In this report we shall show that the time projection chamber (TPC) technique [AB 83] is well matched to the requirements stipulated above, and we shall present a design for a specific detector: **EOS**.

1.2. The Detector

A schematic layout of the detector is shown in Fig. 1.1. A superconducting solenoid provides a longitudinal magnetic field of 1.5T, in which is located a time projection chamber of diameter 1.8m and length 2.0m. The target is located in an evacuated beam pipe of diameter 20 cm, which passes through the center of the TPC. This beam pipe serves to protect the TPC against the very heavy ionisation which would occur if the beam particles passed through the TPC. It is made

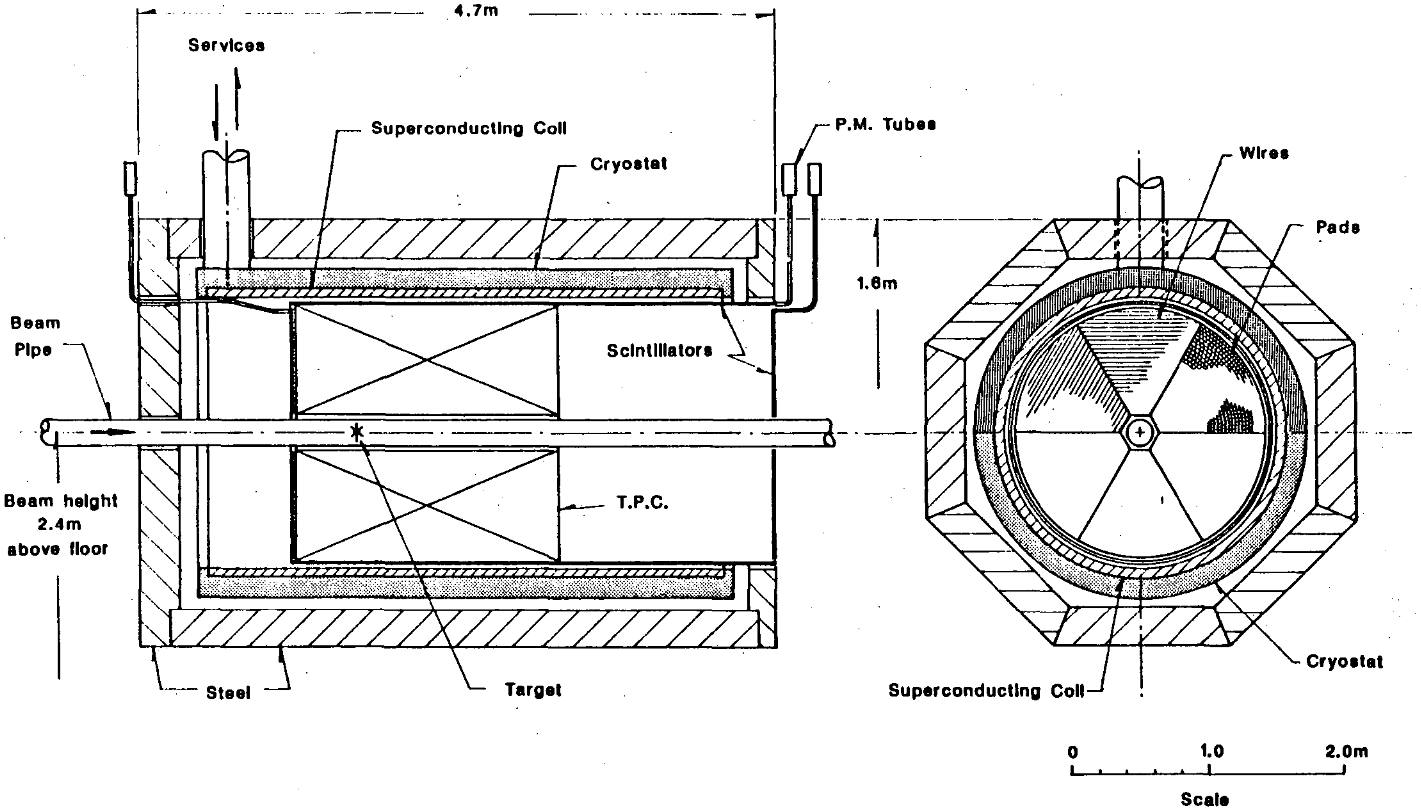

Fig. 1.1. Schematic layout of the EOS detector.

large enough that supplementary detectors can be inserted at a later stage if so desired. The TPC is supplemented by a time-of-flight scintillator array which consists of two parts: the "barrel" scintillators which line the inside of the magnet, and the"downstream" scintillators, which cover the exit face of the magnet.

Figure 1.2 shows a possible location for the EOS detector on the Bevalac floor. This location, in an existing beam line, requires no new shielding, and has sufficient space for supplementary detectors downstream and for the TPC to be pulled out from the magnet on rails.

Figure 1.3 shows a schematic view of the TPC. It consists of a large volume of gas where electrons, produced by ionisation along the particle tracks, drift towards the end cap under the action of parallel electric and magnetic fields. The end cap, constructed in several sectors, is covered with thin-gap multiwire proportional chambers (MWPC). Track localization is achieved by recording with suitable electronics, as a function of time, the charge detected on the anode wires and on rows of pads located behind the anode wires. For each segment of track the drift time (with reference to a common start) provides one coordinate, while the induced signals on the pad rows provide the coordinates in the plane of the MWPC. Since the TPC provides many position measurements along each track and also many samples of dE/dx, it gives excellent momentum measurement and particle identification.

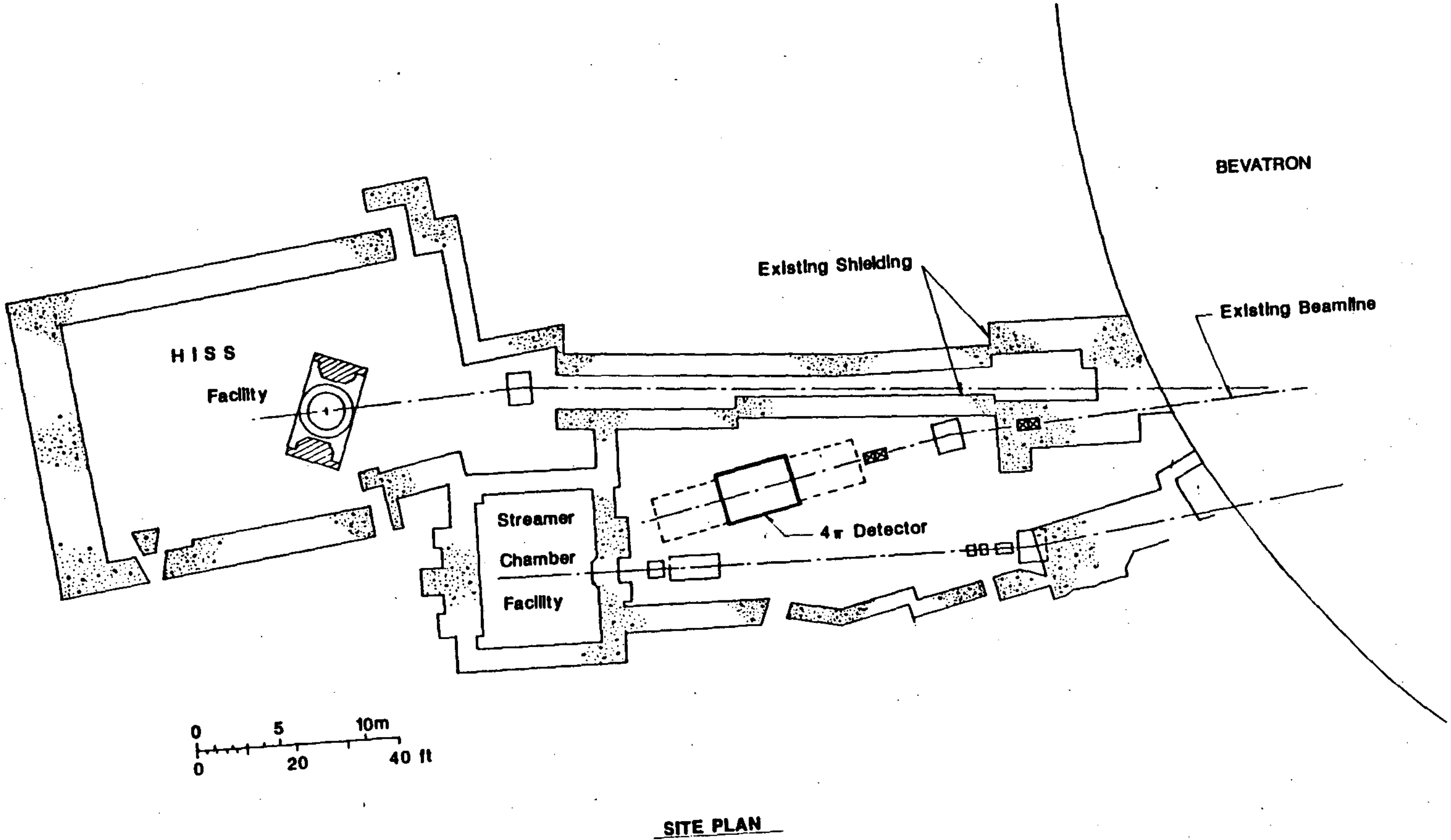

Fig. 1.2. Location of the EOS detector in the BEVALAC experimental hall.

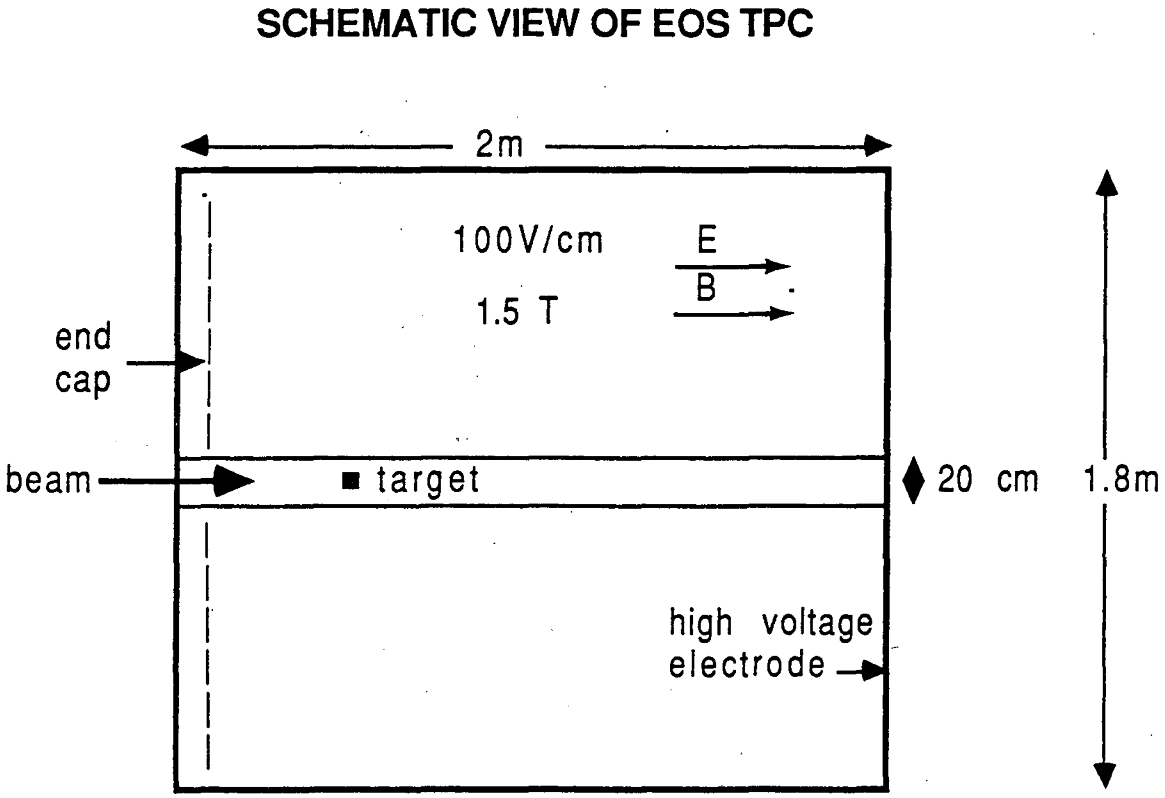

Fig. 1.3. Side view schematic of of the EOS TPC, showing some of the fundamental parameters.

The original TPC, PEP-4, [Cl 76], [Ma 78] was built by a collaboration led by LBL, and it has operated successfully at PEP for several years. Based on its success, the TPC has been chosen as the basis for other major detectors in high-energy physics, particularly the ALEPH [Bl 84], DELPHI [De 84], projects under construction at CERN for experiments at LEP, and TOPAZ [Ka 86] at KEK. The extensive experience acquired with the PEP-4 TPC and the extensive research and development carried out in connection with the new projects provide a firm basis for studying the capabilities of a TPC for the Bevalac. We shall show that such a detector can measure and identify essentially all the charged particles emitted in central collisions, as well as Λ^0 and K^0 particles which decay in the chamber. In order to provide particle identification in the region of the $K-\pi$ and $K-p$ ambiguities (where dE/dx is the same for both particles) we supplement the TPC with a time-of-flight array. This array also provides useful redundancy in particle identification at lower energies, and serves to provide topological triggers for the TPC.

1.3. Performance

Figure 1.4 shows a simulated Au+Au central collision at 1.0 GeV/A, with 200 charged particles. The TPC will be able to measure essentially all the charged particles in such an event, with particle identification close to 100% for heavy particles and pions and better than 80% for Kaons.

Figure 1.5 shows a contour diagram of the invariant cross section $E \cdot (d\sigma/dp^3)$ for production of pions in Ar+KCl central collisions at 1.8 GeV/A,

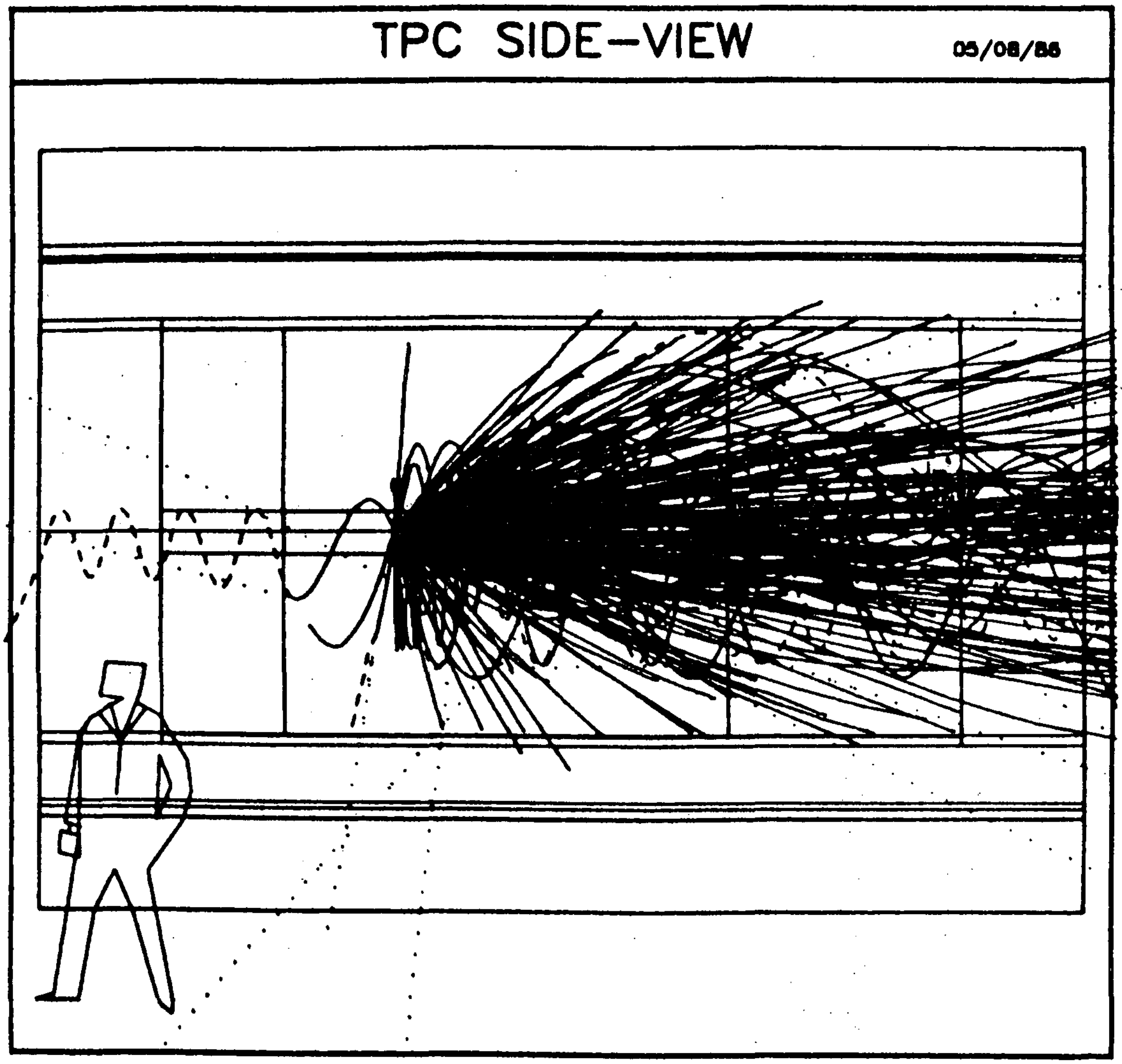

Fig. 1.4. A side view depicting an Au+Au collision at a beam energy of 1.0 GeV/A.

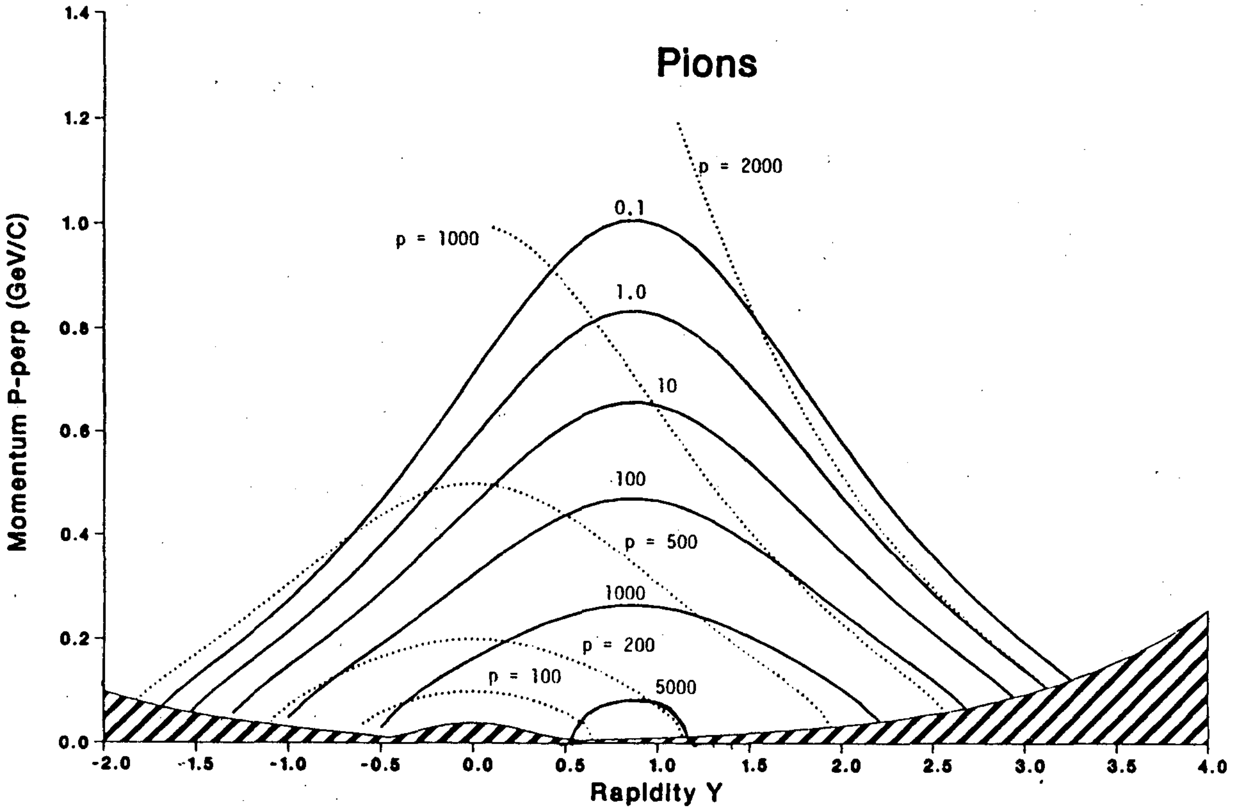

Fig. 1.5. A contour plot of the invariant cross section $E\ d\sigma/dp^3$ of participant pions as a function of transverse momentum and rapidity for central Ar+KCl collisions at 1.8 GeV/A, calculated in the fireball model described in Chapter 3. The shaded area shows the region that is not accessible to measurement due to the beam pipe. Constant laboratory momenta are shown by the dotted lines, in MeV/c. The solid lines show constant $E\ d\sigma/dp^3$ in $mb\ /MeV^2/c^3$.

calculated in a fireball model with parameters adjusted to fit existing experimental data. The shaded area shows the region that is inaccessible due to the diameter and thickness of the beam pipe. Contours are shown down to the level which is accessible in a typical length run and period of data analysis. It is clear that the detector will permit excellent coverage of the fireball regime. Figures 1.6 and 1.7 show similar performance for K^+ and protons.

1.4. Data Rates

The capability of the EOS TPC to generate information is almost overwhelming. As will be shown in Chapter 5, it can operate at an interaction rate of approximately 10^4 per second. To make optimum use of this, selective triggers will be needed, and parallel processing techniques will have to be adopted both in data acquisition and analysis, as discussed later in Chapter 8. Whatever the triggering scheme, the data output is impressive, as will be shown below.

We consider data acquired with a central trigger but no further selection, and analysed by a single CPU at a rate of 0.2 seconds per track,[†] which is consistent with that achieved or projected by similar detectors such as PEP-4 or ALEPH. Table 1.1 shows the output of data analysis at this rate for one month, the amount of time that one might devote to a particular combination of target, projectile and beam energy. The composition of the events is obtained from extrapolation of existing data, as described in Chapter 3. The data in the table

---

[†] This estimate, for track reconstruction using a VAX 11/780 computer, does not include any overhead (which will be substantial) for read/write time, etc. On the other hand, computers currently available such as the VAX 8650 have several times the speed of the 11/780. For further discussion see Chapter 8.

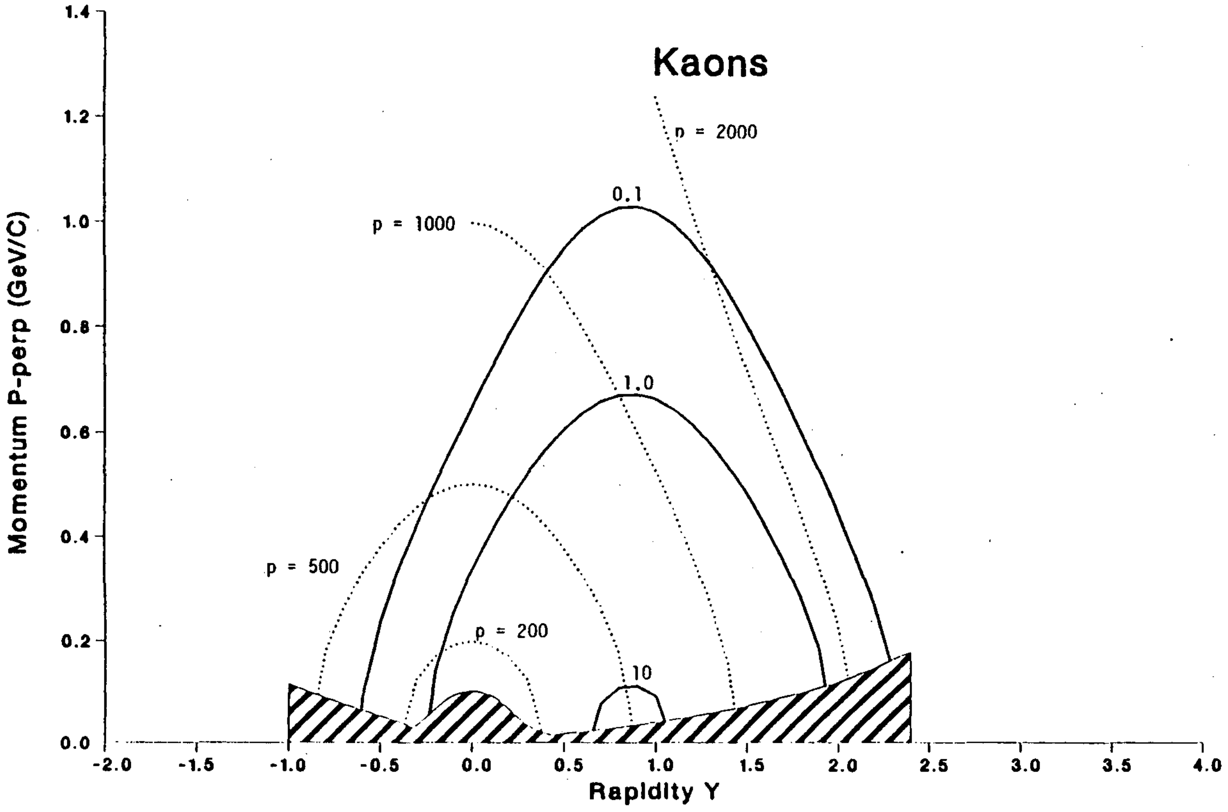

Fig. 1.6. A contour plot of the invariant cross section $E \; d\sigma/dp^3$ of participant kaons. The curves and axes have the same meaning and units as in Fig. 1.5.

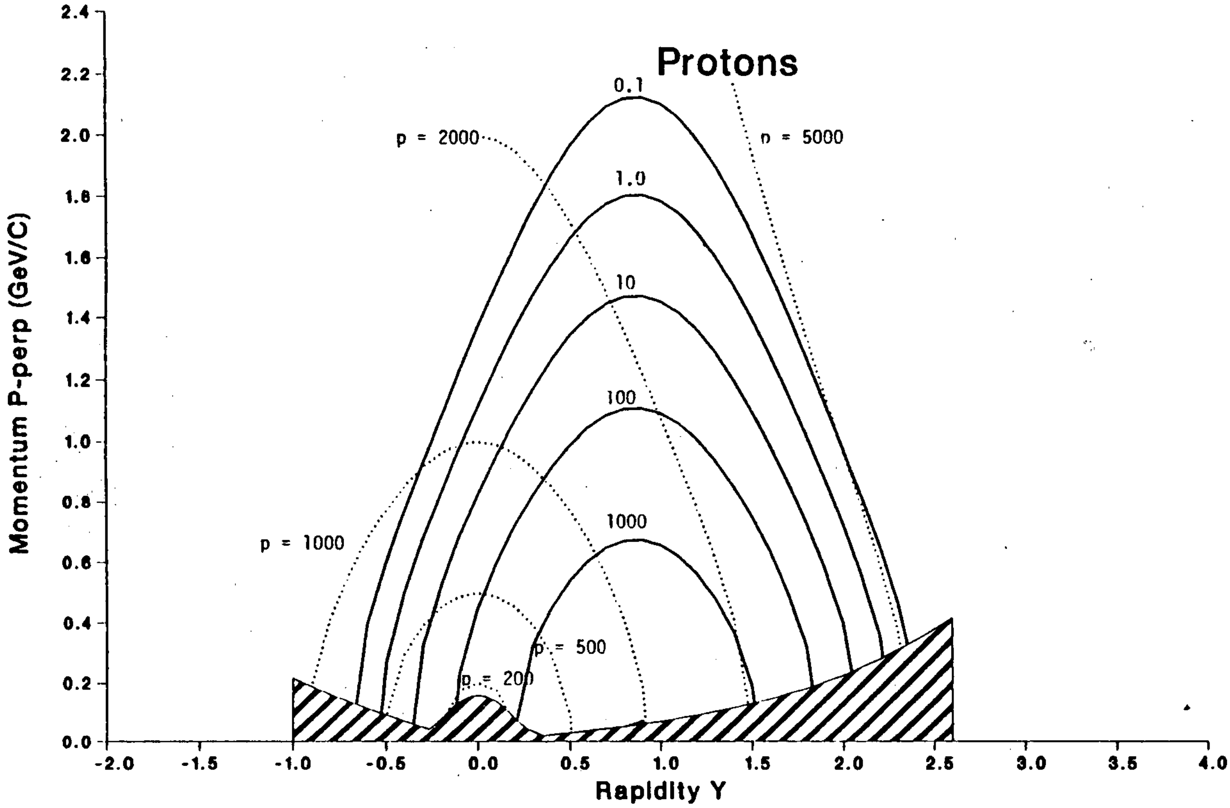

Fig. 1.7. A contour plot of the invariant cross section $E\ d\sigma/dp^3$ of participant protons. The curves and axes have the same meaning and units as in Fig. 1.5.

exceed by two to three orders of magnitude the entire output so far of the LBL Streamer Chamber Facility, which has produced many important results. Furthermore, the new detector will provide data on π^+, K^+ and the breakdown of heavy particles into p, d, t, ^{3}He, ^{4}He, all of which were not previously available. While the number of events analysed is comparable to, or greater than, that achieved by the Plastic Ball, the EOS TPC will provide much more information on each event, having wider dynamic range, much better two track resolution and particle identification capability, and the ability to measure the produced particles π^+ , π^- , K^+ and Λ^0.

The data output can be increased above those mentioned in Table 1.1, by the use of parallel processing techniques (which will be adopted), while the yield of a strange particles could be increased by an additional factor of up to 25 by the use of a strange particle trigger. Several options for such a trigger are under study.

Table 1.1

Data analyzed in 1 month CPU time at 0.2 seconds/track
(12,140,000 tracks)

Reaction	Events	π^+	π^-	K^+	Λ^0
Ar+KCl 1.8 GeV/A (Central)	2.9×10^5	1.4×10^6	1.7×10^6	1.1×10^4	1.1×10^4
Au+Au 1.0 GeV/A (Central)	6.6×10^4	8.0×10^5	1.6×10^6	2.6×10^3	2.6×10^3

1.5. Challenges

The EOS TPC will be one of the most ambitious detectors ever built for a nuclear physics experiment, comparable to the central detectors of the ALEPH and DELPHI experiments at LEP. Yet it seeks to measure events with ten times higher multiplicity of secondary particles and is in this respect more comparable to the detectors being discussed for the Superconducting Super Collider (SSC).

Apart from its complexity, the EOS TPC includes three aspects which have some degree of novelty, and which will require special attention in its design.

First, to achieve the essential multihit capability while limiting the number of electronic readout channels to the proposed 25,000, we have introduced a new type of endcap with varying pad sizes and wire spacings. This is discussed in Chapter 5.

Second, the range of dE/dx values encountered in the EOS TPC exceeds those of interest in most high energy physics detectors. This requires special front-end electronics, also discussed in Chapter 5.

Finally, the need for this detector with its enormous data output comes at a time when very rapid development of parallel processing techniques is taking place. This requires a radical approach to both data acquisition and analysis which must be designed from the beginning to make maximum use of the new computer technology.

All these efforts are justified by the potential knowledge to be gained by exploring the newly-opened field of study of the equation of state of nuclear matter. This equation determined, at the dawn of creation, our very existence; it determined the evolution of extraordinary astrophysical objects which are only now being discovered; and last but not least, it provides the most exhausting demands on our theoretical understanding of nuclear forces as being developed in modern relativistic theories.

Chapter 2

2. Scientific Objectives

2.1. Introduction

The past decade of experimental work at the Bevalac and associated theoretical studies have laid a broad foundation of knowledge concerning the overall properties of relativistic nucleus-nucleus collisions. The following fundamental observations have been made:

(a) It is possible, by several different methods, to make an experimental selection of events according to impact parameter.

(b) For an event with a given impact parameter, the nucleons observed in the final state can be classified as either spectators or participants.

(c) In central collisions between heavy nuclei, the participants are (on the average) brought to rest in their c.m. frame, i.e., the colliding nuclei stop in each other.

(d) Since stopping occurs, and the relative nucleon-nucleon velocity exceeds the sound velocity in nuclear matter, there must be a shock front in which the density increases: it has been estimated that densities as high as $4\rho_0$ may occur in this phase of the collision.

The existence of a high-density, though transient, phase of the collision opens up the possibility of studying the behavior of nuclear matter under extreme conditions previously inaccessible, and its equation of state. The equation of state is the relationship between density, temperature, and pressure for the material under study. It would ideally be desirable to identify some part of the nuclear interaction volume in a period of temporary equilibrium, and to measure its density, temperature, and pressure. In practice, all such information has to be inferred from measurements made in the final state, long after the interacting nuclei have disintegrated. Nevertheless, considerable progress has been made.

Calculations of the *density* show that it varies as a function of time and is not uniform throughout the nuclear volume. Though we have no direct control over the density, it can be influenced, by varying, for example, the beam energy or the sizes of the interacting nuclei.

The *pressure* (or more precisely the compressional energy) has been estimated from the observation that the yield of created pions, established in the high-density phase of the collision, is less than that expected if all the energy in the collision were available to produce pions. It has been suggested that the production of strange particles, such as $K^{\pm}$, may give additional information along these lines. A more direct, source of information on the pressure is the study of collective momentum flow effects which result from a pressure build-up at the interface between the colliding nuclei. Such measurements include the flow angle, and the average transverse momentum in the reaction plane, both measured as a function of impact parameters.

Temperatures have been obtained by fitting the final-state spectra of the participants with Boltzmann distributions. However, these have to be corrected for possible cooling during the expansion phase, and for collective expansion dynamics which is largely unknown. One way to avoid these difficulties, if the compressional energy is known, is to use overall energy conservation to determine the thermal energy and hence, indirectly, the temperature.

In addition to density, compressional energy, and temperature, other state variables can be related to physically measurable quantities. Of particular interest is the *entropy*, which can be measured by studying the ratios between yields of nucleons and complex fragments such as d, t, ^{3}He, and ^{4}He, which are determined by the density of nucleons in phase space. It has been found that the d/p ratio for individual collisions depends strongly on the impact parameter, being highest in the highest multiplicity events. By extrapolating the results, asymptotic entropy values have been extracted for comparison with theoretical predictions.

The above discussion shows that, even within a framework of thermodynamics, there is no unique way to approach an overall understanding of the reaction process and a qualitative explanation of the observations. If present lines of theoretical research continue to develop favorably, it may well be that the desired goal will be reached without any direct reference to state variables or to an equation of state. The nuclear forces used would have to be appropriate for the conditions prevalent in the collision: close contact between pairs of nucleons in an environment of locally high nuclear density. Success in explaining relativistic nucleus-nucleus collisions using these forces would lend confidence to predictions of the behavior of supernovae or of neutron stars, where comparable conditions prevail. An understanding of neutron stars involves, of course, additional ingredients resulting from the large size and long time scale of the system. Thus gravitational and weak forces must also be taken into account there. Assuming that the forces used are consistent with data on nucleon-nucleon interactions and nuclear structure, and have correct relativistic form, the end result of such a program would combine the most recent knowledge of medium-energy physics and heavy-ion physics with traditional nuclear structure physics into a globally satisfactory picture.

Obviously such a unifying program is not a short-term one. Only the beginning steps have been taken, both in experimental and theoretical studies. Nevertheless, the stage has been set for major progress. The EOS TPC will permit the measurement of a new wide range of high precision data. By the time it is ready, new theoretical approaches, stimulated by the already existing results, will be available to be confronted by new measurements. To illustrate the potential for such confrontations, we choose a recent calculation [Ai 86] which is specially valuable for our present purpose since it has been used to make predictions for five different variables which can be measured simultaneously with the detector we are proposing. Figure 2.1 shows predictions for the density reached in La + La collisions at 800 MeV/A, and for an impact parameter of $b = 2$ fm. In this calculation, a "quantum molecular dynamics" approach is used, which combines the advantages of the classical molecular dynamics approach, i.e., the N-

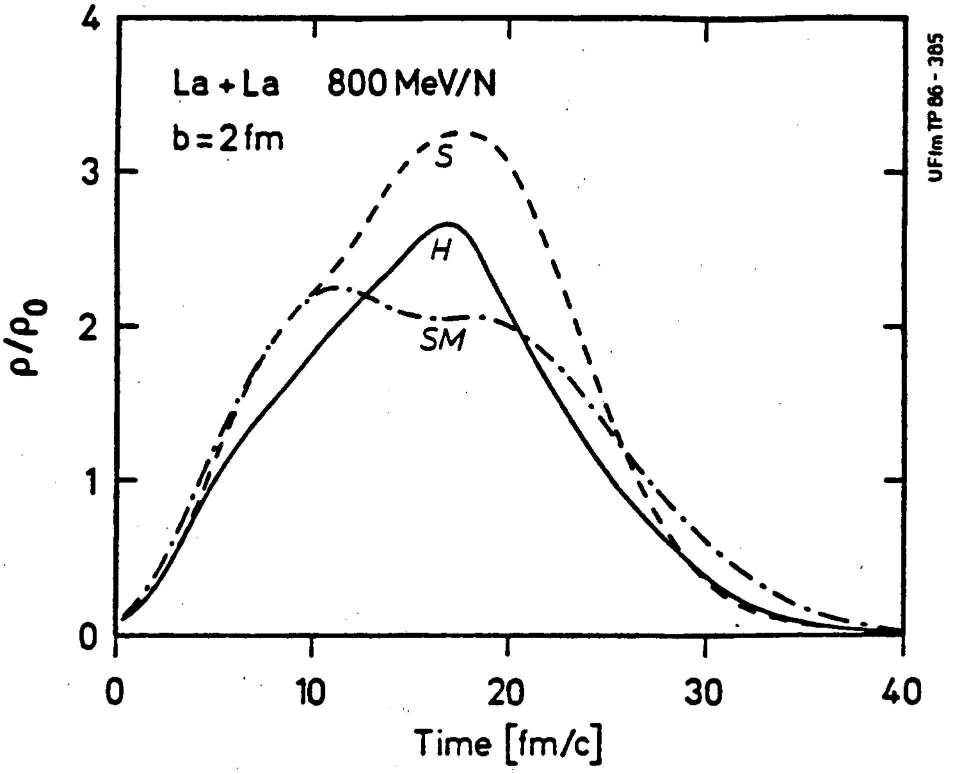

Fig. 2.1. Theoretical predictions [Ai 86] of the density reached in La+La collisions at 0.8 GeV/A and b = 2 fm is shown as a function of time, using the S, SM, and H interactions. The interactions are discussed in the text.

body correlations and an equation of state, with the important quantum features of the Vlasov-Uehling-Uhlenbeck approach, namely, the Pauli principle, stochastic scattering, and particle production. The long-range Coulomb and Yukawa forces as well as the momentum dependence of the nucleon-nucleon interactions are taken into account.

Three different interaction potentials are used to predict observables. In each case the equation of state of nuclear matter is also calculated from the potential. The potentials are designated *S* (for a soft local potential), *H* (for a hard local potential) and *SM* (for a soft, but momentum-dependent, potential). The *S* potential leads to a soft equation of state, while the *H* and *SM* potentials both lead to about the same stiff equation of state. The soft equation of state, as expected, allows greater densities to be reached in the collision than for the hard equation of state. Comparison of both predictions with that for the *SM* interaction shows that the momentum dependence of the interaction is an important aspect of the equation of state in determining the central density.

Figure 2.2 shows predictions of kaon, pion, and deuteron production, using the three interactions. The points shown in the figure are the theoretical calculations, with their numerical uncertainties: no comparison is made with data. Pion production is relatively insensitive to the equation of state: it is mainly the high precision obtainable in the measurement of negative pion multiplicities that has focused attention on this observable. Once again the momentum dependence of the interaction has an effect comparable to the difference between the equations of state. This effect is interpreted by the authors as reflecting a reduced

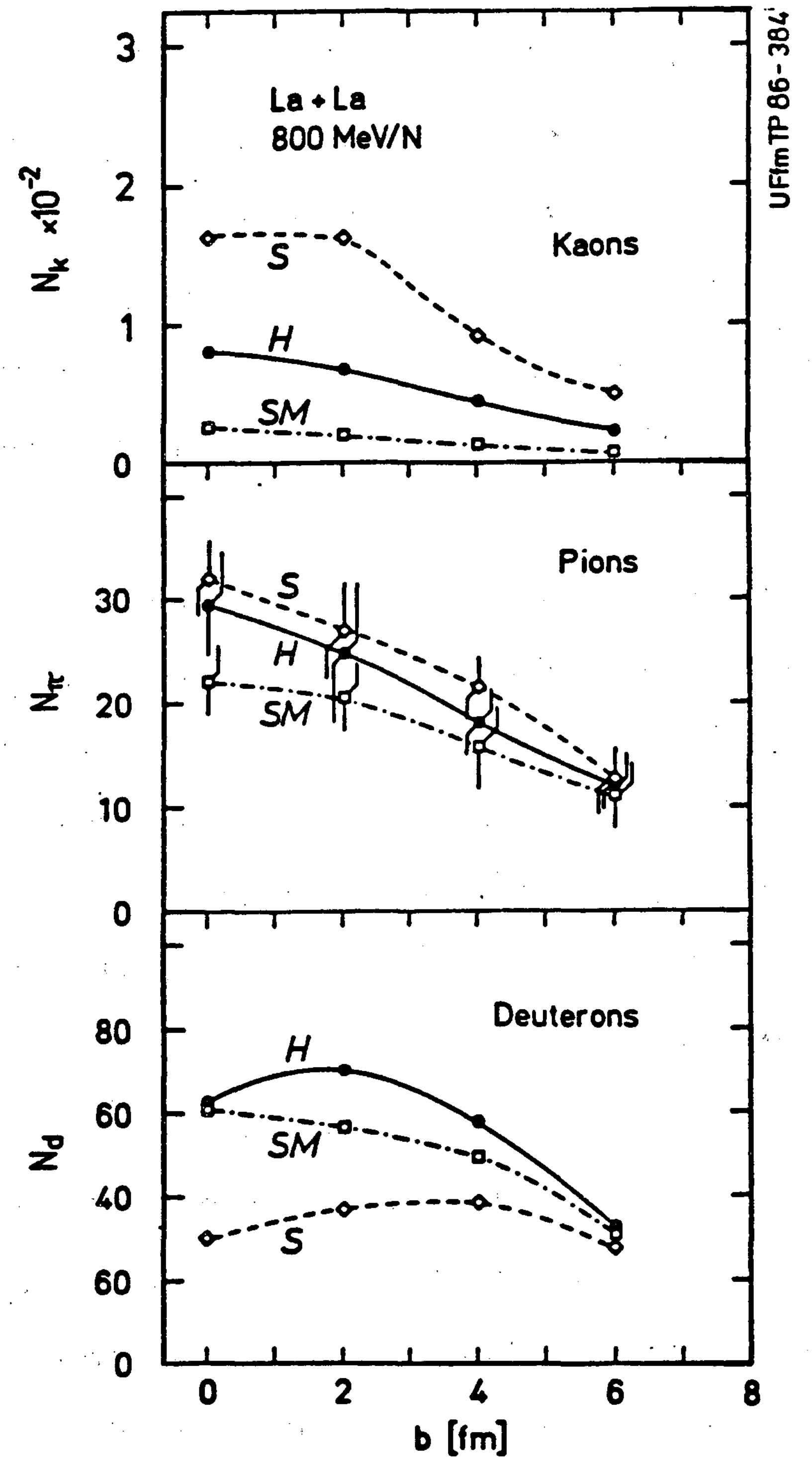

Fig. 2.2. The impact parameter dependence of the kaon, pion, and deuteron yield for La+La collisions at 0.8 GeV/A [Ai 86].

number of nucleon-nucleon collisions during the interaction when the momentum dependence is introduced. Kaon production, for which no data exist at this energy, shows a large sensitivity to the equation of state, but once again the momentum dependence is still more important. The authors attribute the effect in this situation to large off-shell effects in the kaon production amplitude. The simultaneous measurement of kaon, pion, and deuteron production offers an opportunity to separate the effects, provided data at the few per cent level of accuracy can be obtained.

Figure 2.3 shows predictions for average transverse momentum and flow angles. It shows in an interesting way that these two types of analysis are complementary. Transverse momentum is a useful variable at finite impact parameters, but in the limit $b \rightarrow 0$ it does not indicate whether the La + La system in a head-on collision tends to be oblate or prolate. The flow angle and the ratios of the semi-axes of the momentum ellipsoid in a complete sphericity analysis might answer this interesting question.

These predictions have been used here primarily for illustrative purposes. Undoubtedly improvements will be made in calculational techniques and in the interactions used. The calculations shown indicate substantial progress towards consistency of treatment away from an artificial emphasis on specific features (such as the hardness or softness of the equation of state) at the expense of others (such as the momentum dependence, or otherwise, of the interaction). The more important conclusion is that experimental data, if available, could help clarify these effects and focus attention on the most important aspects. Because of the

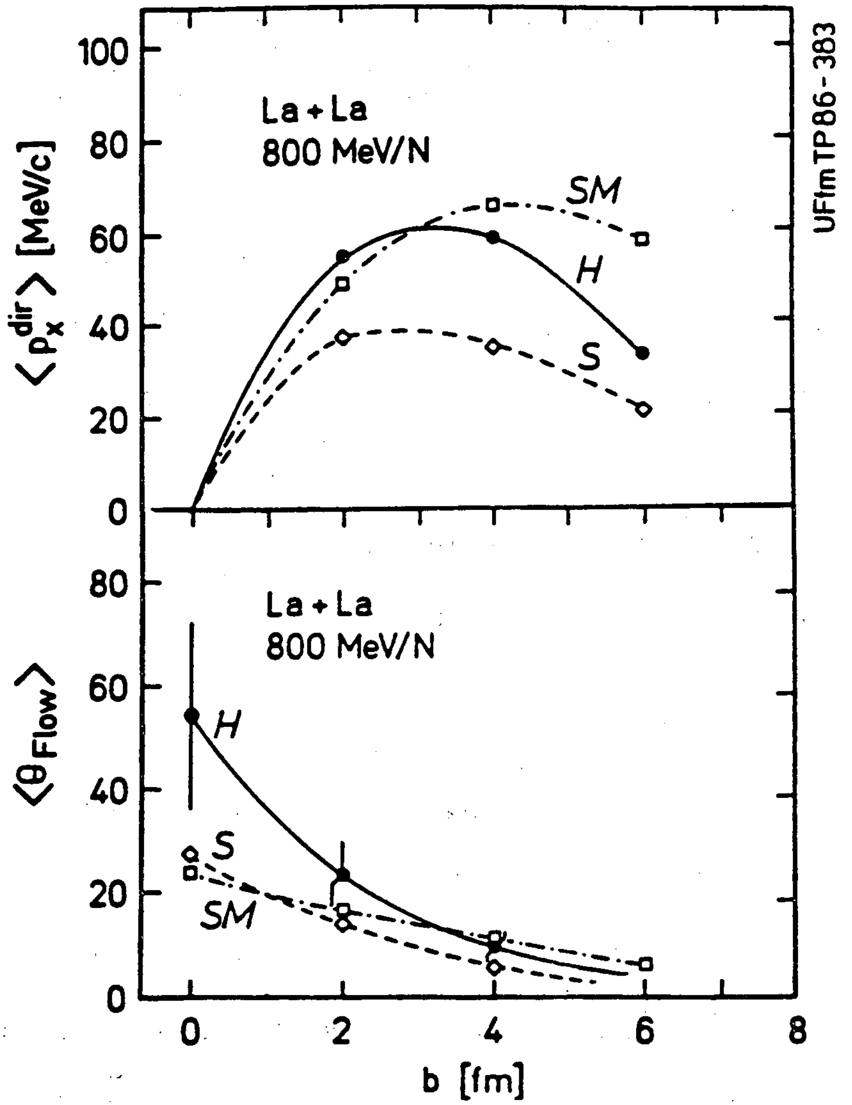

Fig. 2.3. The average transverse momentum and flow angle are plotted against the impact parameter for La+La collisions at 0.8 GeV/A [Ai 86].

difficulty of comparing data from different experiments (uncertainties of ±20% are common, even within sets of data by the same group) it is specially important to obtain data with a common normalization from a single experiment. This is achieved by means of a 4π detector, with nearly complete solid angle coverage, and with large and uniform momentum acceptance for a wide range of different types of particle. The EOS TPC will achieve this goal in the mid-rapidity, fireball, regime.

In the remaining sections of this Chapter we address some specific points of current interest in the study of pions, strange particles, and light nuclear fragments. One expects that the relative significance of these questions will change during the period while the detector is being built, and that new questions will arise. The comprehensive nature of the measurements planned ensures that such changes of emphasis can be accommodated.

2.2. Pion Production

Copious pion production is characteristic of nucleus-nucleus collisions at the Bevalac, reflecting the relativistic nature of the nucleon-nucleon interaction at these energies. The results are usually interpreted in the framework of the isobar model, in which the process that creates or removes pion-like degrees of freedom is $NN \leftrightarrows N\Delta$, while the process $\Delta \leftrightarrows N\pi$ produces or absorbs real pions while leaving unchanged the total pion-like abundancy.

The most relevant data on pion production have been measured using the Streamer Chamber, where π^- can readily be identified as the only particle with negative charge produced in substantial quantities. There it was found that the multiplicity of π^- per event is proportional to the number of participant nucleons in the event, over a wide range of circumstances. In particular, for head-on collisions of equal mass nuclei, where all the nucleons participate, the π^- multiplicity is found to be proportional to A for nuclei up to ^{139}La, beyond which there are no pion measurements at all. If we extrapolate existing π^- results to Au + Au and extract the $\pi^- : \pi^0 : \pi^+$ yield ratios from the isobar model we expect the multiplicities in central collisions at 1 GeV/A to be $24\ \pi^- : 17\ \pi^0 : 12\ \pi^+$. The EOS TPC would permit *simultaneous* measurements of the π^- and π^+ yields in individual collisions, providing opportunities for accurate new tests of the reaction mechanism.

Pion energy spectra in central collisions of light nuclei are consistent with cascade calculations and the attainment of thermal equilibrium between nucleons and Δ-resonances. The spectra measured for La + La show a marked deviation from cascade and thermal model predictions, which is not yet understood. It would be very helpful to obtain systematic measurements of both π^+ and π^- for nuclei over the full mass range, especially in conjunction with simultaneous measurements of collective flow. Such correlated measurements are important since pion intensity interferometry measurements (see below) have indicated that "shadowing" of pion production by the bulk matter surrounding the interaction zone has an important effect on the shape and size of the effective source. While an understanding of the pion spectra in the final state is not expected to have a direct impact on equation-of-state studies, it would be an important step forward which could help clarify uncertainties concerning questions of pion absorption, charge exchange, and re-emission.

Given a detector sensitive to π^+ and π^- with a large dynamic range and with the capability to accept a high data rate, collisions between heavy nuclei provide interesting possibilities for application of the pion intensity interferometric technique [Za 84], [Gy 79]. The high multiplicities yield many correlated pairs; three-or-more-pion correlations can be studied, which is useful because three-pion correlations give independent evidence on the coherence or non-coherence observed in two-pion correlations; simultaneous study of other event characteristics such as flow, or multiplicities of various particles, would enhance the information obtained. It has already been demonstrated that 2π correlations provide a powerful tool to study the evolution in space and time of the collision process, but it has not yet been used to study events already selected by impact parameter, multiplicity, flow, temperature, etc.

2.3. Strange Particle Production

In nucleus-nucleus collisions at the Bevalac strange particles are assumed to be produced in associated pairs of opposite strangeness, as in the reaction $NN \rightarrow N\ \Lambda^0\ K^+$. No experiment has so far had the capability to measure both partners in the pair. Extensive K^+ inclusive studies have been carried out with light projectiles, Λ^0 production has been studied in central Ar + KCl collisions at the Streamer Chamber, and some limited K^- studies have been carried out in a beam-line spectrometer at zero degrees.

The cross sections for production of strange particles and for their subsequent interactions in the nucleus are much smaller than the corresponding cross sections for pions. The probability for strangeness production in a central collision is a few per cent, while the probability for two strangeness-producing interactions in a central collision is of the order of one part in one thousand. No events of the latter kind have so far been observed. A consequence of this low production probability is that a strange particle, once created, has a low probability of losing its strangeness (unless by chance it should re-encounter the partner with which it was created after some scattering within the nucleus). However, strange particles escape rather easily from the nucleus, and are not expected to reach equilibrium concentrations inside the nucleus during the short duration of the overall collision. Thus the number of strange particles measured in the final state must reflect closely the number initially produced. This is in marked contrast to the corresponding situation for pions, where more complex theoretical analysis is required to relate the final state to the more interesting hot high-density phase of the reaction.

As a result of these considerations, the study of strange particle production offers a probe of the early stage of the collision with some of the advantages of lepton or dilepton production, but with a much larger yield. The reason why K^+ and Λ^0 have not, in contrast with π^-, been used significantly to study the equation of state is that the primary nucleon-nucleon production rates are not at all well known, with uncertainties of the order of ± 50%. Thus a systematic study requires also measurement of these rates. The EOS TPC is well suited to carry out such measurements, which have not been practical in the streamer chamber, where more than 10^6 events would have had to be measured to obtain an adequate sample of Λ^0. In addition, the EOS TPC will allow measurement of both the Λ^0 and K^+ in an event, and the observation of rarer events with more than one pair produced. In all cases, the remainder of the event topology would also be determined.

Inclusive K^+ production has been studied only for light nuclear projectiles, sufficiently to determine that the total yield is approximately that predicted by a cascade calculation. According to this calculation, the kaons are produced in the early stages of the collision by associated $K^+ \Lambda^0$ (or Σ^0) production. This is consistent with the observation that K^+ and Λ^0 temperatures are somewhat higher than those of nucleons. Unfortunately, when one considers the details of the production, especially energy spectra, the success of the theory is less satisfactory. The open questions would be simplified if K^+ production could be studied for impact-parameter-selected events, if other quantities such as pion multiplicity were simultaneously obtained.

In estimating yields of strange particles for collisions between heavy nuclei, one has to extrapolate from inclusive K^+ measurements with projectiles up to ^{20}Ne at 2.1 GeV/A and from Λ^0 production in central ^{40}Ar + KCl collisions at 1.8 GeV/A, using the observation that the total yield is proportional to $A_p A_t$. This could produce a yield increased by a factor of 30 for symmetric collisions of heavy nuclei, i.e., about one K^+ per central collision. However, the available beam energy is substantially reduced for heavy nuclei, leading to a reduction by a factor of 10–30 depending on details of the theory. Thus a reasonable planning estimate is that the yield of K^+ and Λ^0 for Au + Au at 1 GeV/A will be about the same as in Ar + KCl at 1.8 GeV/A, i.e., about 0.04 per central event. With such a yield, a 4π electronic detector will gather enough statistics for energy spectra to be measured as a function of angle in central collisions and for correlations to be carried out with other event characteristics.

For each K^+ there should be a Λ^0, except in the relatively rare case of K^+K^- pair production, which is suppressed energetically. It would be interesting to obtain Λ^0 energy spectra and angular distributions subject to the same conditions as the K^+ measurements. For Λ^0 an additional quantity is simply measurable, the polarization. The $\Lambda^0 \rightarrow p\ \pi^-$ decay is self analyzing, and the angular distribution of the decay protons in the Λ^0 rest frame, relative to the normal to the Λ^0 production plane, is

$$dn/d\Omega = (1 - 0.642P\ \cos\theta)/4\pi$$

where P is the polarization of the Λ^0. In nucleon-nucleon collisions, the Λ^0 polarization is found to be proportional to the transverse Λ^0 momentum. In streamer chamber experiments at the Bevalac and at the Synchrophasotron, Λ^0 polarization has been measured for small samples. Within the limited statistics the results are consistent either with zero or with the same transverse momentum dependence as in nucleon-nucleon collisions. Measurements with good statistics would add Λ^0 polarization as a test of the reaction mechanism.

No systematic study of K^- production has so far been carried out. Comparison of K^- and K^+ production would be useful in connection with deciding the influence of finite mean free path effects. Present knowledge concerning K^- production is based on measurements at zero degrees only, where it is found that the yield is roughly 1/20 that of K^+ and that the c.m. energy spectrum falls off much more rapidly than that for K^+. These observations are consistent with a tertiary production mechanism in which, for example, the reaction $\pi\,\Lambda^0 \rightarrow K^-N$ occurs. Because of the low yield and the necessity for superlative K/π discrimination K^- studies will continue to demand specialized detectors. Nevertheless it may be possible, using the EOS TPC, to obtain useful information on the total multiplicity. It would be especially valuable to examine events in which a K^+ is produced, to see what fraction includes a Λ^0 and what fraction includes a K^-. It is difficult to see how such information could be acquired in any other way.

2.4. Light Charged Participants ($p, d, t, {}^3$He, ^{4}He)

The bulk of the outgoing particles (with the exception of neutrons) fall in this category, and they carry the most basic information about the collision. Studies of flow and transverse momentum distributions have begun. It will be important to develop the capability to obtain high-precision data: not only data with good statistics but data that are relatively free from major efficiency corrections and which cover the full dynamic range with good particle identification.

Extensive studies have demonstrated the existence of collective flow for collisions with non-zero impact parameter. Here the outgoing momentum is concentrated along some angle which is greater than zero and increases with increasing multiplicity (decreasing impact parameter). At impact parameter $b = 0$ it has been suggested that the momentum ellipsoid should become oblate, but the best evidence so far is consistent with a spherical shape. Since the flow angle for non-zero impact parameters is a manifestation of the pressure build-up at the interface between the colliding nuclei, one may ask: where is the final-state flow for *central* collisions? Evidence from pion production suggests that about 30% of the energy in central collisions is tied up in compression at the moment of maximum density. It is possible that this compressional energy is converted into thermal motion as the nuclear system expands. On the other hand, if the expansion is isentropic, it may be manifested as radial flow. This idea was originated by Siemens and Rasmussen, who christened the radial flow as a "blast wave" [Si 79].

The resolution of this question is crucial to an understanding of relativistic nucleus-nucleus collisions. If there is an appreciable amount of radial flow, the spectra of final state particles will not reflect the temperature of the system, but some combination of thermal and collective flow motion. Over most of the dynamic range such a combination yields a Boltzmann-like distribution, but with an incorrect temperature. In order to resolve this issue, it will be necessary to obtain precision data on the energy spectra of outgoing particles in impact-parameter selected data. Slight deviations from a thermal spectrum should be seen at very low particle velocities, where the collective motion is most important: particles should be boosted to slightly higher velocities than expected on the basis of the true temperature. At very high velocities the collective motion should become negligible and the slope of the spectrum should yield the true temperature. In between, the combination of thermal and collective motion would yield an effective temperature which is greater than the true temperature.

A fundamental question concerning relativistic nucleus-nucleus collisions is that of how much entropy is generated. In the extreme, a large generation of entropy could indicate a phase change. The basic key to entropy measurement lies in the observation that the density of particles in phase space determines the ratio of deuterons to protons in the system. Theoretical development of this idea continues. While contact with experiment has not been consistent either in its method or its results, the experimental needs have become clear. It is necessary to make complete measurements of the energies and angles of all produced p , d , t , ^{3}He, ^{4}He over as wide a dynamic range as possible, as a function of total multiplicity. A good determination of entropy would be a useful third measure of the nuclear matter equation of state (in addition to particle production and flow).

Apart from the possibility of studying flow and entropy, the data on light charged participants will (if accurate enough) permit many useful tests to be made. As an example, it was suggested in Section 2.2 that negative pion production in heavy nuclear collisions may exceed positive pion production by a factor of two. This ratio originated from the isospin of the colliding nuclei. It would be of great interest to study the equation of state as a function of isospin since all the astrophysical objects tend to be neutron-rich. The preferential emission of π^- will have a tendency to restore the isospin towards zero. This tendency would be reduced by pion charge-exchange effects. The careful comparison of ^{3}H~~e~~ and ^{3}He yields in the final state would provide complementary information on the final isospin content of the system.

Finally, it should be remarked that with expanded detector capabilities, and especially with heavy projectiles and target, more variables become measurable and statistically significant within individual events. Tests of new ideas become possible. As an attractive example, consider the possibility that there is a class of central collisions in which something like a pion condensate occurs. This would result in low temperatures, low entropy, perhaps in low multiplicities and perhaps with special effects to be seen in the pions. This would almost certainly have escaped attention with the detectors available to date. It is worth remembering that in collisions between very heavy nuclei the number of particles of each type is very large and significant variations from the norm should be easy to recognize, if the dynamic range of the detector and its efficiency and solid angle are complete enough. For example, in a Au+Au event it should be possible to determine the temperature to an accuracy of 10% by measuring the protons. With 24 π^- and 12 π^+, pion variables of useful statistical accuracy will be available in each event.

Chapter 3

3. Event Characteristics

3.1. Reaction Models

In order to set the design parameters of the detector and to test its adequacy, it was desired to input as much information as is already available about heavy ion reactions in the Bevalac energy range. Since this is fragmentary, reaction models were used to extrapolate the data into unknown regions. Since the emphasis of the research is to study the fireball, the models used were those which can be adjusted to match the properties of particles emitted in the participant regime, from central collisions. Three programs have been used extensively: a) the fireball code, Therm2; b) the Fai-Randrup code; and c) the detector simulation code, GEANT3.

The Therm2 program assumes that the yield of a given particle in a central collision is the product of three factors: The cross section σ for the central collision, the multiplicity M of particles of that type emitted in a central collision, and a momentum distribution $f(p)$ which is isotropic in the c.m. system and determined by a temperature T.

For a particle of mass m and temperature T, the momentum distribution in the c.m. system is given by [Ha 71]:

$$f(p)dp = \frac{p^2 dp}{exp(\sqrt{p^2+m^2}/T) - b}$$

where b =1, 0, or −1, according to whether the particle is a boson, classical particle, or fermion.

For each event, the number of particles of mass m appearing in $dpd\Omega$ in the c.m. system is then given by:

$$dn = \frac{Mf(p)dp}{\int f(p)dp} \cdot \frac{d\Omega}{4\pi}$$

where M is the multiplicity of particle m in the breakup of the fireball. The cross section for production of particles of mass m in $dpd\Omega$ for central collisions is given by $d\sigma = \sigma dn$, where σ is the central collision cross section.

The simulation of events using Therm2 has the advantages that yields and "temperatures" of different particles can be varied independently to match experimental data, and that individual particles can be calculated without calculating entire events. The latter is important for rare particles such as K^+ or Λ^0. The program does not, on the other hand, allow for two-particle correlations or for long-range correlations such as flow, which would increase the particle density in localized regions of phase space.

The Fai-Randrup program [Fa 83] was designed to provide a reference model that invokes as few assumptions as possible about the specific dynamics of the collision process, to serve as a standard against which more sophisticated theoretical calculations could be judged, to serve as a background for recognizing peculiar structures in experimental data, and to help in assessing the acceptance of particular detection systems. In it, three particle sources are used: two spectator sources and one participant source. Each source is characterized by its number of nucleons, charge, and total four momentum. If a source has excitation energy sufficient for complete disassembly into free nucleons, it is said to be above the disassembly threshold. It is then assumed to explode quickly into a number of pions, nucleons, and composite nuclei that are generally excited and particle unstable. If a source is below the disassembly threshold it is assumed to de-excite by sequential light particle evaporation, and the same is assumed for the particle unstable explosion products.

The program includes a number of parameters that can be matched to experimental data, and flow effects can be introduced. We have used it for Au + Au collisions at 1 GeV/A, with input parameters provided by the Plastic Ball group, based on their global measurements. We have found it useful for estimating yields of heavy fragments. However, it greatly overestimated the temperatures of the pion spectra.

The response of the detector was simulated using the CERN program GEANT3, which was written by R. Brun, F. Bruyant, A.C. McPherson, and P. Zanarini for the purpose of modelling high energy physics experiments [Br 85]. GEANT3 incorporates standard packages for handling experimental geometry, particle tracking, decay processes, secondary interactions, and graphics. Several examples of its use are shown in Chapter 4.

3.2. Multiplicities

Table 3.1 shows the test events which we have used to evaluate the capabilities of the detector. We chose two reactions: Ar+KCl at 1.8 GeV/A and Au+Au at 1.0 GeV/A, each at the highest energy of the Bevalac for that projectile. The former is well documented for π^-, K^+ and Λ^0 production [Sa 80], [Ha 81] and suitable to test the particle identification capabilities of the detector. The latter provides a severe test of the detector's capabilities for handling high multiplicity events.

Table 3.1

Multiplicities and temperatures for central collisions.

	Ar+KCl 1.8 GeV/A	Au+Au 1.0 GeV/A
n_{ch}	46	199
p, d, t	20, 10, 2	97, 49, 10
^{3}He, ^{4}He	2, 1	5, 2
n	21	145
π^+, π^o, π^-	5, 5, 6	12, 17, 24
K^+, Λ^o	0.04, 0.04	0.04, 0.04
$T_p=T_K=T_\Lambda$ (MeV)	118	90
T_π (MeV)	69	50

In estimating the numbers given in Table 3.1 we assumed completely central collisions, i.e., all the incoming nucleons participate in the collision and appear in the outgoing fireball spectra. The yields of p, d, t were assumed to be in the ratio 1.0 : 0.5 : 0.1 which is roughly consistent with several observations in the neighborhood of 0.8 GeV/A [Na 81a, GS 86, Do 85]. The yield of π^- was taken from from experimental data on Ar+KCl and La+La [Ha 85] [Ha 86], extrapolated to other charges according to the ratio $\pi^+:\pi^o:\pi^- = 5Z^2+NZ : N^2+Z^2 +4NZ : 5N^2+NZ$ [St 86], and extrapolated to Au+Au by assuming that the total number of pions produced in central collisions is proportional to A [Ha 86]. The yield of K^+, and Λ^0 was taken from measurements of Λ^0 in central Ar+KCl collisions at 1.8 GeV/A [Ha 81], and the yield for Au+Au at 1.0 GeV/A was set equal to it using arguments set forth in Chapter 2. The yields of ^{3}He are based on very limited experimental data and have been adjusted to balance charge in the reaction. The yields of neutrons are obtained by balancing mass, and the total number of charged particles, n_{ch}, is obtained by adding the appropriate values in the table. The temperatures T_p and T_π for Ar+KCl were obtained from [Br 84]. T_Λ was set equal to T_K [GS 86, Schn 82] and both were set equal to T_p for simplicity, even though the observations suggest that they are about 10 MeV higher than T_p. The temperatures for Au+Au were based on a variety of data on the energy dependence of temperatures, assumed to be independent of A.

The data in Table 3.1 should not be misinterpreted as a compilation of experimental data suitable for theoretical interpretation. Most of the figures are obtained by very indirect means. Among the charged particle data, the yields of complex particles at 1.8 GeV/A are probably overestimated. This does not affect the usefulness of the results for our present purpose since the total yield of singly charged particles is almost fixed as a result of charge conservation and the reliable pion yields. The yield of π^+ for Au+Au is completely unknown

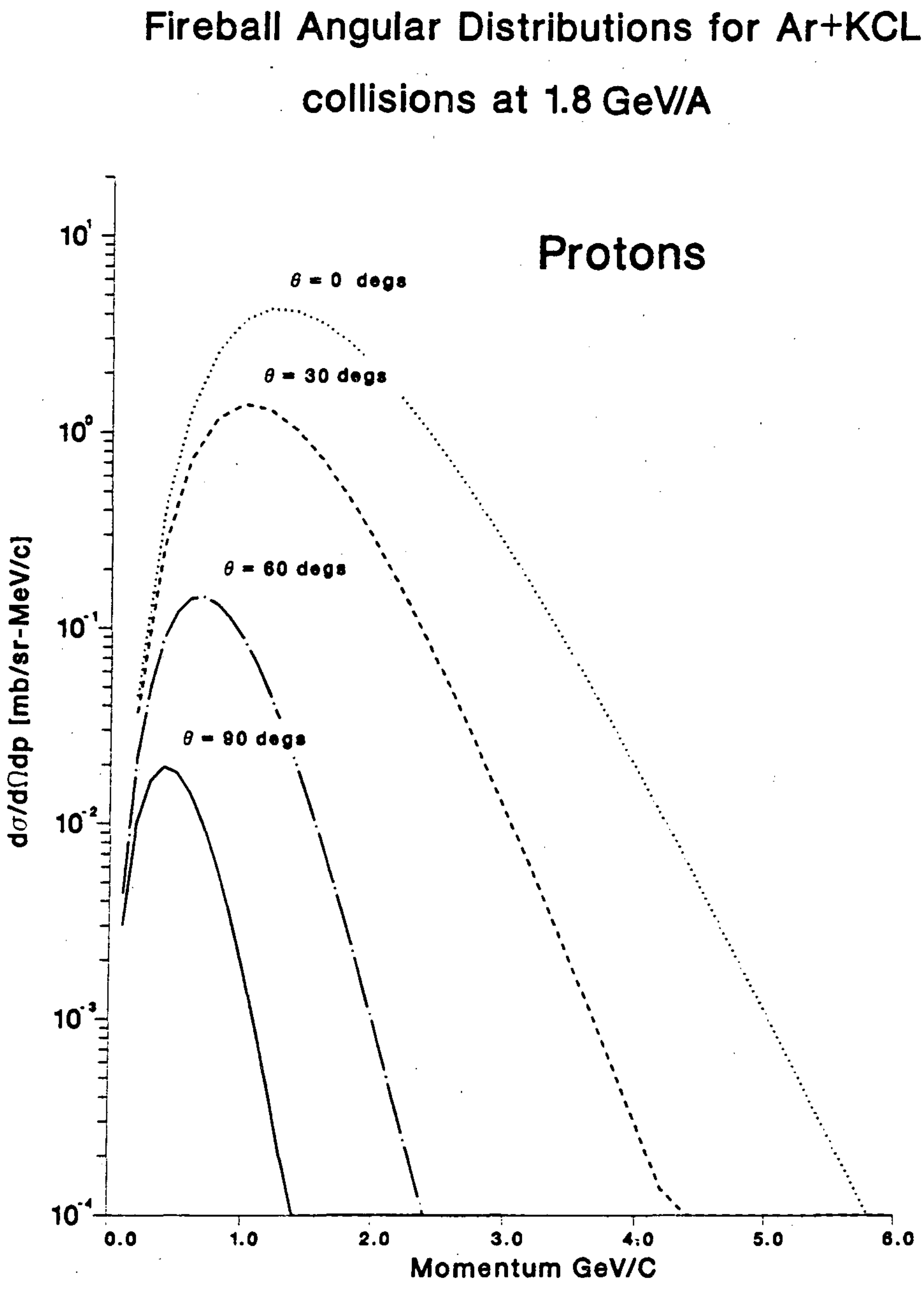

Fig. 3.1(a). Differential cross section versus participant proton momentum for central Ar+KCl collisions at 1.8 GeV/A, calculated with the program Therm2. A central collision cross section of 180 mb was assumed.

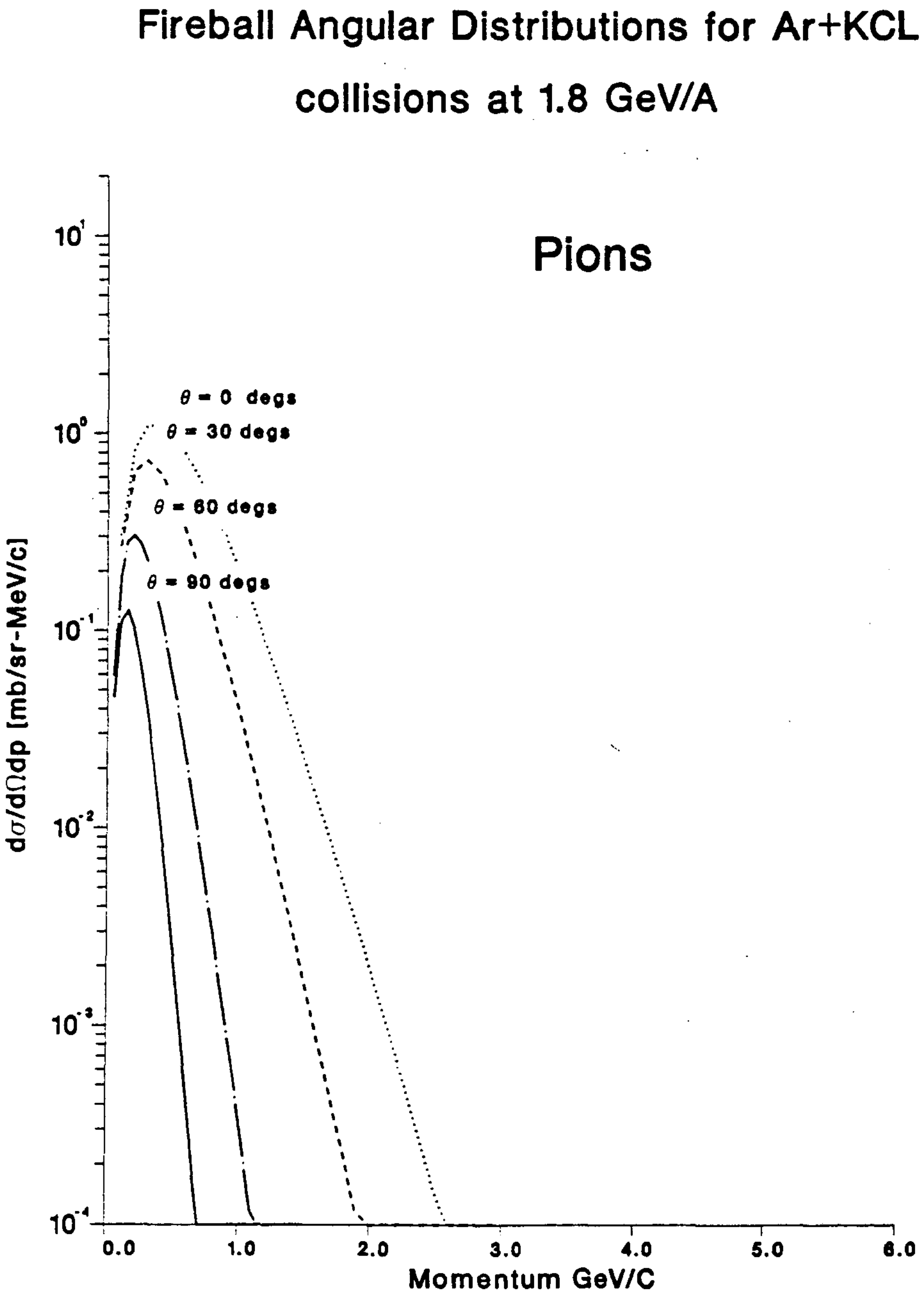

Fig. 3.1(b). Differential cross section versus participant pion momentum for central Ar+KCl collisions at 1.8 GeV/A, calculated with the program Therm2. A central collision cross section of 180 mb was assumed.

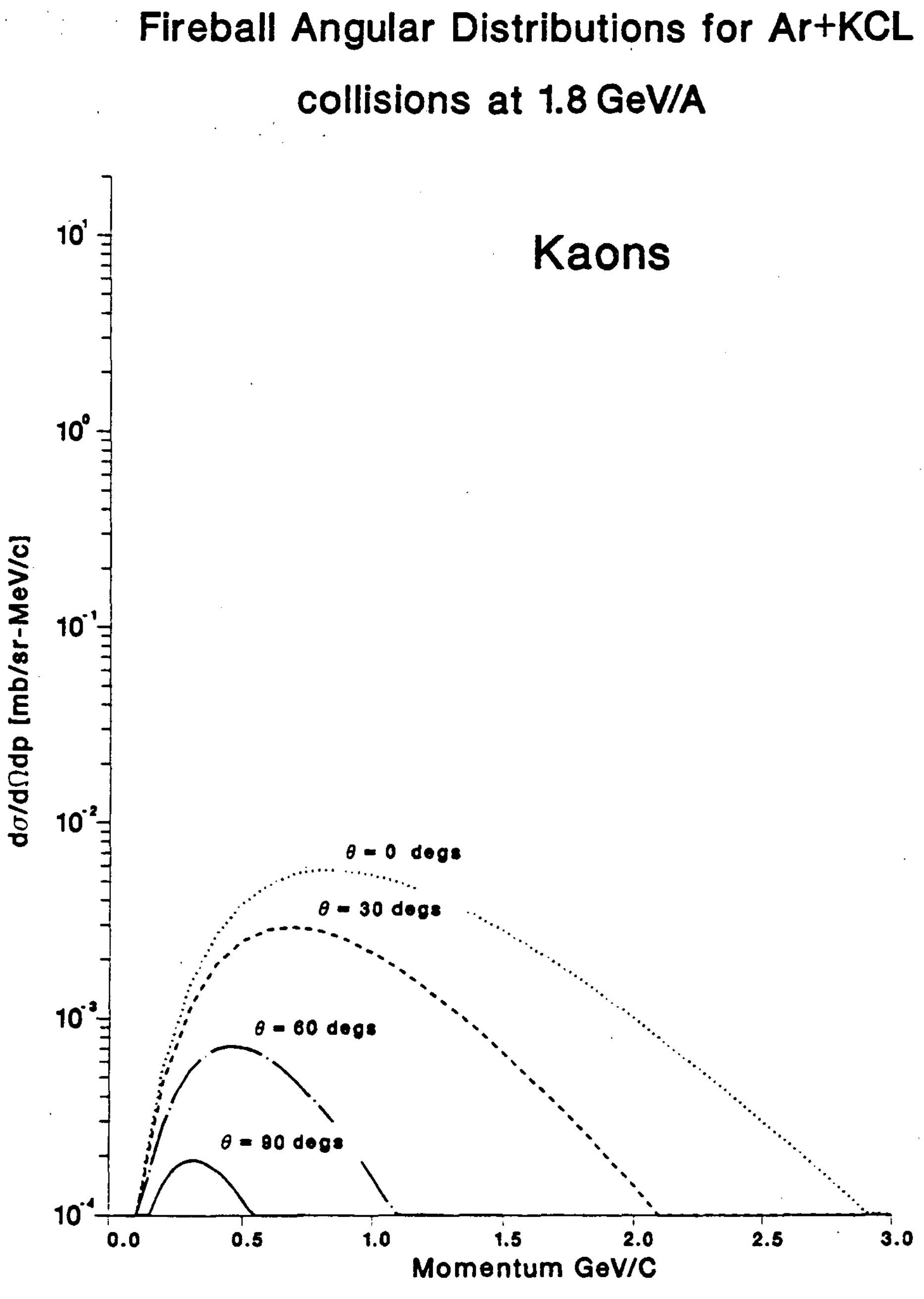

Fig. 3.1(c). Differential cross section versus participant kaon momentum for central Ar+KCl collisions at 1.8 GeV/A, calculated with the program Therm2. A central collision cross section of 180 mb was assumed.

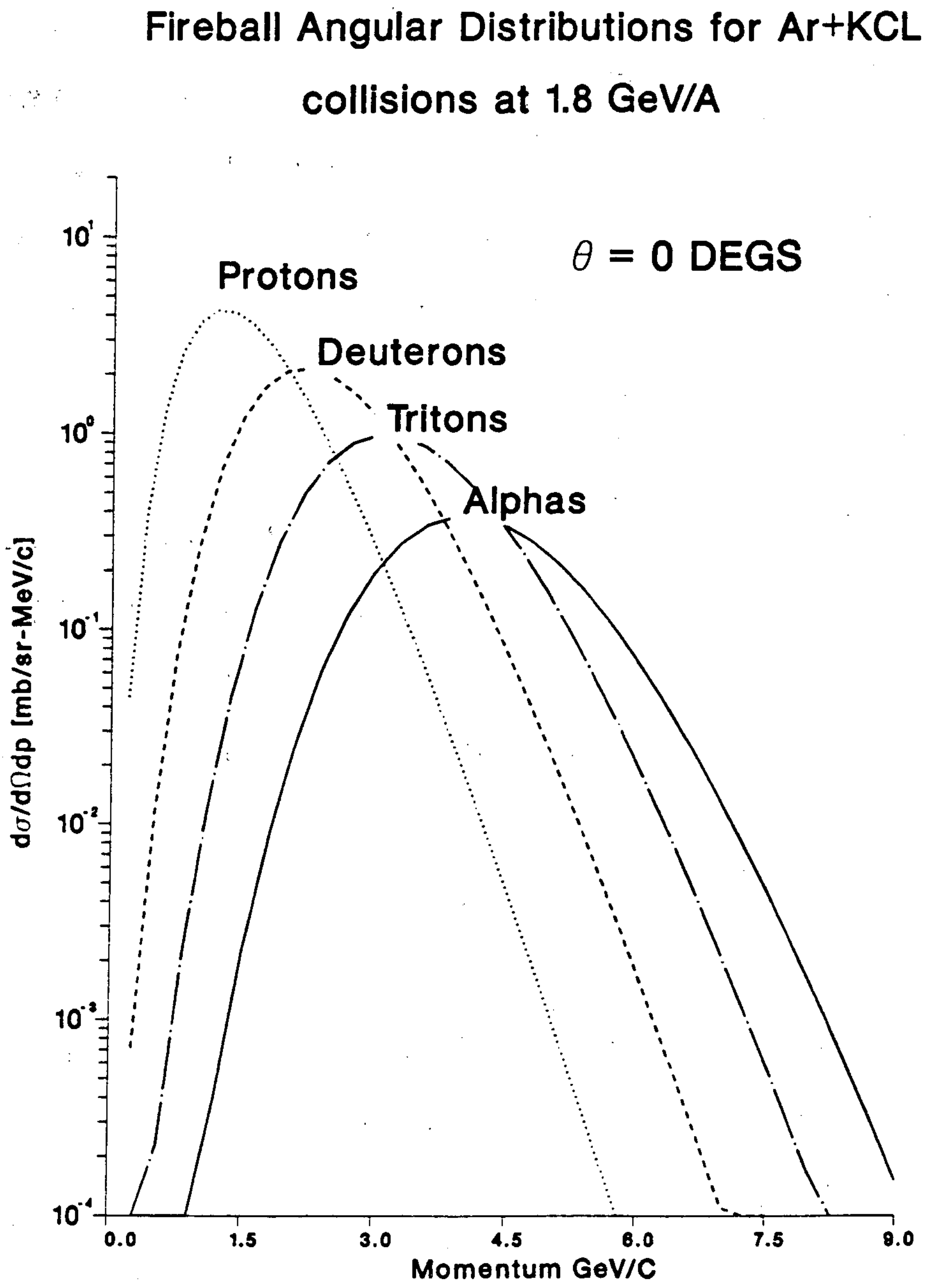

Fig. 3.1(d). Differential cross sections at $\theta = 0^o$ versus participant momentum for central Ar+KCl collisions at 1.8 GeV/A, calculated with the program Therm2. A central collision cross section of 180 mb was assumed.

experimentally. Perhaps the most serious deficiency in the model is the assumption that the pion spectra can be characterized by a single temperature. Evidence on Ar+KCl at 1.8 GeV/A suggests a 5% component at a temperature comparable to that of the protons [Br 84]. Recent evidence on La+La shows a similar tendency [GS 86]. This could make the detection of kaons more difficult by increasing the number of pions at the same momenta.

3.3. Spectra

Figure 3.1(a)-(d) show spectra generated by Therm2 for central Ar+KCl collisions at 1.8 GeV/A assuming a collision cross section of 180 mb. The lowest level plotted is the lowest cross section we consider feasible to measure in an extended period of data analysis. Figure 3.2(a)-(d) show similar results for central Au+Au collisions at 1.0 GeV/A. It is clear that in either reaction we will be able to obtain an excellent overall picture of fireball protons, kaons, and pions, subject to adequate particle identification.

An alternative presentation of these results has already been given, for Ar+KCl, in Figs. 1.5 to 1.7, in the form of contours in the $y-p_T$ plane. Curves of constant laboratory momentum are also shown. From there, and from Figs. 3.1 and 3.2, one can see that for a reasonably complete coverage of the fireball it is necessary to achieve momentum measurement and particle identification up to about 2000 MeV/c for pions and kaons and to 5000 MeV/c for protons.

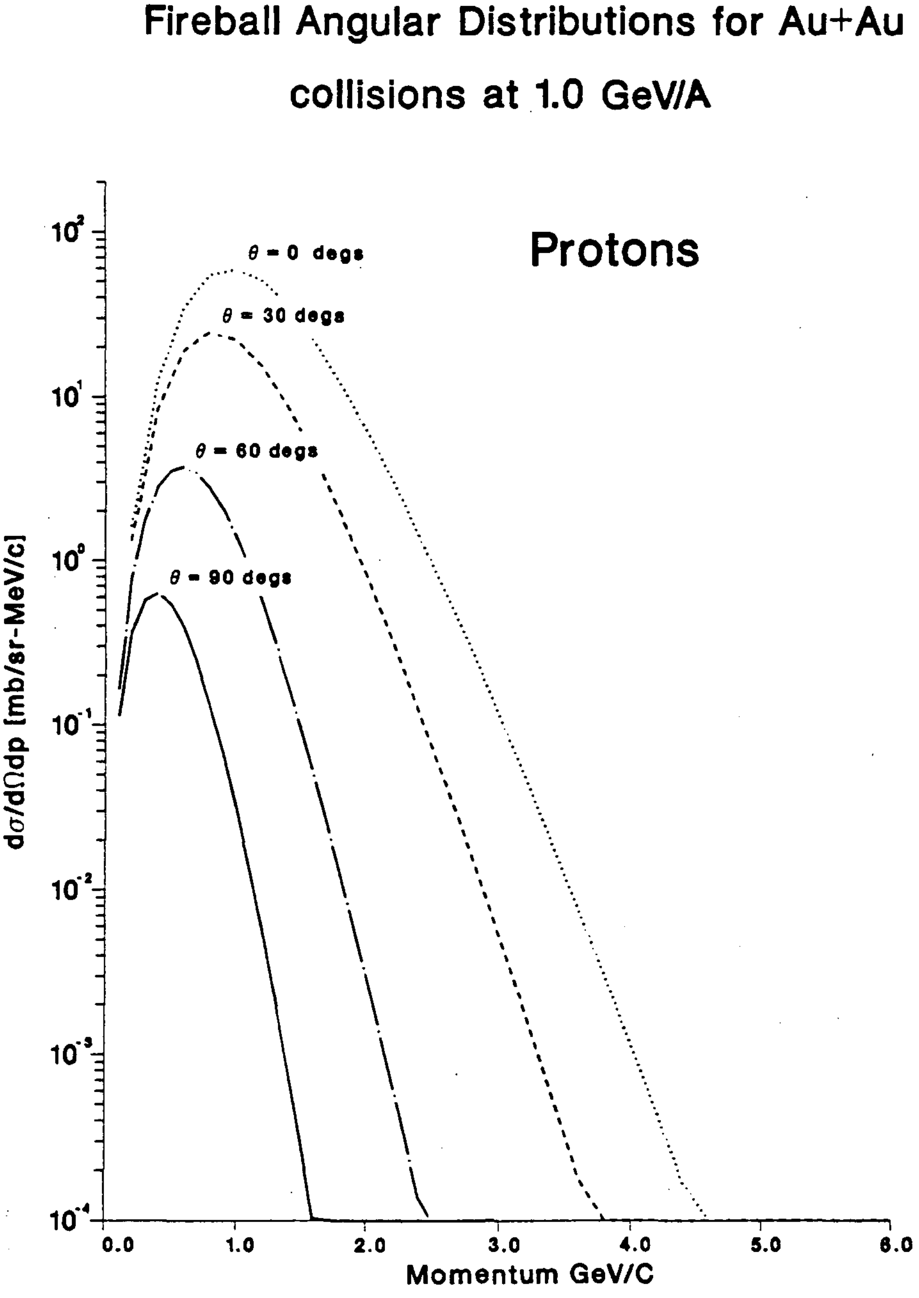

Fig. 3.2(a). Differential cross sections versus participant proton momentum for central Au+Au collisions at 1.0 GeV/A, calculated with the program Therm2.

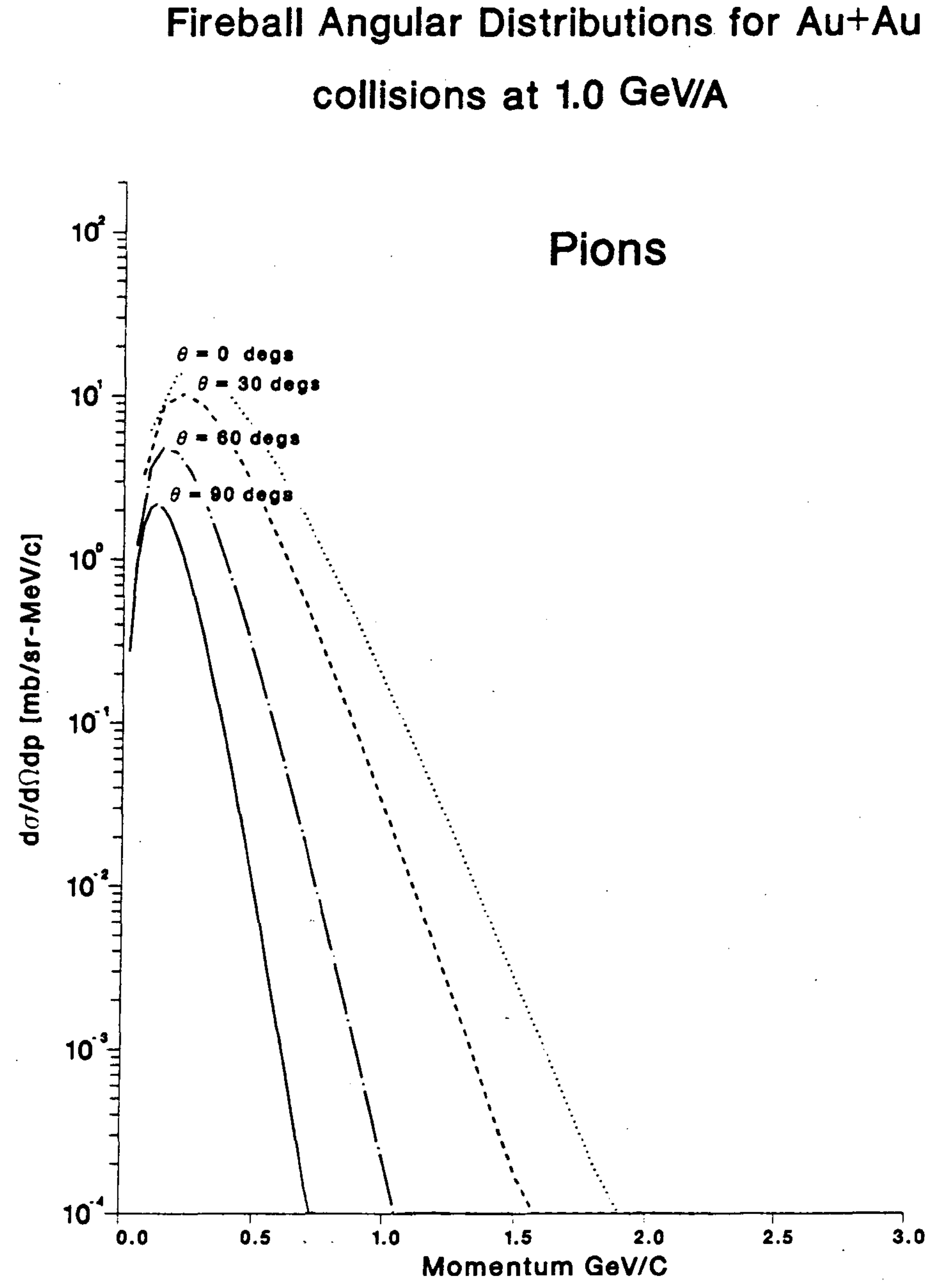

Fig. 3.2(b). Differential cross sections versus participant pion momentum for central Au+Au collisions at 1.0 GeV/A, calculated with the program Therm2.

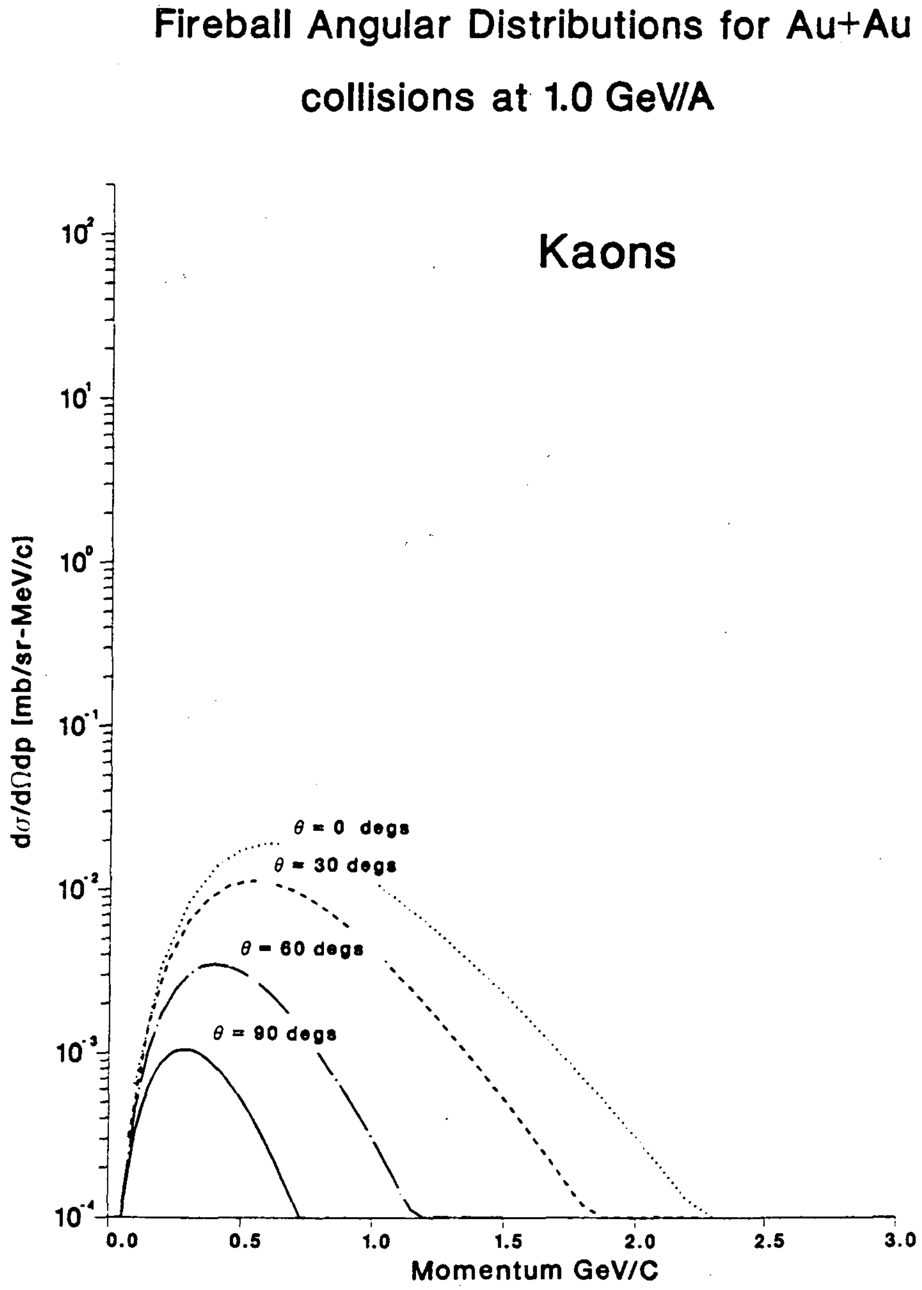

Fig. 3.2(c). Differential cross sections versus participant kaon momentum for central Au+Au collisions at 1.0 GeV/A, calculated with the program Therm2.

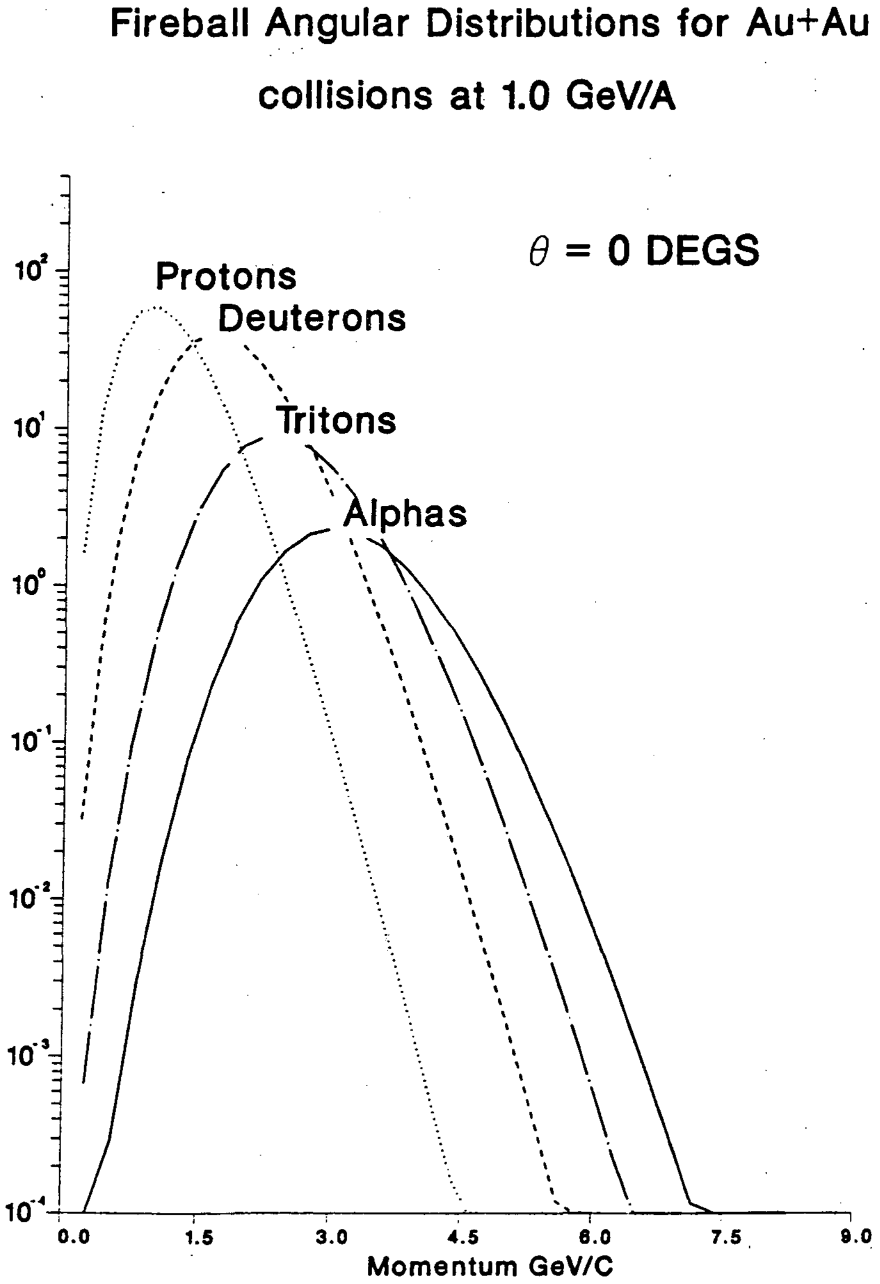

Fig. 3.2(d). Differential cross sections at $\theta = 0^o$ versus participant momentum for Au+Au collisions at 1.0 GeV/A, calculated with the program Therm2.

3.4. Particle Ratios

A characteristic of heavy ion collisions at the Bevalac is extremely large ratios between particle yields. Fig. 3.3 shows, for example, the ratios between pion, kaon, and proton yields at 17.9°. They vary by several orders of magnitude, which places severe demands on particle identification methods. In anticipation of our discussion of particle identification by means of dE/dx measurement and/or time of flight, we here present an outline of the statistical criteria to be applied to either method, or to the combination of both.

Figure 3.4 shows an example of particle identification by dE/dx measurement, taken from a PEP4 experiment [Sh 84]. It shows the distribution of dE/dx values for particles falling in a given momentum bin. It should be noted that this distribution would not be typical of results at the Bevalac, where protons almost always dominate.

The analysis of inclusive spectra is the most straightforward. Here, such a distribution as shown in Fig. 3.4 would be fitted with four free parameters corresponding to the yields of the four particles p, K, π, e, using χ^2 to determine the best fit. The widths of the distributions for the individual particles are assumed known.

For complete event analysis, this procedure does not suffice. In each event, it is required to determine on an absolute basis the identity of every particle. Since specific events have a negligible probability of being repeated, least squares fits using a large number of events cannot be carried out. Two approaches are

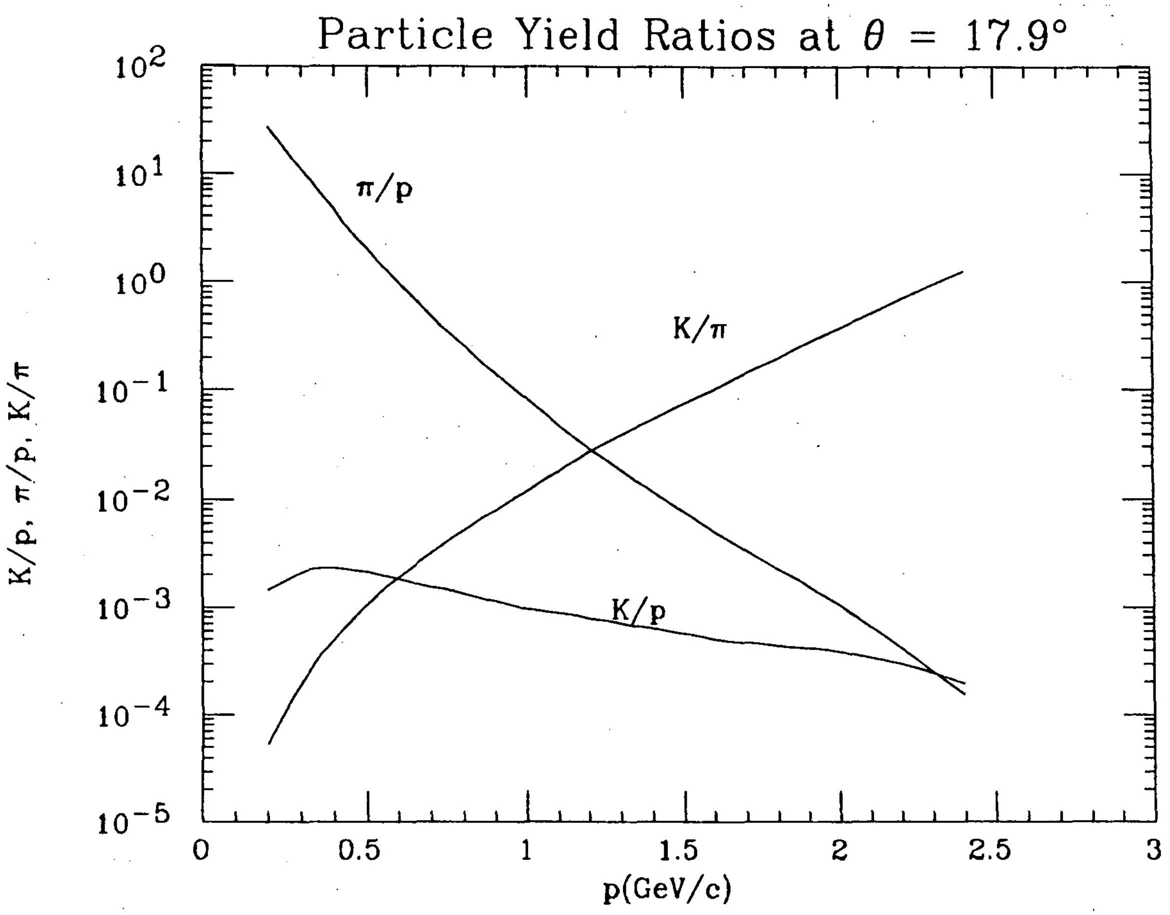

Fig. 3.3. Ratios of $(d\sigma/dpd\Omega)\times SF$ at $\theta = 17.9°$ for central Ar+KCl collisions at 1.8 GeV/A. The survival fraction $SF = exp\,(-L/\beta\gamma L_o)$, is the fraction of particles that do not decay before reaching the extremity of the TPC.

possible. One is to improve the resolution of the detector to the point where no ambiguity exists. The other, for a given detector, is to restrict the acceptance criteria, and thereby reduce the ambiguity. The shaded areas on Fig. 3.4 show how this was done by PEP4. In order to achieve sufficient purity for the p, K samples (75%) the acceptance was in each case reduced to about 25%. The acceptance and purity of the pion samples are both better than 90%.

In the above example, the acceptance for given cuts is well determined by the properties of the detector, but the purity is model dependent. In our estimates of the purity to be achieved, we have used predictions of the fireball program, Therm2. Given particle ratios at a given momentum, such as those in Fig. 3.3, it is possible to specify how many standard deviations separation in dE/dx or time of flight is necessary to achieve a desired acceptance, and purity. Table 3.2 shows such results for several acceptance levels and for 90% and 99% purity. We conclude from Table 3.2 that if the yield ratio between two particles is 1:1 we can achieve satisfactory acceptance and purity with about three standard deviations separation. However, if the ratio is 1000:1 we need about five standard deviations.

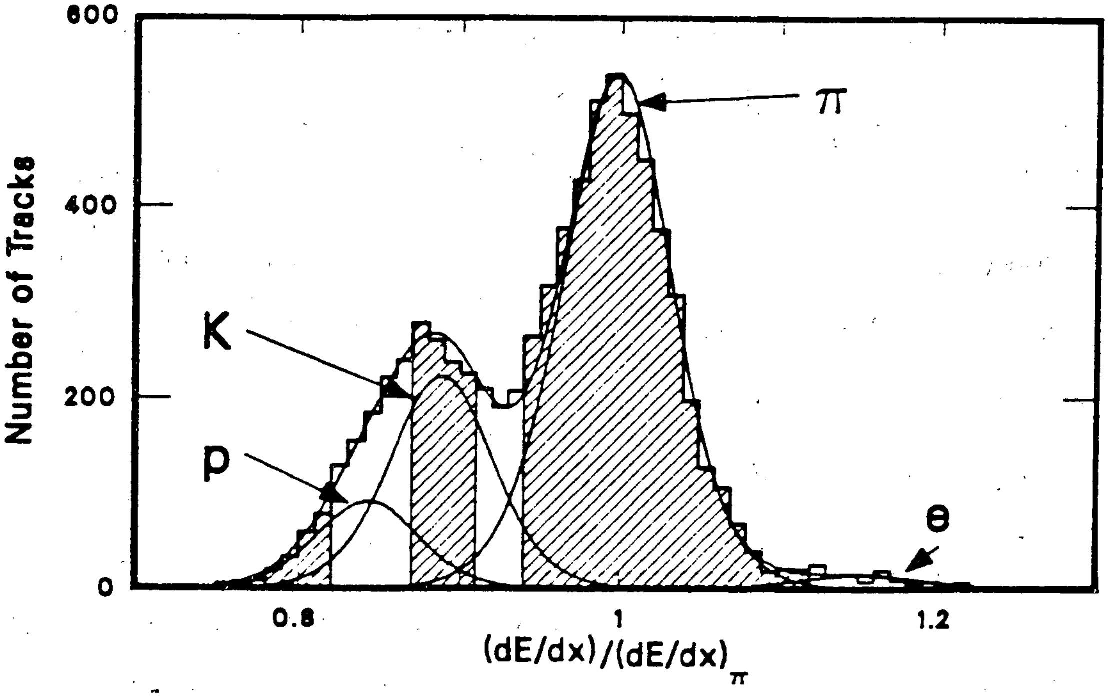

Fig. 3.4. The distribution of dE/dx in the PEP4 TPC [Sh 84] (normalized to the expected value for pions of the same momentum) for tracks with momenta between 3.7 and 6 GeV/c. The crossed hatched regions represents those particles that would be called pions, kaons and protons with the criteria given in the text.

Table 3.2

Necessary particle identification resolution for various values of acceptance and purity.

Acceptance(%)	Purity(%)	Ratio of Yields			
		1:1	10:1	100:1	1000:1
86.6 ($\pm 1.5\sigma$)	99 90	3.8 2.8	4.6 3.8	5.2 4.6	5.7 5.2
68.3 ($\pm\sigma$)	99 90	3.5 2.5	4.2 3.5	4.8 4.2	5.2 4.8
38.3 ($\pm\sigma/2$)	99 90	3.1 2.2	3.9 3.1	4.4 3.9	5.0 4.4
0	99 90	3.0 2.1	3.7 3.0	4.3 3.7	4.8 4.3

Chapter 4

4. The TPC: General Characteristics

4.1. Overall Detector Design

We have already introduced the EOS detector in Section 1.2. In this Chapter we discuss the overall design and performance of the TPC, reserving aspects that depend on the the detailed design of the endcap for Chapter 5.

The EOS TPC has been designed primarily for studies of the participant region of heavy ion collisions. However, its design is such that supplementary detectors can, at a later time, be added to cover other regions of phase space. It meets the following design goals:

The detector should:

(a) identify and measure the momentum of

- p, d, t, ^{3}He, ^{4}He
- π^+,π^-,K^+,K^-,K^0_s and Λ^0,

  with an accuracy of about 1%.

(b) have a dynamic range in the fireball c.m. system of

- 10 MeV/c up to $\sim$ 1 GeV/c for pions,
- 30 MeV/c up to $\sim$ 1 GeV/c for kaons,
- 60 MeV/c/A up to $\sim$ 2 GeV/c/A for p, d, t, ^{3}He, ^{4}He,

(c) tolerate an event rate of up to 10,000 per second;

(d) accommodate a multiplicity of about 200 charged particles per event;

(e) have as large an acceptance in solid angle as is technically feasible.

The chosen design has the following parameters:

(a) A solenoidal magnetic field centered along the beam direction, with a diameter of 2 metres, and a field strength of 1.5 Tesla.

(b) The time projection chamber is approximately 1.8 metres in outside diameter and 2 metres long. The target is placed in a central beam pipe which is evacuated and separated from the TPC. The target is located 0.5 m from the rear of the TPC, and charge is drifted toward the rear, to be measured using an endcap of approximately 25,000 pads and 1000 sense wires.

(c) The gas is 91% Ar 9% CH_4 at atmospheric pressure, and the electric field strength is 115 V/cm.

(d) The sides of the TPC are covered by a barrel array of time-of-flight detectors. The downstream end is also covered with a highly segmented array of time-of-flight detectors.

This design has the following special features:

(a) As a continuous tracking detector it has outstanding capability to resolve high-multiplicity events, including secondary vertices (Λ^0, K^0) and decays in flight (π, μ, K).

(b) As an electronic detector it can accommodate high event rates.

(c) It uses true reconstruction of events in three dimensions, and does not use projective geometry.

(d) The solenoidal magnetic field measures directly the interesting physical quantity, transverse momentum, and minimizes azimuthal biases in event shapes such as would be present with a transverse field design.

(e) The solenoidal field affects the beam and projectile fragments minimally, permitting the addition of downstream detectors if desired. Similarly, some measurements of target fragments might be achieved inside the beam pipe, if desired.

4.2. Particle Trajectories

Some useful relationships concerning the trajectory of a charged particle in a magnetic field along the beam direction are presented in Appendix I. A particle emitted from the target (on the axis of the magnet) travels in a spiral along the outside of an imaginary cylinder whose surface touches the axis and whose radius is given by:

$$\rho = \frac{p\ \cos\lambda}{0.3\ zB} \tag{4.1}$$

where ρ is in meters, the momentum p , is in GeV/c, λ is the dip angle, z is the charge of the particle in units of the electronic charge, and B is the magnetic field in Tesla. The magnetic field alters the transverse momentum p_t ($=p\ \cos\lambda$), but leaves the longitudinal momentum unchanged. The longitudinal momentum is thus obtained by measuring p_t and the dip angle λ.

A consequence of Eq. 4.1 is that in a magnet of radius R, any particle with $\rho < R/2$ does not reach the wall of the magnet but continues to spiral (all others complete less than one half turn of the spiral). For our chosen radius of 1m and a field of 1.5 T, this condition is: $p_t < 225\, z\, (MeV/c)$.

Figure 4.1 (a)-(c) illustrate some of these features. Figure 4.1(a) shows an 'enhanced' Ar+KCl event with the correct proportion of particles but 100 tracks. Figure 4.1(b) shows 100 kaons from Ar+KCl events, while Figure 4.1(c) shows 100 pions, also from Ar+KCl events. It will be seen that spiraling is most significant for pions, because of their lower mass and lower temperature.

The amount of spiraling is of interest for several reasons. For simplicity of pattern recognition it should be minimised since nearly straight tracks are easier to find. Spiraling fills up too many pixels in the TPC, adding redundant information which is generally not useful and serves to confuse other tracks. To seek an optimum, we have considered other values of the magnetic field. While it would certainly be attractive to reduce the field to improve pattern recognition, it is found that the effect on momentum resolution is disastrous. Naively we might expect the momentum resolution $\Delta p/p$ to be inversely proportional to the product BR^2. In practice the radial diffusion in a TPC is found to be roughly inversely proportional to B, so that momentum resolution is determined by the product $(BR)^2$. Our values of B and R are chosen to give sufficient momentum resolution and we accept the degree of spiralling shown.

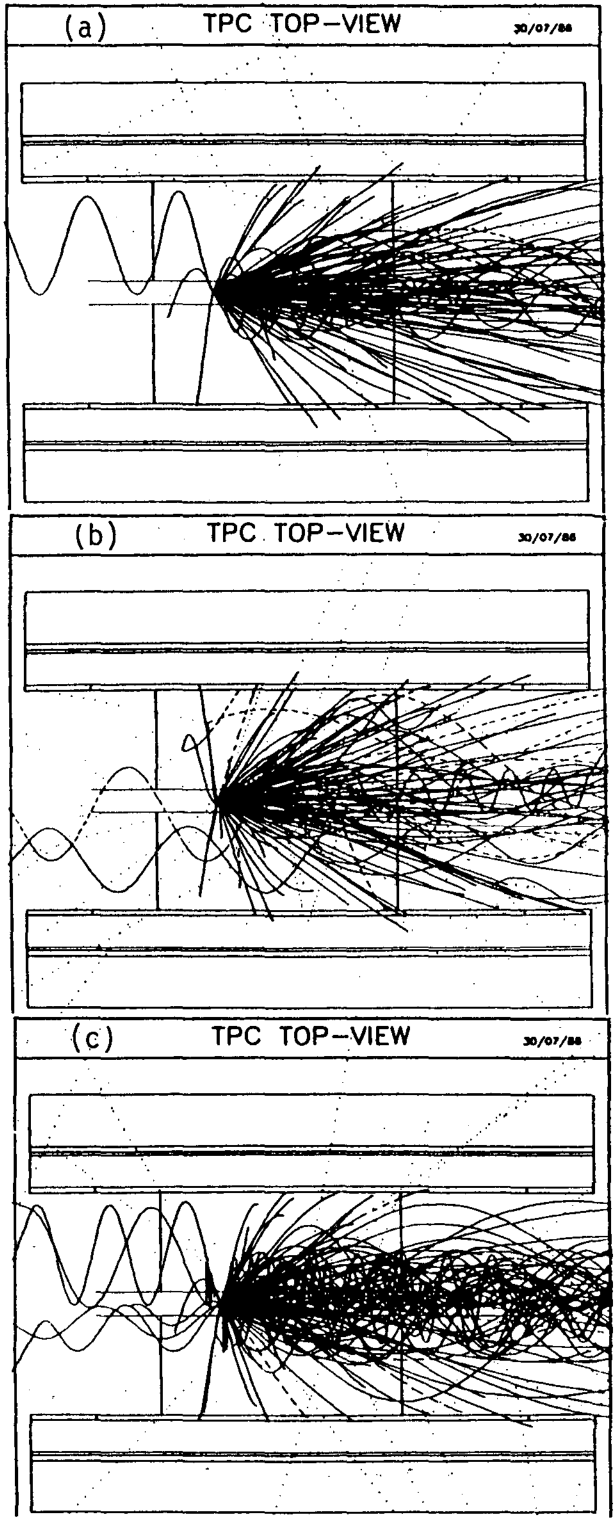

Fig. 4.1. (a) Side view of an 'enhanced' central Ar+KCl event at 1.8 GeV/A in the EOS TPC. The momentum distributions were obtained from the program Therm2, using the particle ratios and temperatures as in Table 3.1, but with 100 charged participants instead of the normal 46. Figures 4.1 (b) and (c) show 100 kaons and 100 pions from Ar+KCl events, respectively.

4.3. Diffusion

The intrinsic spatial resolution of a TPC is determined by the degree of diffusion of the ionisation electrons after they have drifted through the chamber on to the end cap. This has recently been measured as a function of magnetic field for a 91% Ar 9% CH_4 mixture [Am 86]. Diffusion is proportional to the square root of the drift distance. In a magnetic field transverse diffusion is reduced while longitudinal diffusion diffusion remains unchanged. Table 4.1 shows the results of Amendolia et al. [Am 86] extrapolated to a magnetic field of 1.5 T and a drift distance of 200 cm.

Table 4.1
Diffusion of ionization electrons. The data are extrapolated to $B = 1.5$ T and a drift distance of 200 cm based on the results of Amendolia et al. [Am 86].

		Longitudinal	Transverse
Single electron	σ (mm) fwhm (mm)	9.5 22.4	1.34 3.16
Mean of 30 electrons	σ (mm) fwhm (mm)	1.73 4.08	0.24 0.57

The values in the table for a single electron determine the width of a track projected onto the end cap, and hence the two track separation capability of the detector. The values shown for the mean of 30 electrons which is a typical number sampled by a pad on the end cap determine the accuracy with which the centroid of a track, and hence the momentum of a particle can be determined.

4.4. Momentum Resolution

The diffusion shown in Table 4.1 determines the ultimate resolution that can be achieved with the TPC. We shall show in Chapter 5 how to match this with the specific design of an end cap.

To display the momentum resolution of the TPC we have performed a simplified analytic calculation, and a detailed Monte Carlo calculation for simulated events. Appendix II shows how to derive the analytic expression, which is shown in Eq. 4.2.

$$\begin{aligned}\left(\frac{\Delta p}{p}\right)^2 &= 11.1\, A_n\, \frac{\sigma_r^2 \cos\lambda}{B^2 L^4} \cdot p^2 \\ &+ C_n\, \frac{\sigma_z^2 \sin^2\lambda \cos^2\lambda}{L^2} \\ &+ 2.95\times 10^{-3}\, \frac{1}{B^2 L\; L_R\, \cos\lambda} \cdot \frac{1}{\beta^2} \qquad (4.2)\end{aligned}$$

Here $A_n = \dfrac{720\, N^3}{(N-1)\,(N+1)\,(N+2)\,(N+3)} \approx \dfrac{720}{N+5}$.

where N is the number of equally-spaced measurements along the back;

$C_n = \dfrac{12\,(2N+1)\,(8N-3)\,N}{(N-1)\,(N+1)\,(N+2)\,(N+3)} \approx \dfrac{192}{N+5}$;

σ_r = rms radial diffusion of electrons (in m);

σ_z = rms longitudinal diffusion of electrons (in m);

λ = dip angle;

$p =$ particle momentum in GeV/c;

$B =$ magnetic field in Tesla;

$L =$ length of measured track (in m), projected perpendicular to the beam and assumed to be nearly straight;

$L_R =$ radiation length of the gas (in m);

$\beta =$ particle velocity in units of the speed of light.

The first term (proportional to p^2) arises from the determination of the transverse momentum p_t, the second from the determination of the dip angle λ, and the third (proportional to $1/\beta^2$) from multiple scattering in the TPC gas.

To make numerical estimates we fixed the values of σ_r and σ_z at their maximum values corresponding to 200 cm drift. Following the geometry of the chamber, we find $L = 0.8$ for $\lambda < \tan^{-1}(1.5/0.9)$, i.e., $\theta > 31°$, and $L = \dfrac{1.5}{\tan\lambda} - 0.1$ for $\theta < 31°$. We set the number of measurements equal to $L/0.01$, and $L_R = 130$ m.

The results for the three terms in the equation are shown separately in Fig. 4.2. Here the resolution given by the Curve 1 must be multiplied by p (GeV), that of Curve 3 must be multiplied by $1/\beta$, and then all three contributions to the resolution should be added in quadrature. The three curves may be summed without any multiplicative factor for 1 GeV/c pions, for which $\beta \approx 1.0$.

For low energy particles curve 3 dominates the result, and for high energy particles curve 1. Curve 2 is never the most important. The rise at small angles,

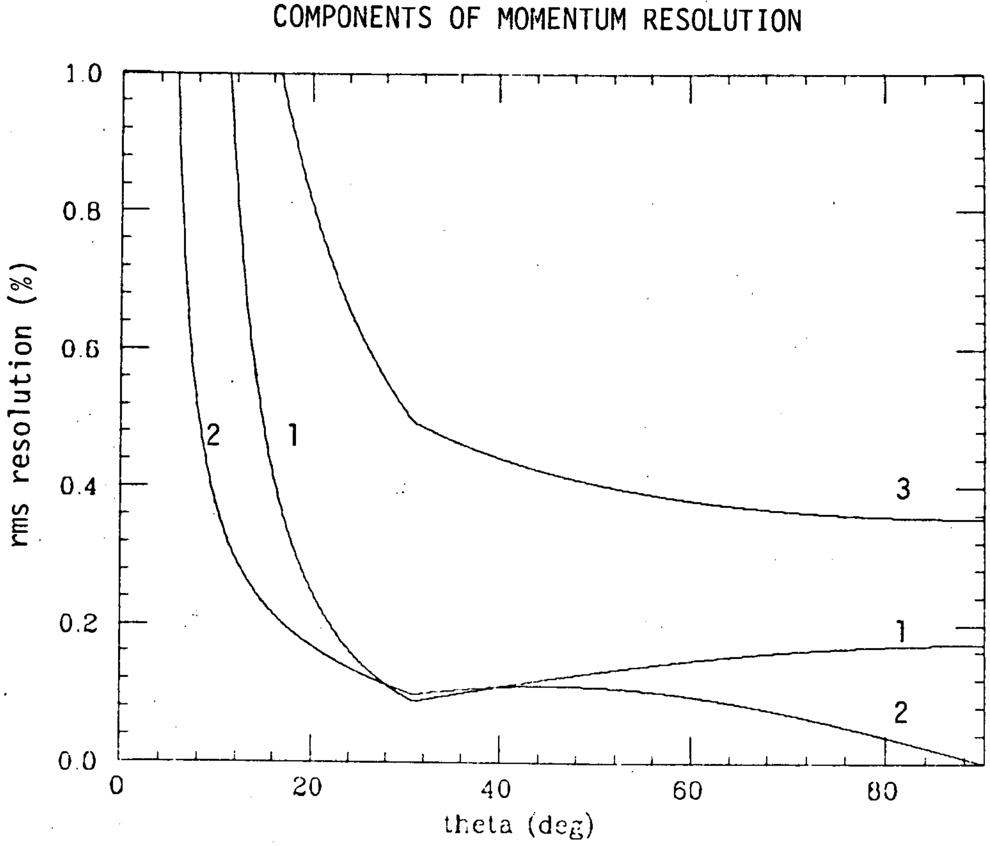

Fig. 4.2. Contributions to the momentum resolution in the TPC from the three terms of Eq. 4.2. The resolution given by curve 1 must be multiplied by p (GeV/c), that of curve 3 must be multiplied by $1/\beta$, and all three contributions must then be summed in quadrature.

intrinsic to measurements in a solenoid, is aggravated by the truncation of the TPC at 31° and also by the reduced number of measurements that can be made on the reduced length of track. If improved momentum resolution is needed for the most forward angles, one possibility would be to add drift chambers in that region.

Figure 4.3 shows the resolution as a function of angle for protons of various energies. It is typically of the order of 1% for angles greater than 31° , but deteriorates in the forward direction.

To test the overall momentum accuracy in a typical event, a Monte Carlo calculation was carried out using information supplied by the GEANT program for a sample of Au+Au events at 1.0 GeV/A. This calculation avoided many of the approximations involved in deriving Eq. 4.2. The results are shown in Fig. 4.4. It is seen that the typical momentum error is about 1%.

4.5. dE/dx Resolution

The TPC technique is specially useful for the identification of particles by dE/dx measurement, since it provides the large number of independent samples of dE/dx within a given length of track that has been shown to be essential to achieve high resolution. A summary of the theory of energy loss in thin samples is given in Appendix III. Here we present only the most important results.

For a given thickness of gas, the most probable energy loss is a universal function of $\eta \equiv \beta/\sqrt{1-\beta^2}$. This is shown in Fig. 4.5 for 1 cm of Ar at atmospheric pressure, normalized to its minimum value.

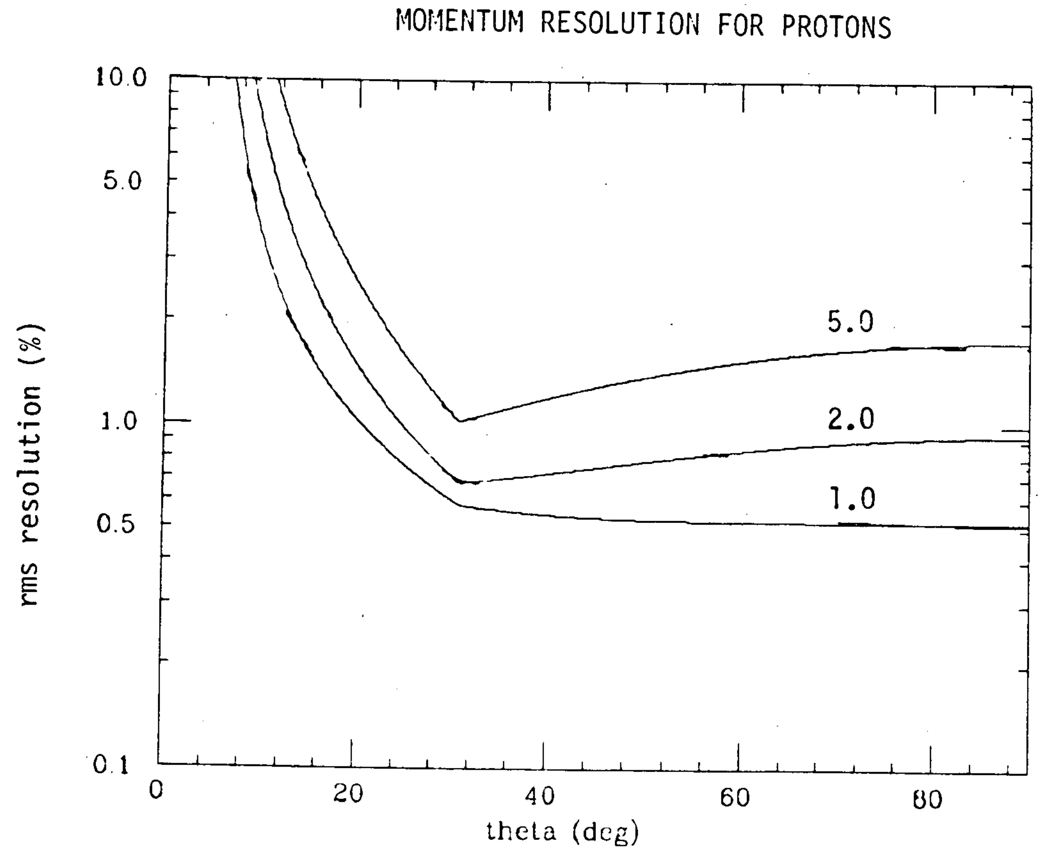

Fig. 4.3. Momentum resolution as a function of angle is shown for protons of various momenta. The curves are labelled in GeV/c.

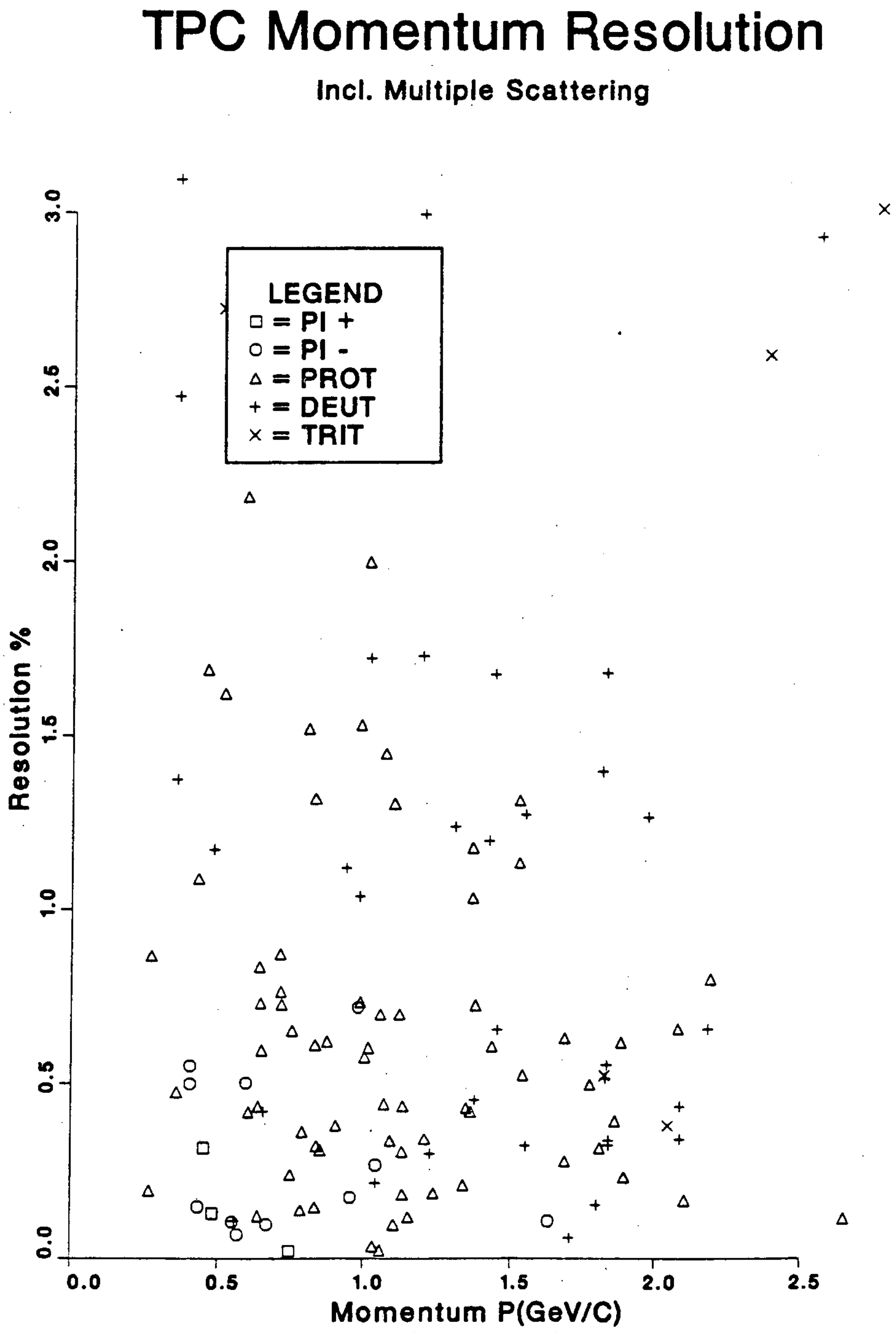

Fig. 4.4. A Monte Carlo simulation of Au+Au events at 1.0 GeV/A showing that the typical momentum resolution is ≈1%.

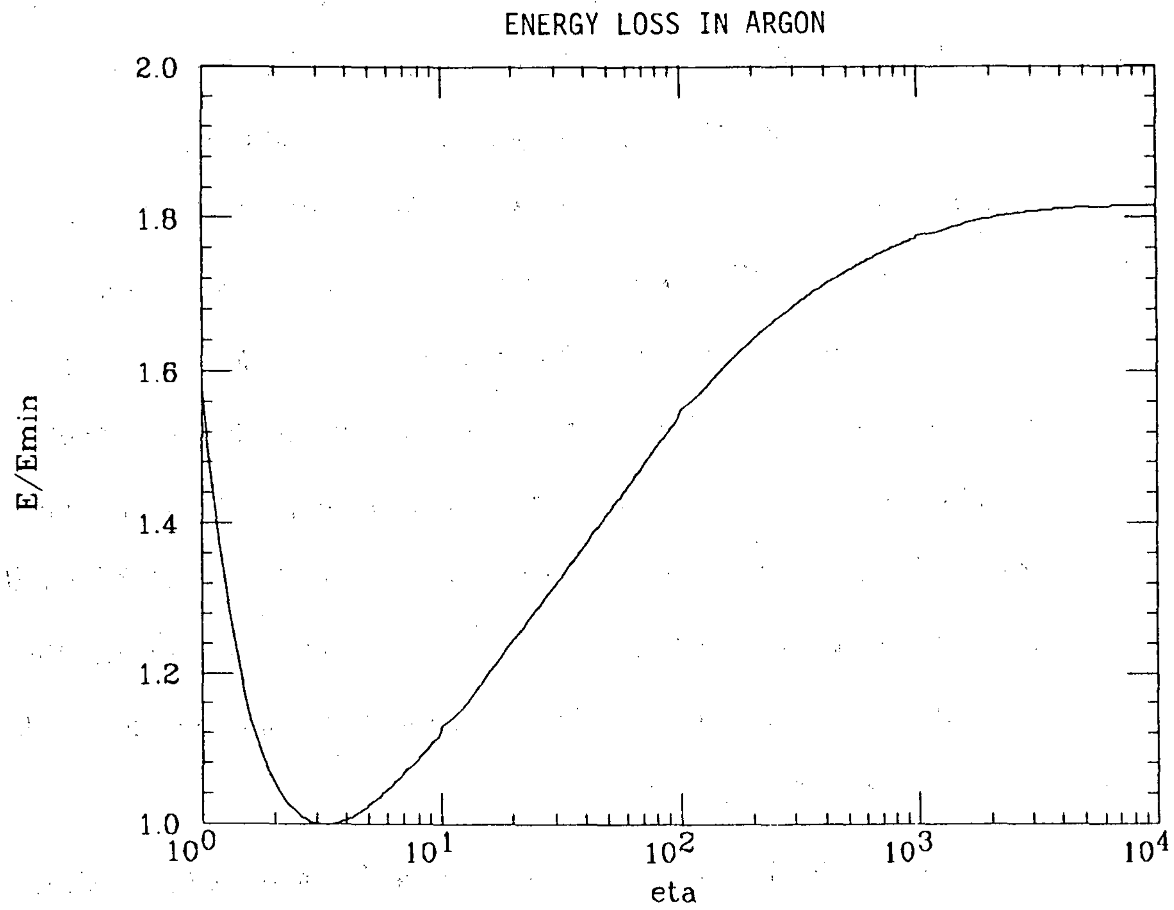

Fig. 4.5. dE/dx normalized to the minimum ionization value, as a function of η, for 1 cm of Argon at a pressure of 1 atm.

Figure 4.6 shows the energy loss in 1 cm of Ar at atmospheric pressure, as a function of momentum, for various particles: e, π, K , p , d , t . This energy loss leads to production of about 40 ion pairs per cm at the minimum, so that the signals to be measured in the TPC will be quite small. Examination of Fig. 4.6 will show that if a resolution of 10% is achieved in dE/dx, identification of π, K will be achieved up to 0.8 GeV/c, of protons up to 1.3 GeV/c, of deuterons up to 2.3 GeV/c and tritons up to 3.3 GeV/c. This covers the majority of the particles produced in the fireball. To obtain particle identification at higher momenta, the EOS detector will be provided with the time of flight array described in Chapter 6. With two completely independent methods of particle identification we can obtain valuable redundancy for the lower momenta, and combine the two methods at the higher momenta to obtain greater discrimination than could be obtained with either method alone.

Calculation of the fluctuations in energy loss in small samples requires a detailed understanding of the energy transfer processes in the specific gas under consideration. Monte Carlo calculations using empirical photoabsorption cross sections have been reported by the authors of [Er 77], [La 80] and [Al 80]. Figure 4.7 shows a measured distribution for 1 cm samples in the UA1 central detector, as well as the theoretical prediction [Ca 82]. The long tail of the distribution, which persists for samples up to 1 m or more, is not satisfactory for particle discrimination. However, by taking the truncated mean (the mean of the lowest 60% or 70%) of a large number of samples, a near-Gaussian distribution is obtained, as shown in Fig. 4.8.

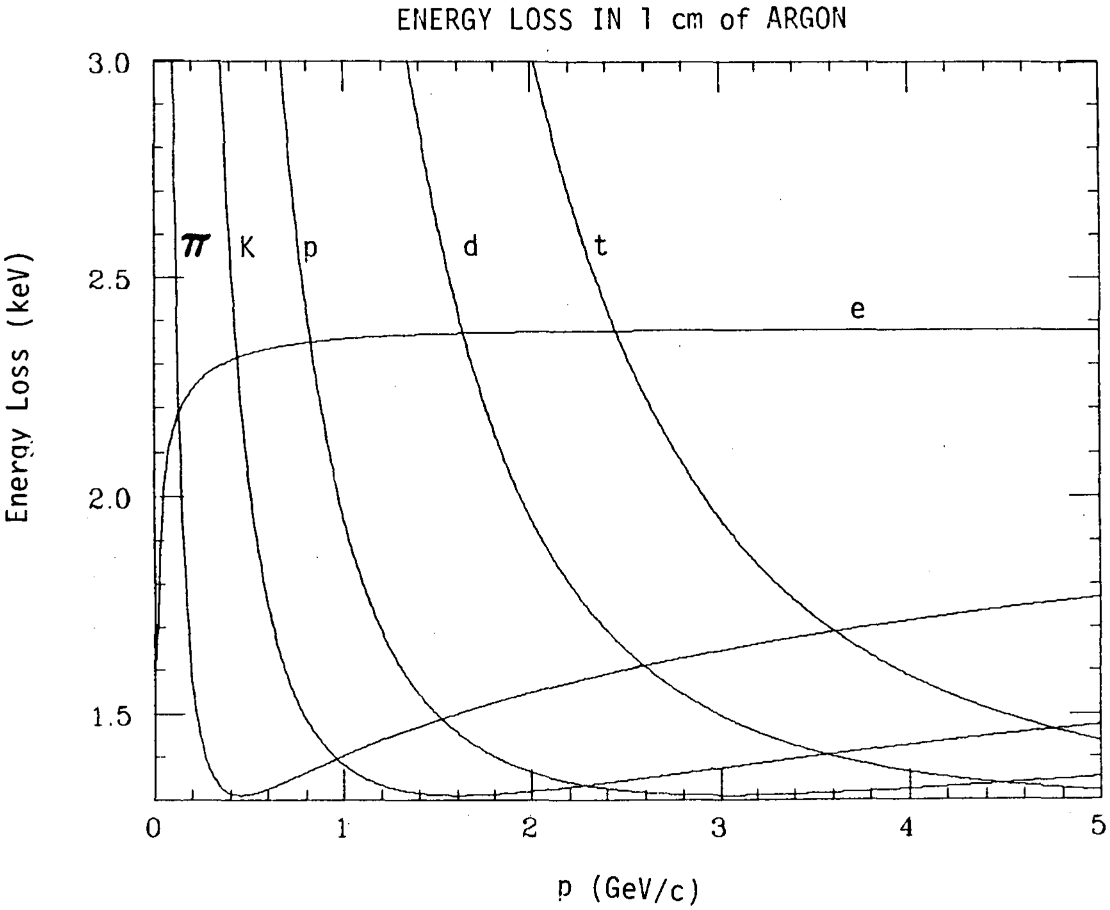

Fig. 4.6. Energy loss in 1 cm of argon at 1 atm is plotted against momentum for electrons, pions, kaons, protons, deuterons, and tritons.

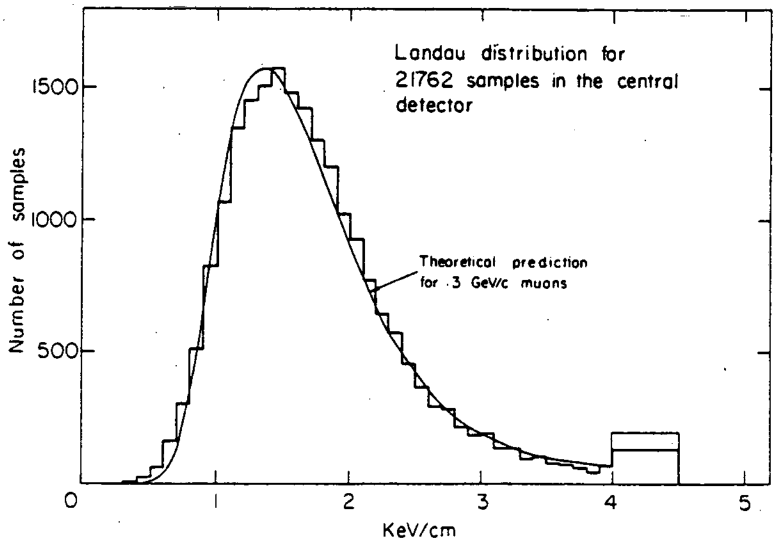

Fig. 4.7. Distribution of energy loss per cm in the UA1 central detector [Pl 82], for a mixture of 60% ethane and 40% argon at atmospheric pressure. The sample size is 1 cm.

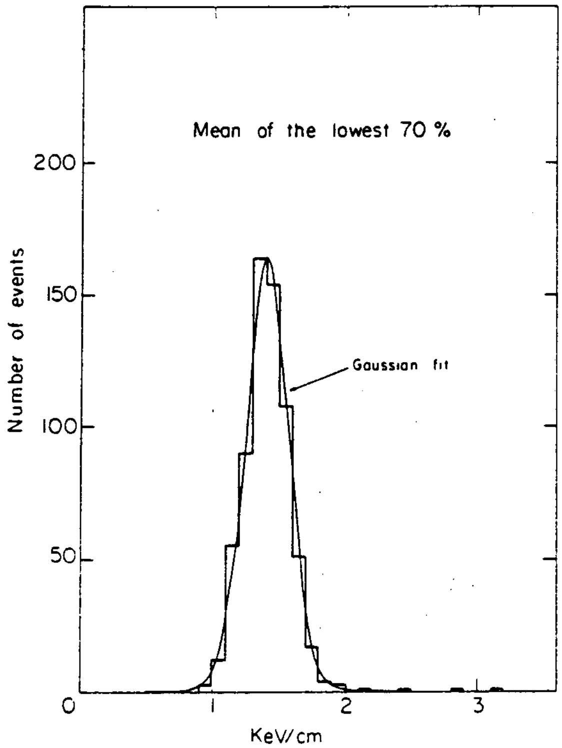

Fig. 4.8. Mean of the lowest 70% of 34 measurements, each 1 cm thick, in the UA1 central detector [Pl 82].

Allison and Cobb [Al 80] have provided a semi-empirical formula to predict the resolution obtainable in a variety of circumstances. If there are n samples, each of thickness X cm, at a pressure of P atmospheres of argon, the resolution is given approximately by:

$$R\,(\%\ \mathrm{FWHM}) = 96\ n^{-0.46}(XP)^{-0.32} \tag{4.3}$$

If the Bohr theory were valid, both exponents in Eq. 4.3 would be the same, equal to -0.5, and R would be proportional to $(nXP)^{-0.5}$. Thus only the total thickness of gas would matter. However, Eq. 4.3 can be rearranged as

$$R\,(\%\ \mathrm{FWHM}) = 96\ n^{-0.14}(nXP)^{-0.32} \tag{4.4}$$

This shows that for a given thickness, nXP, the resolution can be improved by subdividing the gas into smaller and smaller samples. Remarkably this has been tested and found accurate for 1 m total track length subdivided into 57, 230 and 1805 samples [Lu 82], as shown in Fig. 4.9. If Eq. 4.3 is generalized to other gases it becomes

$$R\,(\%\ \mathrm{FWHM}) = 81\ n^{-0.46}\left(\frac{Kx}{\beta^2 I}\right)^{-0.32} \tag{4.5}$$

where the variables are defined in Appendix III.

Equation 4.5 shows that the resolution should improve as the ionization potential I is decreased. Isobutane (I = 52.1 eV) should have a resolution 1.8 times smaller than argon (I = 210 eV), while Ne, Ar, and Xe should have about

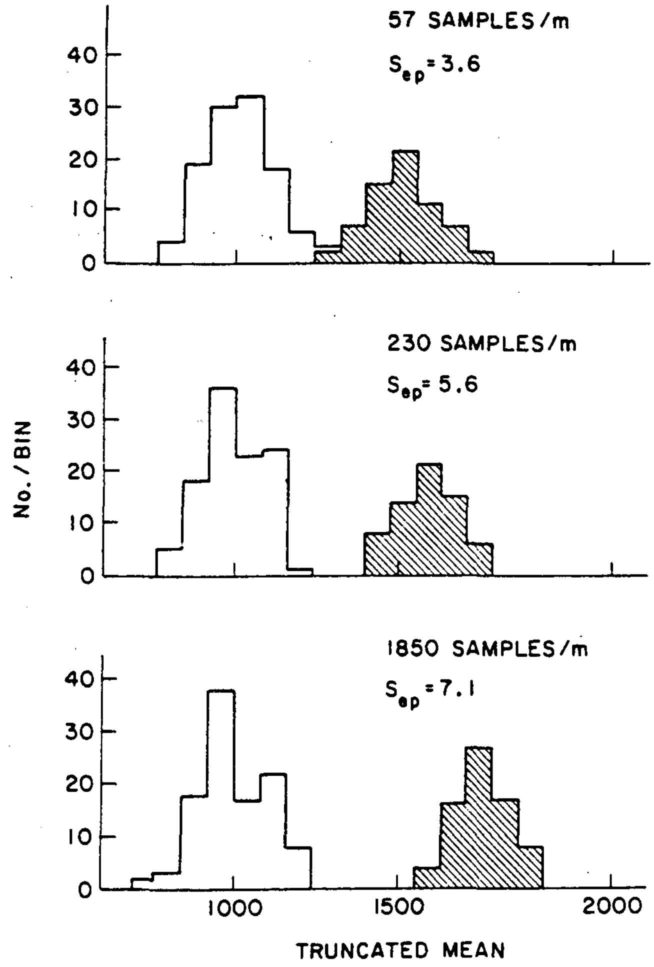

Fig. 4.9. The truncated mean of energy loss for 110 proton tracks (open histogram) and 72 electron tracks (shaded histogram). The results are shown for 3 different sample sizes. Each track is 1 meter long. S_{ep} is the seperation between the distributions [Lu 82].

the same resolution. These conclusions have been verified by Lehraus [Le 82], [Le 83].

We have selected 91% Ar 9% CH_4 as the gas for our TPC because it has many attractive properties and it is well studied. Atmospheric pressure is chosen because it is technically much simpler and also allows us to add external detectors: at our energy the secondary particles cannot penetrate great thicknesses of material. The use of complex hydrocarbons is rejected because signal attenuation by electron attachment would be too great [Le 82].

Once the gas and pressure are chosen, the overall dimension nX and the number of samples, n , determine the resolution. In our detector nX is typically between 80 cm and 160 cm. For 80 samples, obtained from measurements on the pads, the corresponding resolution (fwhm) is between 12.8% and 10.2%. For 160 samples, obtained from measurements on the sense wires, the resolution is improved to between 11.6% and 9.3%. For resolution at energy losses away from the minimum, see Appendix III. Figure 4.10 shows the discrimination to be obtained for 80 samples and a path length of 120 cm, as a function of momentum.

4.6. Magnetic Field

The average velocity of a swarm of electrons drifting in a combined $\vec{E}$ and $\vec{B}$ field is:

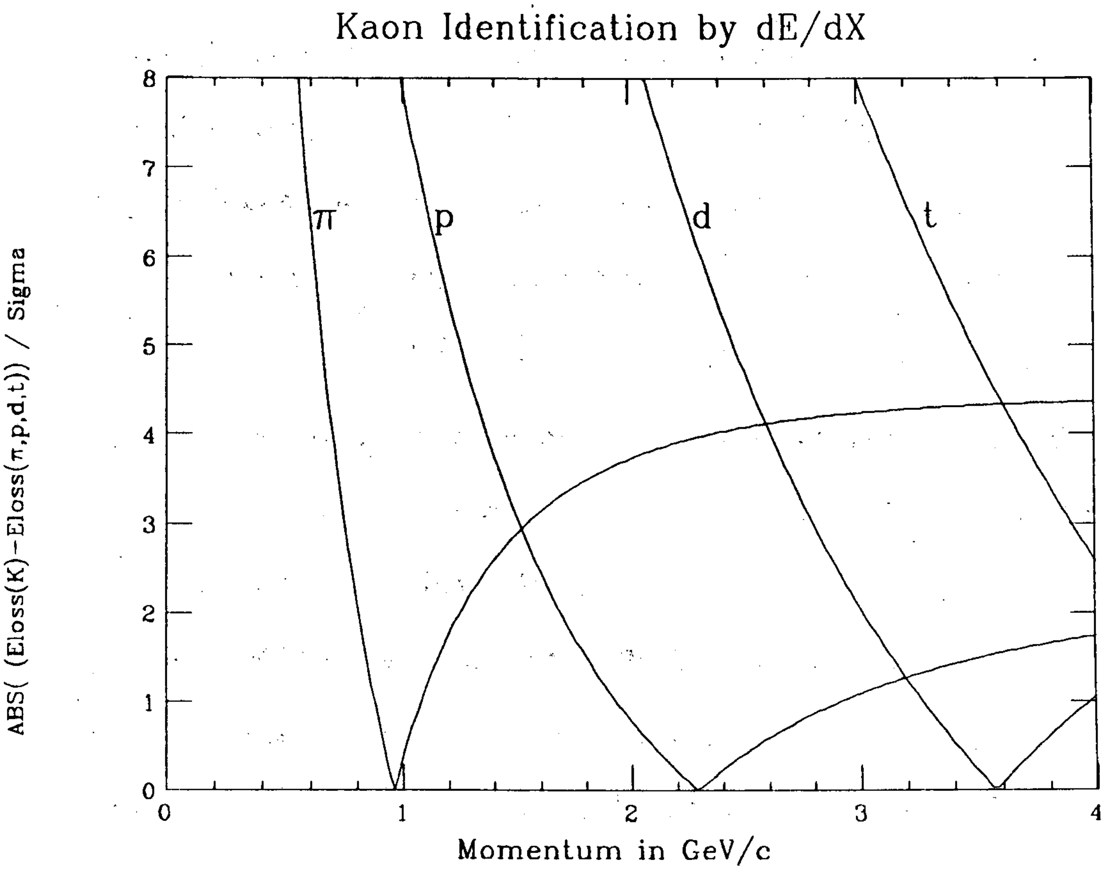

Fig. 4.10. The difference in energy loss between kaons and pions, protons, deuterons, and tritons, as a function of momentum. The calculation is for a path length of 120 cm, with 80 samples. The curves are normalized to the expected dE/dx rms error.

$$\vec{w} = \frac{\mu}{1 + \omega^2\tau^2} \left[\vec{E} + \frac{\omega\tau}{B} \vec{E} \times \vec{B} + \frac{\omega^2\tau^2}{B^2} (\vec{E} \cdot \vec{B}) \vec{B} \right] \tag{4.6}$$

where μ is the mobility, τ is the mean time between collisions, and $\omega = \frac{eB}{m}$ is the electron cyclotron frequency. The values of μ and τ depend on the gas, gas pressure, and temperature, and on the electric and magnetic field strengths. In the EOS TPC the value of μ will be 5.05 cm/μs, and $\omega\tau$ will be approximately 7.0 [Am 86]. These values are not applicable close to the sense wires, where the electric field becomes very strong.

For $\vec{E}$ exactly parallel to $\vec{B}$, the electrons drift along the common direction. In other situations the drift direction depends on the value of $\omega\tau$. For small $\omega\tau$ the electrons follow the $\vec{E}$ field, while for large $\omega\tau$ they follow the $\vec{B}$ field. In the EOS TPC $\omega\tau$ is large, but not sufficiently large that we can neglect the $\vec{E} \times \vec{B}$ term in Eq. 4.6. To estimate the effect of field inhomogeneities, we first consider the effect of a small radial component in the $\vec{B}$ field, which will be the major source of error in a solenoidal magnet.

Let $\vec{E} = E_z \hat{z}$ and $\vec{B} = B_z \hat{z} + B_r \hat{r}$, where $\hat{z}$ and $\hat{r}$ are unit vectors in the longitudinal and radial directions, and where $B_r << B_z$. Equation 4.6 then becomes

$$\vec{w} = \mu E_z \left[\hat{z} + \frac{B_r}{B_z} \left(\frac{\omega^2\tau^2}{1 + \omega^2\tau^2} \hat{r} + \frac{\omega\tau}{1 + \omega^2\tau^2} \hat{\xi} \right) \right] \tag{4.7}$$

where $\hat{\xi}$ is an azimuthal unit vector equal to $\hat{z} \times \hat{r}$.

After integrating Eq. 4.7 over the drift time we obtain

$$\Delta z = \int_{z}^{-1} dz$$

$$\Delta r = \frac{\omega^2\tau^2}{1+\omega^2\tau^2} \cdot \frac{1}{B_z} \int_{z}^{-1} B_r \; dz$$

$$\Delta \xi = \frac{\omega\tau}{1+\omega^2\tau^2} \cdot \frac{1}{B_z} \int_{z}^{-1} B_r \; dz \tag{4.8}$$

for an electron produced at z and drifted to $z = -1$ m, the end cap location (the TPC extends between $z = \pm\, 1$ m). Inserting $\omega\tau = 7$ gives

$$\Delta r = \frac{49}{50} \cdot \frac{1}{B_z} \int_{z}^{-1} B_r \; dz$$

$$\Delta \xi = \frac{7}{50} \cdot \frac{1}{B_z} \int_{z}^{-1} B_r \; dz = \frac{1}{7} \Delta r \tag{4.9}$$

The most significant electric field variations are not necessarily radial, but for symmetry with the discussion of the magnetic field we consider $\vec{B} = B_z \; \hat{z}$ and $\vec{E} = E_z \; \hat{z} + E_r \; \hat{r}$, where $E_r << E_z$. We find

$$\vec{w} = \mu \, E_z \left[\hat{z} + \frac{E_r}{E_z} \left(\frac{1}{1+\omega^2\tau^2} \, \hat{r} - \frac{\omega\tau}{1+\omega^2\tau^2} \, \hat{\xi} \right) \right] \tag{4.10}$$

which leads to

$$\Delta r = \frac{1}{50} \cdot \frac{1}{E_z} \int_z^{-1} E_r \, dz$$

$$\Delta\xi = -\frac{7}{50} \cdot \frac{1}{E_z} \int_z^{-1} E_r \, dz = -7 \, \Delta r \tag{4.11}$$

Equation 4.11 shows that the expected radial displacement due to a radial electric field has been reduced by a factor of 50 as a result of the presence of the magnetic field (via $\omega\tau$). The azimuthal displacements introduced by the $\vec{E} \times \vec{B}$ term, while small, are not necessarily negligible.

We will not examine the electric field further, except to discuss space-charge effects in Section 5.4. Electric field problems in the EOS TPC will essentially be the same as in other atmospheric-pressure TPC's such as ALEPH and DELPHI. We, like they, will benefit greatly from the very extensive studies of electric fields carried out by the PEP-4 collaboration [Va 82]. Our magnetic field, on the other hand, is potentially a problem because one end of the magnet is open (see Fig. 1.1). We have therefore made numerical estimates of the expected effects due to magnetic field non-uniformity.

The effect of the displacements given by Eq. 4.8 on the analysis of a specific particle track is complex. The value of the integral is different for each point on the track. Figure 4.11 shows the magnetic field lines inside a solenoid, with an exaggerated radial component. The target is represented by T, and the arrows TA and TB represent two straight tracks. We note that the radial displacement of a field line over a longitudinal distance dz is equal to $B_r/B_z \; dz$. Hence the total radial displacement over the distance from z to $z = -1$ is equal to

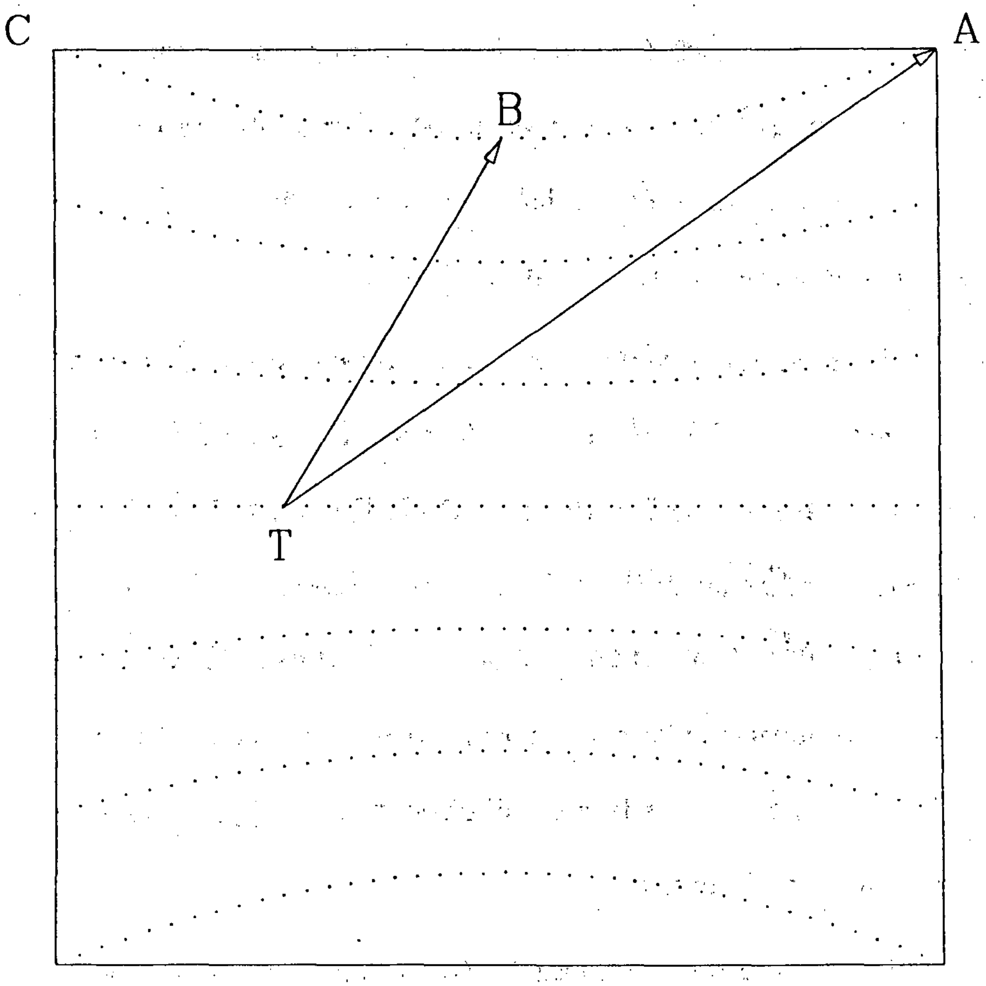

Fig. 4.11. An exaggerated version of the radial distortions of the magnetic field lines inside a solenoid of a TPC. The target is represented by T. TA and TB represent two straight tracks.

$\int_{z}^{-1} B_r / B_z \, dz$. This, in our approximation of a constant B_z, and apart from the factor $\frac{49}{50}$, is equal to Δr in Eq. 4.9. Thus we can consider that the radial motion of a drifting electron is closely described as following the field lines, as shown in Fig. 4.11. Electrons produced at T drift along the axis with no corrections, since $B_r = 0$ at $r = 0$. Electrons produced at A and B drift along the same field line and arrive at the same point on the end cap. However, the correction is zero for A, because of the symmetry of the field, and maximal for B.

A detailed calculation of these effects involves using a Monte Carlo program to generate tracks, and then to "swim" the ionization electrons through the magnetic field, which needs to be known everywhere in the TPC. In order to obtain analytic expressions we devised a model magnetic field close to that expected for the TPC. We first calculated numerically the field within a solenoid of diameter 2m and length 4m. We then adopted the expressions $B_z = 1.5$, $B_r = 0.1\, rz$ as a reasonable approximation to the field in Tesla for the central volume of length 2m and diameter 2m. Figure 4.12 shows the calculated values of B_r as a function of r and z and our approximation to them.

Two types of tracks are simple and informative to consider. First we consider the errors introduced in the measurement of a straight track, originating from the target at $r = 0$, $z = -0.5$ m. Figure 4.13 shows the calculated values of Δr and $\Delta \xi$, obtained using Eq. 4.9, plotted as a function of r for points along the track. Tracks below $\theta = 30°$ exit at the end of the chamber so there is no correction to be made at the end point (cf. track TA in Fig. 4.11). Tracks at

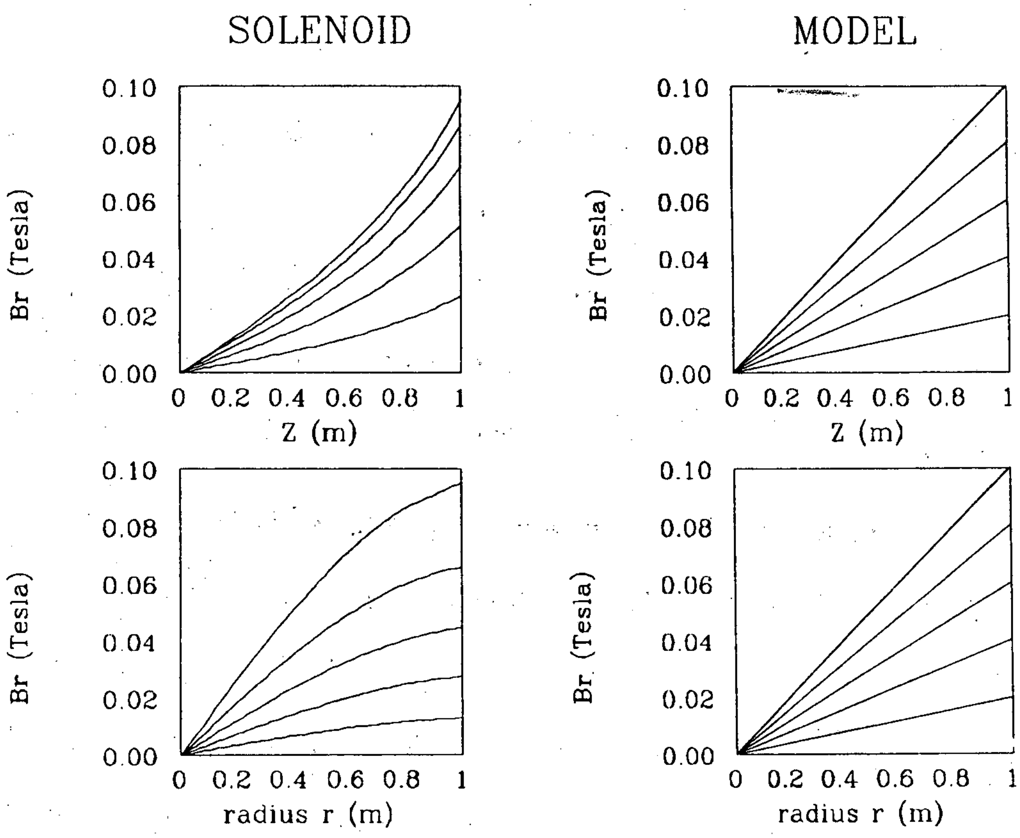

Fig. 4.12. B_r as a function of r and z, for a solenoid and for a model of the solenoidal field.

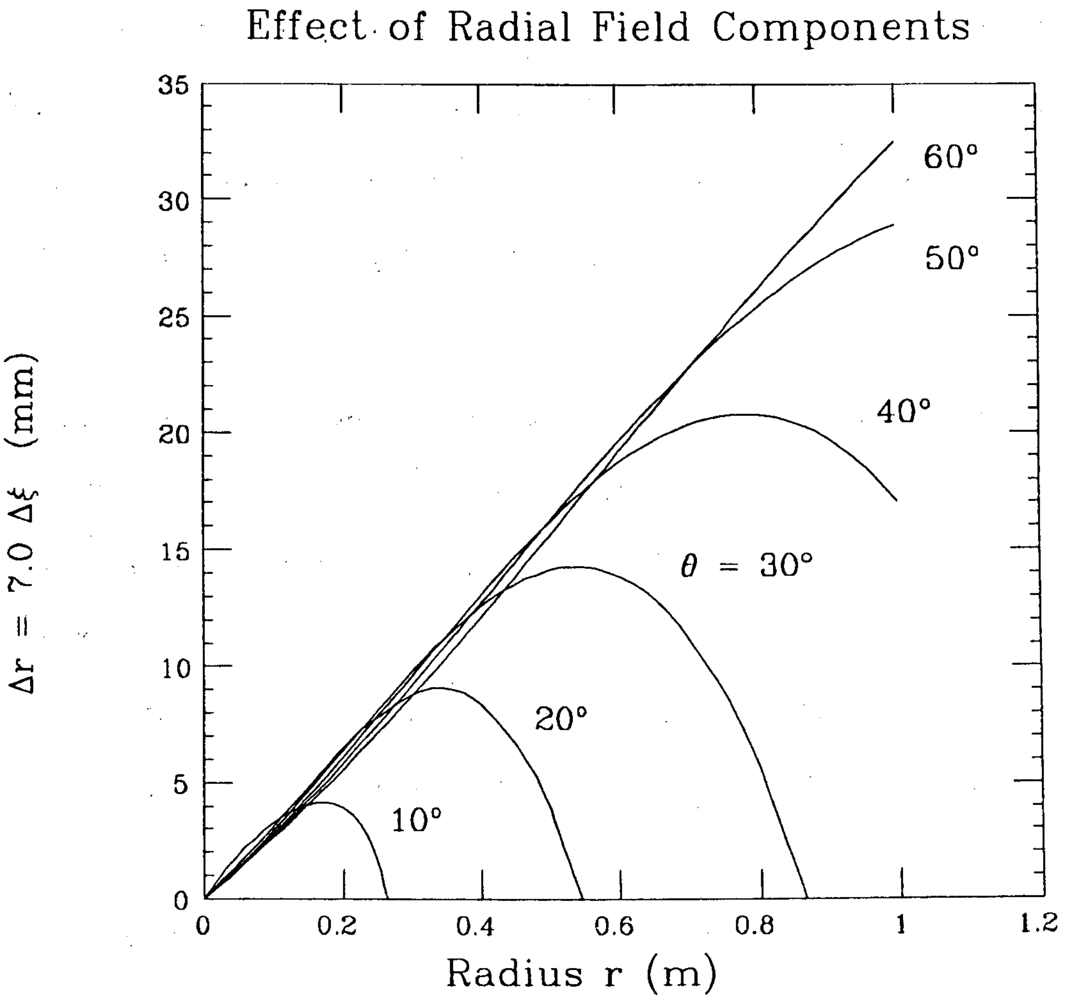

Fig. 4.13. The radial displacement Δr and azimuthal displacement $\Delta\xi$ of drifting electrons as a function of r, calculated for the model field and straight tracks at various values of θ.

about 60° travel through the central part of the chamber (cf. track TB in Fig. 4.11) and have the largest correction. The linear dependence of $\int B_r \; dz$ on r is characteristic of a solenoid and is reflected in our parameterization of the field.

For the large angle tracks, where Δr and $\Delta \xi$ depend linearly on r, the effect of the non-uniformity in field is to produce an apparent change of the *angle* of the track. For tracks between $\theta = 45°$ and $\theta = 90°$ the angle shift is approximately 0.9 sin 2θ in θ and 0.2 in the azimuthal angle ϕ, both measured in degrees.

For the smaller-angle tracks, in particular those below 30°, the displacements would be more likely to interpreted as a *momentum* shift. For the 30° track the sagitta of the projection on the end cap would have a value of 2 mm (the maximum of $\Delta \xi$ as shown in Fig. 4.13). This corresponds to a transverse momentum of 2.7 GeV/c (or actual momentum of 5.4 GeV/c) instead of the true value of infinity. The direction of curvature would suggest a positive track. Straight tracks at 10° and 20° would also appear positive at about the same momentum. Similarly, negative tracks with a true momentum of 5.4 GeV/c would appear to be straight.

The other type of track that can simply be considered is the spiralling track. Here the largest effect would be for a spiral of diameter 1m, which just reaches the edge of the chamber and corresponds to a momentum of 0.225 z GeV/c where z is the charge on the particle. Portions of the track near $r = 0$ would be unaffected. Portions of the track, if any, near $r = 1$, $z = 0$ would be maximally affected, with a radial displacement of about 3 cm, or 3%. As the particle spiralled through the chamber it would experience all of the field distortions and be difficult to fit unless they were taken into account.

We now consider the relationship of our model field to the expected field. Oxford Instruments, Ltd., have provided us with a preliminary design for the magnet (shown in Fig. 1.1) and have calculated properties of several configurations of coil windings, including the effect of the iron, which we have not included in our model. The configuration of coil and yoke is shown in Fig. 4.14. The coil is 3.6 m long and 2.2 m diameter. The values of $\int B_r \, dr$ are about 30% worse than in our model, if a uniform current density is used throughout the coil. By dividing the coil into three segments A , B , C as shown in the figure, and adjusting the currents separately, the field shown in Fig. 4.15 was achieved. This is better than our model by a factor of two, i.e., straight tracks would appear to have a momentum of about 11 GeV/c, for a singly charged particle. It is expected that further optimization of the parameters of the magnet will produce at least another factor of two improvement. This would be satisfactory, but the field would still need careful calibration.

To calibrate the magnetic field to the accuracy needed to achieve precision equal to the resolution shown in Figs. 4.2–4.4 a position accuracy of 0.05 mm in space is needed. This can be provided by a laser beam, and the ionization produced by the laser serves to simulate idealized and perfectly straight tracks against which the TPC can be calibrated. Measurements can be repeated identically many times, to improve accuracy, and can be made periodically throughout

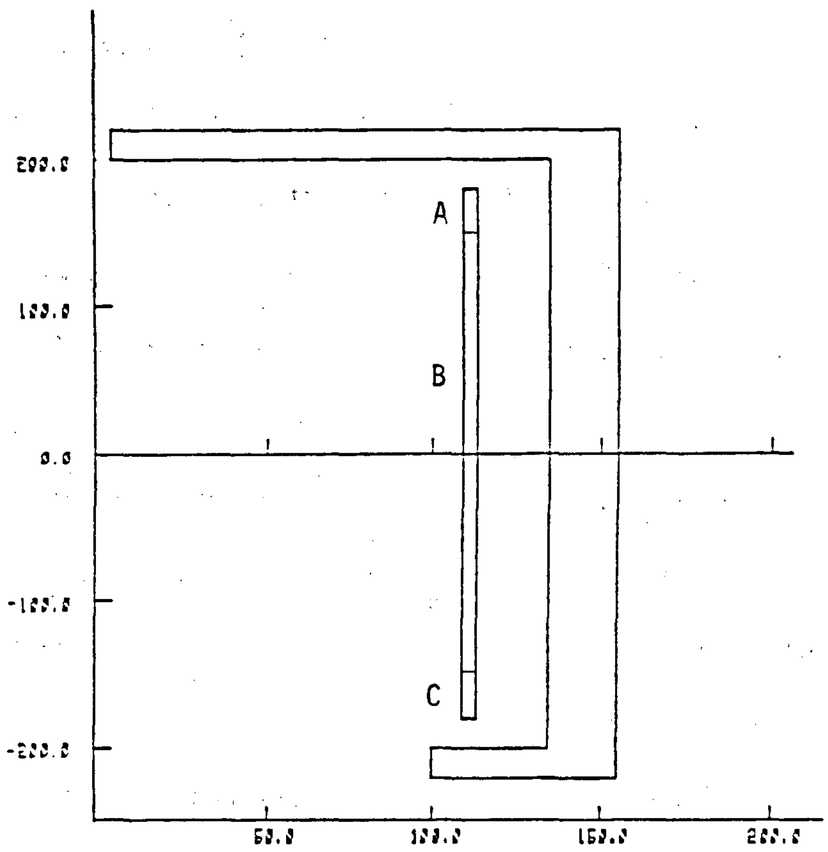

Fig. 4.14. The preliminary magnet design provided by Oxford Instruments, Ltd. has three independent superconducting coils, indicated by A, B, and C.

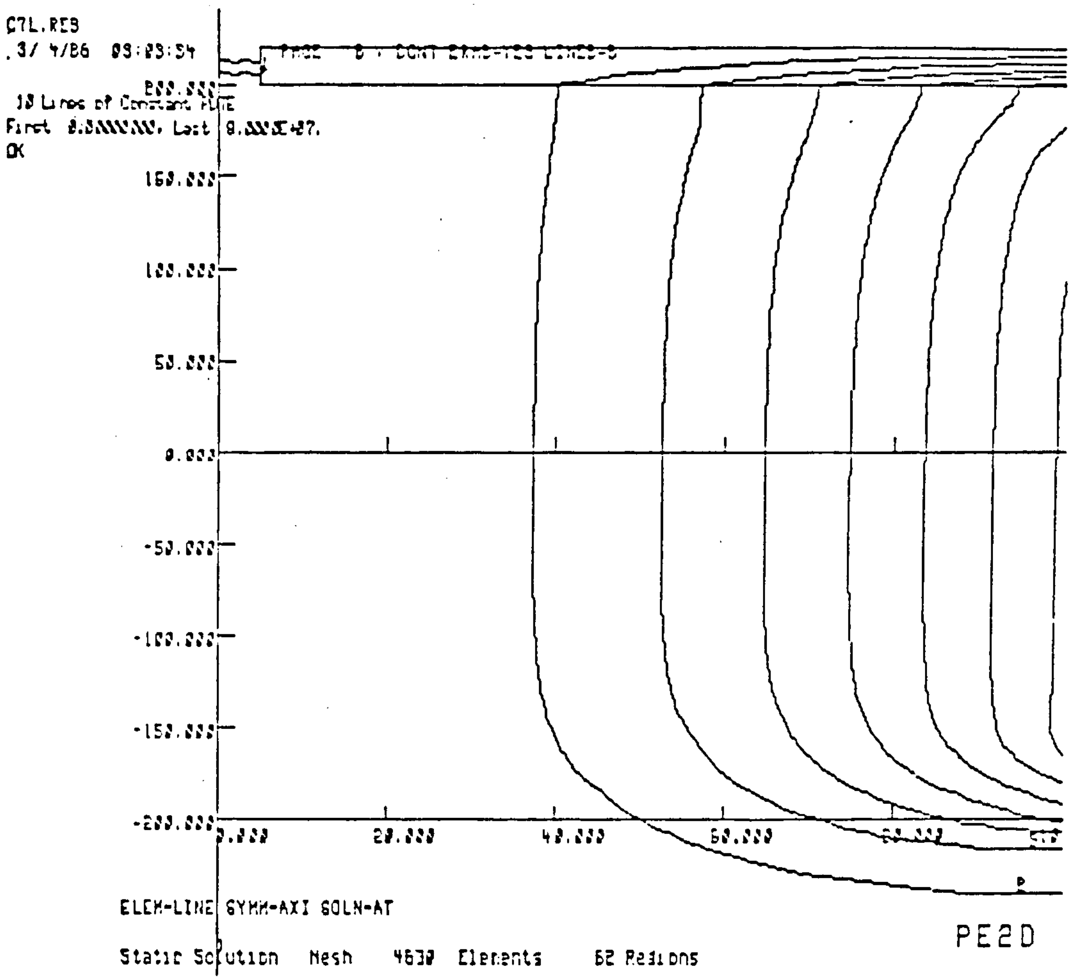

Fig. 4.15. Field map from the preliminary magnet design of Oxford Instruments, Ltd. The abscissa is the radial coordinate, and the ordinate is the z-direction.

the data-taking runs to verify that the magnetic field has remained constant and to calibrate the effect of electric field non-uniformities, which are less well understood and which may vary. The technique of laser calibration has been demonstrated by the ALEPH collaboration [Am 85a], using their TPC 90 prototype.

Chapter 5

5. The TPC: Specific Design Considerations

5.1. Two Track Separation

The TPC has been introduced in Chapter 1 and its potential performance discussed in detail in Chapter 4. In this chapter we present specific design considerations, concentrating on those areas where our application of the TPC technique is more difficult than previous ones. The most important difference from previous TPC experiments is the high multiplicity of particles emitted in relativistic heavy-ion collisions. This requires special attention to two-track separation. The high event rates, coupled with the high multiplicity of secondary particles, require special attention to space-charge effects. Finally the wide range of particles and momenta of interest in heavy ion collisions requires special attention to the dynamic range of the electronics.*

We analyze the response of the TPC in terms of pixels which are rectangular parallelepipeds with sides Δr , Δz , and $\Delta\xi = r\,\Delta\phi$, in a cylindrical coordinate system. Each pixel has a uniform response to any electrons produced inside it, and no response to any others. The transverse diffusion of electrons (given in Table 4.1) is negligible compared with the pad size. We therefore set Δr and $\Delta\xi$

---

*Other areas where new ground needs to be broken are discussed in Sections 3.4 and 6.5 (particle identification) and Chapter 8 (handling the enormous volume of data).

equal to the pad dimensions in the radial and azimuthal directions. This is an approximation to the true response: the PEP-4 collaboration [Ai 83] found that the pad response function is a gaussian with FWHM roughly equal to the pad width in each direction. The longitudinal response is, on the other hand, completely determined by diffusion, the time sampling rate being chosen to ensure that this is so. We set $\Delta z = 2.24\sqrt{(z+50)/200}$ cm, the FWHM of the distribution, where z is measured in cm, and the target is located at $z = 0$.

We can now visualize the response of the detector, considered filled throughout its volume by pixels as defined above, and ask for each pixel whether one track passes through it, or more than one. To simplify the analysis we assume all the tracks are straight ($B = 0$). By making this approximation, we can calculate the probability that a given pixel will be hit, in terms of the solid angle subtended by that pixel at the target.

The straight-line approximation is instructive since it emphasizes the strong geometrical correlations within specific events, i.e., if two tracks are not resolved at large radii they will not be resolved at any smaller radii. This is the key consideration at small angles, where the problem of two-track separation is most severe. At the other extreme, it is not at all valid for low-momentum particles produced at large angles, which may spiral through the detector introducing a great deal of unwanted information about themselves while obscuring other tracks where they cross. However, only a small fraction (~20% — see Fig. 4.1(a)) of particles spiral. Monte Carlo calculations using GEANT3 confirmed that the separation of nearly parallel tracks is the most significant problem in two-track separation, and indicated the desirability of an analytical approach such as the present one.

Figure 5.1 shows the summed particle yields for central Au+Au and Ar+KCl collisions based on the model events described in Chapter 3. The greatest particle density is at 0°, where for Au+Au 270 particles are emitted per steradian. For the TPC, the solid angle subtended at the target by pixels near 0° is given simply by $\Delta\Omega = (\Delta r)(\Delta\xi)/R^2$ where R is the distance from the target. We can now calculate the mean number of particles, m, hitting a given pixel. This is a useful figure-of-merit for two-track separation. The Poisson distribution with mean m gives the probability that one, and only one, particle will be observed in a pixel as $P(1) = me^{-m}$. The probability that a given particle will be clearly measured is therefore $P(1)/m$, or e^{-m}. The multiple-hit probability, which we shall refer to as MHP, is $1 - e^{-m} \approx m$ for small values of m. For comparison with existing detectors, we note that the basic elements of the Plastic Ball [Bad 82] are 4.2 msr for $10° < \theta < 30°$ and 17.5 msr for $30° < \theta < 160°$. According to our calculation for Au+Au central collisions at 1 GeV/A, $m \sim 1.0$ for the Plastic Ball elements at 10°. This gives a MHP of 63%: only 37% of the particles can be measured cleanly. This calculation neglects dynamical correlations, which might increase the MHP by as much as a factor of two (see [Za 84] and the discussions of momentum flow in [AA 86]).

We begin by considering two-track separation at the outside of the detector. It is essential to achieve clear separation of the tracks at large radii, to simplify pattern recognition: once we know what tracks are present we will find it easier

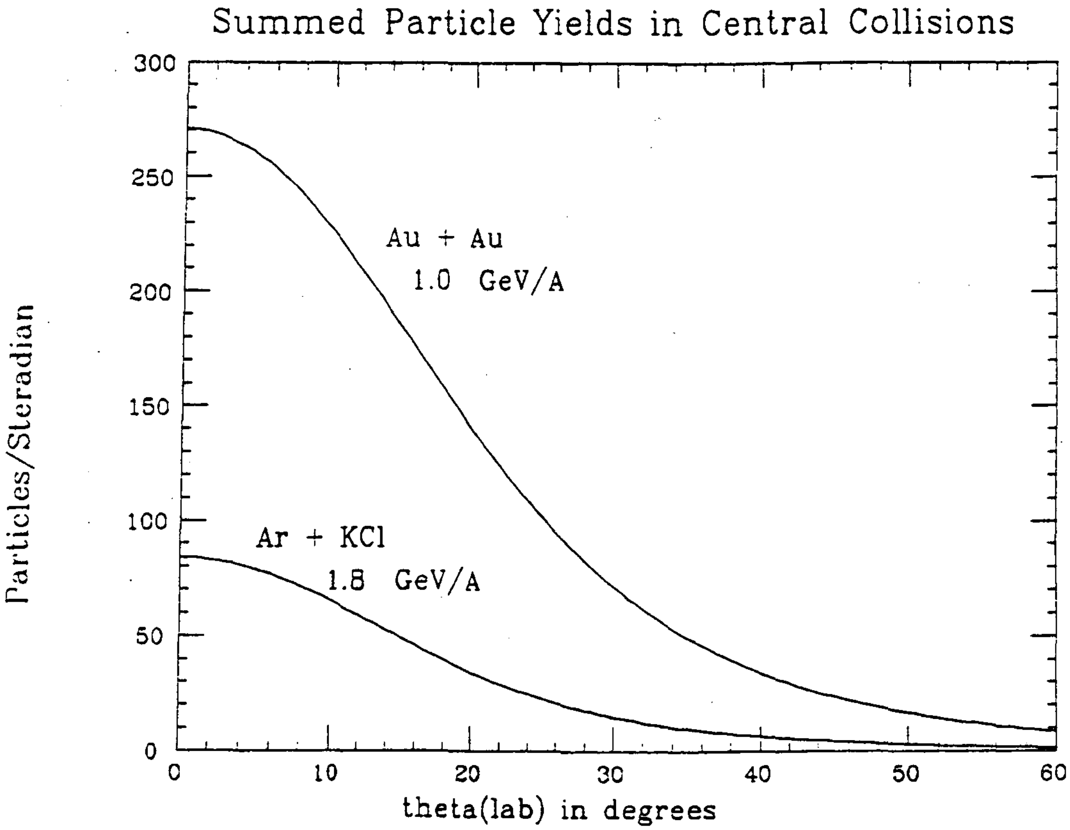

Fig. 5.1. Summed particle yields for central Au+Au (1 GeV/A) and Ar+KCl (1.8 GeV/A) collisions as a function of θ.

to extend their analysis to the smallest radii where useful information can be obtained. In addition, most of the momentum information is in the outer part of the track (assuming that the vertex location is known) since the magnetic deflection is proportional to the square of the distance.

We have considered three different pad and wire configurations:

(a) $(0.5cm)^2$ pads everywhere ;

(b) $(1.0cm)^2$ pads everywhere ;

(c) $(0.5cm)^2$ pads at r = 10 cm, varying linearly to $(1.5cm)^2$ pads at r = 90 cm.

In each case the wire spacing is one half of the pad width.

5.1.1. Multiple Hit Probability for the Pads

The radial pad width Δr contributes $\cos\theta \cdot \Delta r / R$ to $\Delta\theta$. The longitudinal diffusion contributes $\sin\theta \cdot \Delta z / R$. The FWHM of $\Delta\theta$ is given by the greater of the two contributions (in our uniform-response model of the pixels). At angles less than θ_c the two-track separation in θ is determined by Δr and at greater angles by Δz. The angle $\theta = 31\,^\circ$ corresponds to the circumference of the front face of the TPC. The pixel width in the ϕ direction is $\Delta\phi = \Delta\xi/(R\ \cos\theta)$, transverse diffusion being negligible.

Before calculating the MHP, we need to make an important modification to our schematic model, to allow for the fact that the true response function in each direction (r, ξ, z) is given by a gaussian, rather than by the square distribution of the same fwhm which we have assumed. Figure 5.2 shows calculated pad responses for a gaussian distribution with $\sigma = w/2.35$, where w is the pad width, for various separations of two tracks and for various locations of the hits relative to the pad centers. It will be seen that a separation of 2.5 w is the smallest which reliably gives a pad with near-zero response between the two tracks. We consider this to be an essential condition for simple and rapid pattern recognition, and therefore increase the effective pixel width by a factor of 5 for calculating the MHP. This yields a factor of 25 in $\Delta\Omega$, allowing for a factor of 5 in both Δr (or Δz), and $\Delta\xi$.

Figures 5.3 show the MHP as a function of θ for Au+Au central collisions at 1 GeV/A and for Ar+KCl central central collisions at 1.8 GeV/A based on the model events described in Chapter 3, and calculated for the outside of the detector, i.e., for pixels at the maximum radius. In comparing the results for the three cases, it should be borne in mind that case (a) requires about 100,000 pads, while cases (b) and (c) each require about 25,000. Since it is hardly likely that the electronics can cost less than about $100 per pad, the number of pads is likely to be limited by economic considerations. Case (c) gives the same MHP as case (a) at the smallest angles, and about the same as case (b) at larger angles. Section 5.2 will discuss the feasibility of constructing an end-cap with a non-uniform pad and wire arrangement, such as case (c).

The multihit probability shown in Fig. 5.3 is about a factor of 10 better than for the Plastic Ball [Bad 82], and comparable to that achieved in the new 4π detector proposed [No 86] for the SIS/ESR facility under construction at GSI.

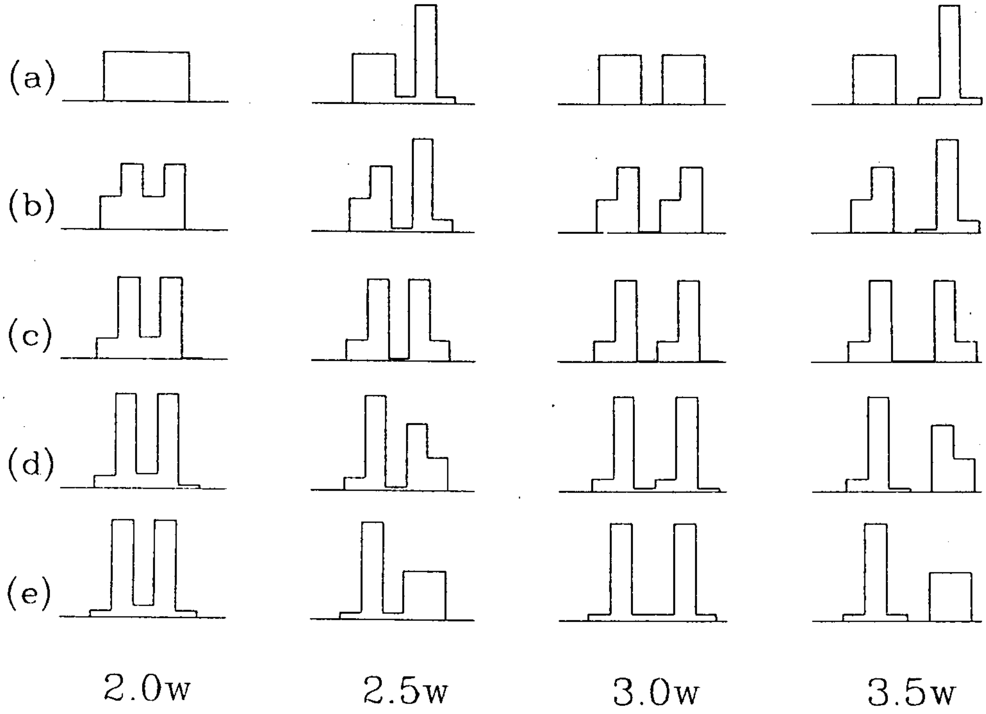

Fig. 5.2. Calculated pad responses (Gaussian distributions), for various locations (a-e) of the ionization centroid relative to the pad centers.

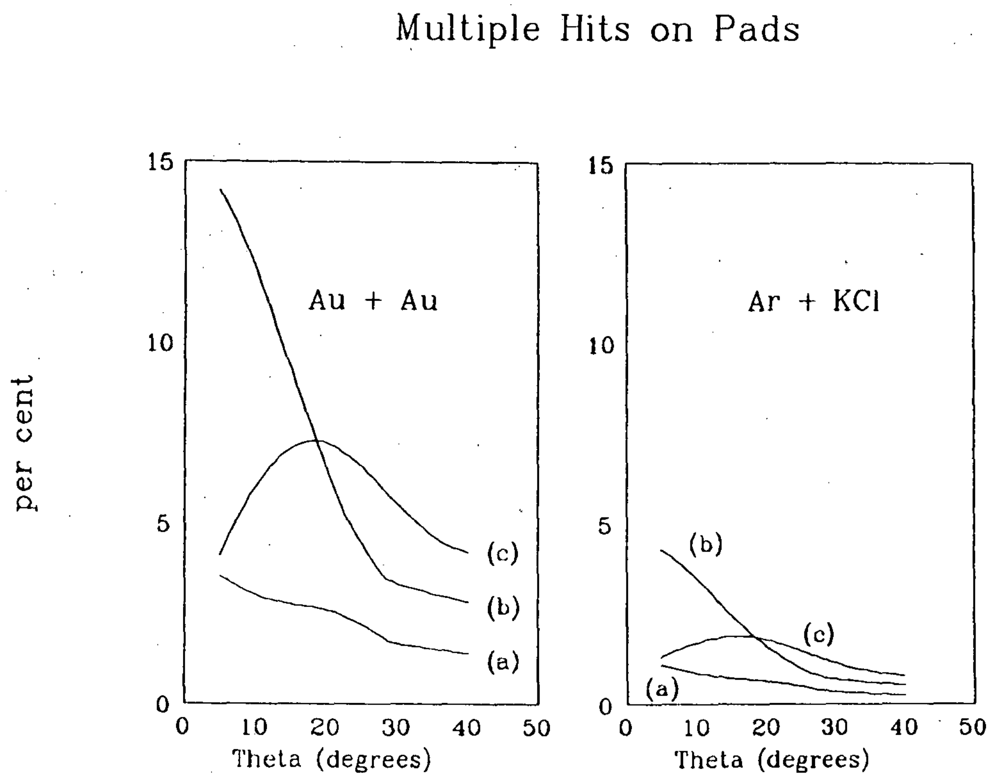

Fig. 5.3. Multiple hits on the pads for Au+Au at 1 GeV/A and Ar+KCl at 1.8 GeV/A. The three pad layout designs (a-c) are described in the text.

In the interior of the TPC, the two track separation deteriorates in a complicated way. For cases (a) and (b) the MHP at small angles (where it is determined by Δr and $\Delta\xi$) increases proportionately to $1/R^2$. At larger angles (where it is determined by Δr and Δz it increases proportionately to $1/R$. Case (c) shows a slower dependence on R, since the pad size varies linearly with R. Overall we can say that the MHP is increased by a factor of two to four at $R/2$. This means that simple track recognition will not be possible in many instances, and χ^2 minimization routines will be necessary. We note that two tracks separated by 1.25 w (half the separation assumed for the curves in Fig. 5.3) satisfy the Rayleigh criterion of 3σ separation. thus χ^2 minimization should reduce the MHP shown in Fig. 5.3 by about a factor of 4. Since this is about equal to the increase in MHP on going to $R/2$ we consider that Fig. 5.3 also represents the two track separation at $R/2$, provided least squares minimization is employed.

Finally we note that the performance of any of the three pad layouts is satisfactory for Ar+KCl central collisions.

5.1.2. MHP for the Wires

The procedure for calculating the MHP for the wires is similar to that for the pads. The value of Δr for the wires is twice smaller than for the pads. Since the values of θ_c are reduced by about a factor of two, so that the value of $\Delta\theta$ is nearly always determined by longitudinal diffusion.

To calculate the MHP for the wires, we used $\Delta\phi = \pi/3$ corresponding to a six-sectored end cap and increased the effective $\Delta\theta$ by a factor of 5, following the same arguments in Section 5.1.1. The results are shown in Fig. 5.4. They are rather discouraging, though we note that a factor of four reduction may be achievable with least-squares fitting.

In order to improve the MHP for the wires it would be necessary to increase the number of wires. Decreasing the radial spacing does not help. Any improvement would have to come in the azimuthal direction, through additional segmentation of the end cap, such as by introducing more sectors, or using a hexagonal array as for the ALEPH detector. The number of wires needed for cases (a), (b), and (c) are 1920, 960, and 960 respectively. Increasing that number to about 10,000 would bring the MHP for the wires down to values comparable to those for the pads. However, the dead regions of the TPC at the ends of the wires, would be greatly increased. Any other solution would involve a radical revision of the concept of the EOS detector.

5.2. Pad and Wire Layout

The EOS time projection chamber, in contrast to similar devices built for colliding beam experiments, is single ended. This enables us to minimize nuclear and electromagnetic interactions by placing the electronics upstream from the target, where there are only a few particles. The side walls and anode plane can be thin, low-density material, while the endcap can be constructed to have high rigidity and maintain the close tolerances required. The beam pipe, which is evacuated, is made of beryllium, or of carbon fibers. We adopt a sectored layout as in PEP-4 and DELPHI. This has the disadvantage of radial dead regions. If we

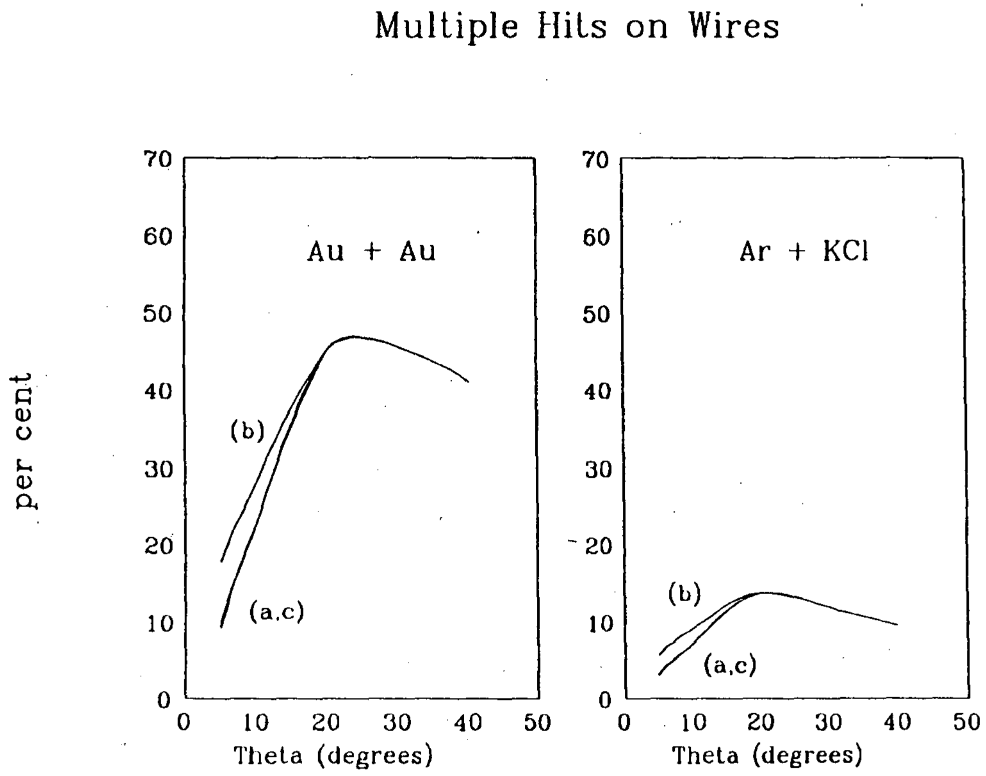

Fig. 5.4. Multiple hits for the wires, for the three endcap designs described in the text.

can contrive to reduce these to 1 cm, a six-sectored layout would be 8.3% dead near the center and 1.1% at 90 cm radius. The loss would be greatest for stiff particles at very small angles.

A major difference between the EOS TPC and the colliding beam detectors is that in order to achieve adequate two-track separation we have to rely on the information obtained from the pads. To obtain sufficient dE/dx measurements it is then necessary to cover the entire end cap with pads. A logical consequence of this approach might be to abandon the wire information altogether, the wires serving only to generate avalanches when the drifting electrons reach the end cap. Another approach might be to use a mesh anode instead of a grid of wires. This is very attractive [Hi 83] but suffers from the disadvantage that a field of about 15 kV/cm is required, compared with 1 kV/cm for a grid. The system is very close to breakdown and may also have intrinsic instabilities in a magnetic field [Gr 86a]. Another possibility would be to use short anode wires, as in the NA36 design [Gr 86b]. This has great advantages for two-track separation, but is not useful for dE/dx measurements because of gain variations along the anode wires due to edge effects.

The arguments in favor of retaining the wire information are several, in addition to the argument that the number of electronics channels required to read out the wires is only a few per cent of the total†. First, there is a class of important low multiplicity experiments, such as Λ^0 and K production in p-p and p-nucleus collisions, that are necessary to understand the more complex nucleus-

---

†The wires, nevertheless, add significantly to the burden on the data handling system.

nucleus collisions but will not produce too high a multi-hit probability for the wires. Second, if the size of the avalanche on a wire is known, analysis of the nearby pads' responses to it is greatly simplified. Third, because the wires are more closely spaced than the pads (by a factor of two) the dE/dx information obtained from them is improved by a factor of $2^{-0.14}$ or 0.91 in resolution.[‡] Fourth, use of the wire information permits some corrections for dE/dx fluctuations to be made in position measurements and hence an improvement in the momentum resolution. These uses of the wire information will not be possible for all tracks, especially for the parts of tracks that are near the target, but will be a most valuable supplementary source of information.

The distance from the pads to the anode wires is usually set at about half the pad width. A disadvantage of a small value of this distance is that most of the induced signal may be on a single pad, with insufficient signal on adjacent pads to permit accurate fitting of a centroid. Figure 5.5 shows this effect for gaussians of FWHM equal to various multiples of the pad width. The situation in 5.5(a) corresponds roughly to the PEP-4 response, while 5.5(b) corresponds roughly to the response of ALEPH and DELPHI, where the pad width has been reduced by about a fact of 1.2 for the same wire-cathode distance. Figure 5.6 shows the layout of wires in PEP-4. The appropriate layout for the EOS TPC has not yet been studied in depth, except for considerations of space-charge build-up due to positive ion feedback. To reduce this effect we plan to add an additional grid and have carried out calculations for typical arrangements (such

---

[‡] In addition to this, the dE/dx samples obtained from the wires are truly independent while the pad information is a weighted average over several such samples.

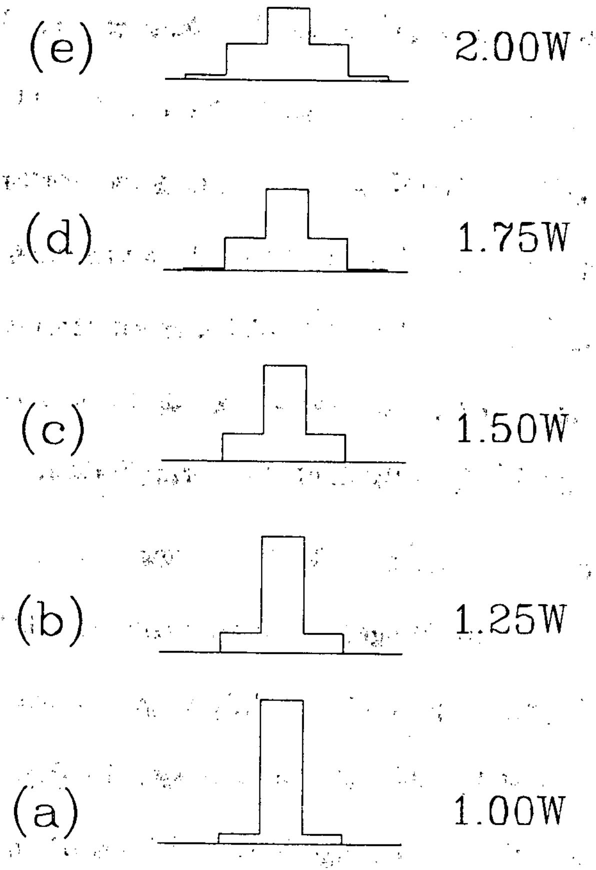

Fig. 5.5. Pad responses for different anode to pad distances, as a function of the pad width, w.

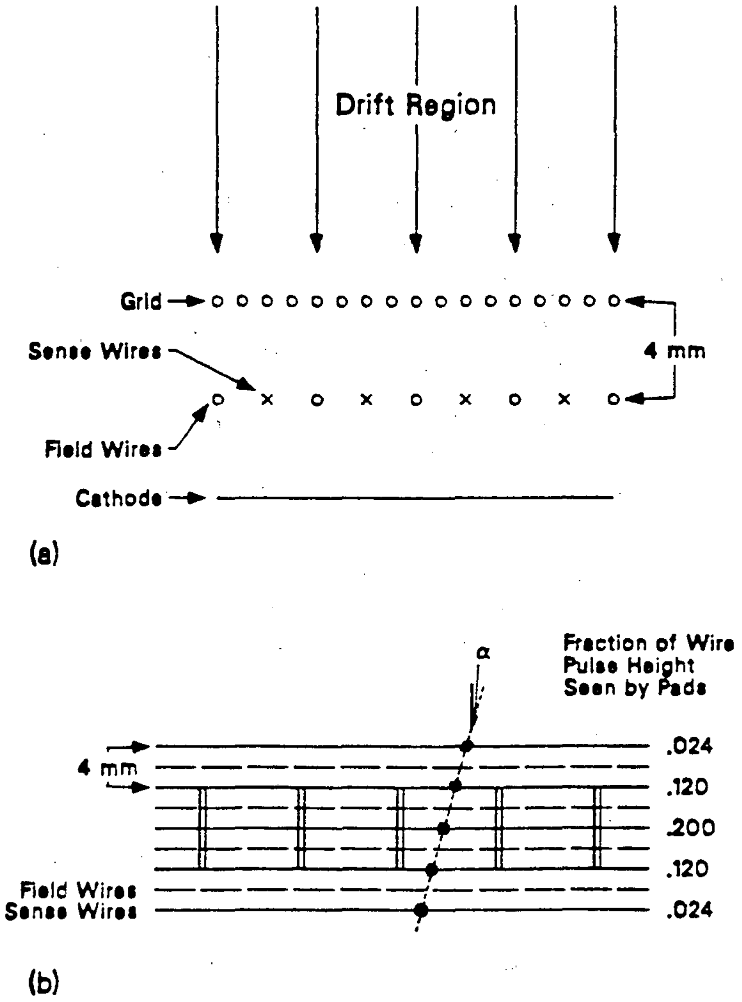

Fig. 5.6. The wire layout for the PEP-4 TPC [Cl 76].

as ALEPH) to check that a suitable suppression is possible (see Section 5.4).

We have so far described the pads as arranged in concentric rows, but no firm decision has been made on this as opposed to having straight rows parallel to the wires, as in the PEP-4 detector. The ALEPH and DELPHI detectors have opted for a concentric arrangement, which ensures that the crossing angle for their stiff tracks is close to 90° and consequently reduces the off-line corrections to be applied in the momentum analysis. This argument applies also to the EOS TPC, but to a lesser extent and not at all to spiraling particles. An argument supporting concentric rows is related to pattern recognition. Pattern recognition is simplified if the events are projected into the r-z plane. In such a projection, most of the tracks are nearly straight, and this view is easier to construct (perhaps on-line to insert in a trigger) if all the pads at a given radius are oriented identically. The argument in favor of straight rows lies in the geometrical simplicity and ease in combining wire and pad information.

5.3. Non-Uniform Pad Arrangement

In Section 5.1, considerations of the most economical approach to the multi-hit situation led us to propose a pad layout in which the size of the pads varies linearly from the inner to the outer radius of the TPC. We discuss two possible situations: variable gap and anode wire distance, and readout through resistive cathodes. The latter was suggested to us by F. Sauli [Sa 86]. Another possibility which we have considered is to use some variation of the TRIUMF TPC geometry [Bry 84], consisting of individual proportional tubes. We have not included the latter here since we have been unable, so far, to conceive a design which provides both good dE/dx and good position measurement.

(a) Variable Gap and Anode Wire Distance

A possible layout is to vary the pad size, wire spacing and anode-cathode gap in the same proportion, to maintain optimum localization properties. It is not mechanically feasible to vary the wire diameter in the same proportion, and it would be inconvenient to vary the wire potential. We therefore examine the effect on the proportional multiplication of keeping the wire diameter and potential constant. With reference to Fig. 5.7(a), let us imagine a MWPC in which both the gap width g and the wire spacing s are a function of the coordinate perpendicular to the anode wires; the diameter of the wires is constant and equal to 2a, and the operating voltage is V_0. In first approximation, and for moderate gains, one can express the proportional multiplication factor [Sa 77] as follows:

$$M \approx \exp(kCV_0) \tag{5.1}$$

where C is the capacitance per unit length of the anode wire to the cathodes, and V_0 is the operational voltage. K is a constant for a given gas and wire diameter. The capacitance per unit length C is given for $g \sim s >> a$ by:

$$C = \frac{2\pi\epsilon_0}{\frac{\pi g}{s} - \ln(\frac{2\pi a}{s})} \tag{5.2}$$

assuming that the local variations of parameters, in a geometry such as the one of Fig. 5.7(a), can be neglected. Again in first approximation, for $s >> a$, Eq. 5.2 can be written as:

$$C \approx \frac{2\epsilon_o \; s}{g} \tag{5.3}$$

Combining Eq. 5.1 and 5.3 one can see that the gain M remains constant, for equal wire radii and operating voltage, if the ratio s/g is kept constant. Although a more detailed analysis may show a deviation from this simple relationship, a solution in which both the gap and wire spacing are increased seems rather straight forward to implement.

(b) Readout through Resistive Cathodes

A simple way of adjusting the pad width and distance without modifying the basic MWPC construction and operation is to read out the induced pulses through a semi-transparent or resistive cathode. This method of read out was developed originally to allow a flexible choice of the geometrical shape of the readout electrodes and to simplify the construction of large, modular systems such as those based on plastic streamer tubes [Ba 78], [Bat 82]. It is based on the observation that, if one cathode in a MWPC is made from a thin sheet of material having a large surface or bulk resistivity, the fast signal induced on external pickup electrodes has roughly the same amplitude and distribution of that induced on identical electrodes internal to the chamber. A detailed analysis of the induced signal formation through resistive electrodes appears in the quoted

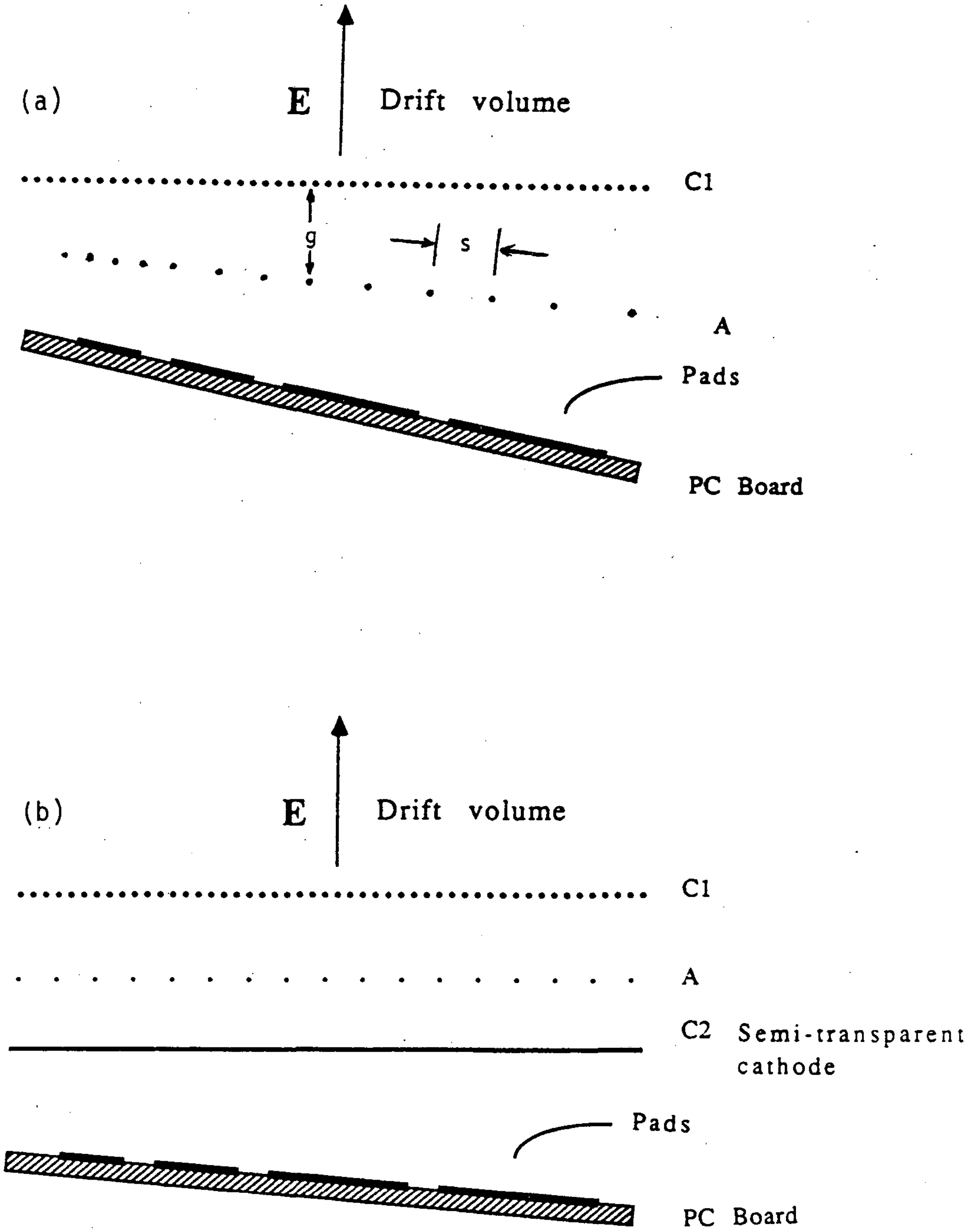

Fig. 5.7. Two possible ways to vary pad size and gap spacing as a function of radius [Sa 86].

references: in particular, the transparency of the cathode to induced signals increases with its surface resistivity and can approach 100%. The width of the induced charge distribution on external electrodes has been measured for a large range of geometrical parameters, although always for pickup electrodes lying in close contact with the backside of the resistive cathodes, and satisfies the general rule of having a FWHM equal to twice the anode-pickup electrode distance. It seems reasonable to assume that the dominant effect is purely geometrical, irrespective of the cathode-anode distance in the MWPC. In the geometry illustrated in Fig. 5.7(b) a standard end cap thin-gap MPWC is shown with one cathode consisting of a high resistivity foil; signals are read out using suitable pads, external to the chamber, and having a size comparable to their distance from the anode plane. As in the conventional TPC geometry, the readout pads can be organised in rows parallel to the anode wires or, for example, in circular arcs such that stiff tracks would be nearly perpendicular to the pad rows.

An obvious advantage of the semi-transparent cathode solution is that it allows one to change rather easily the readout pattern without disassembling the whole detector; this may be particularly convenient if, as a consequence of a change in energy or nature of the interactions under analysis, the topology of the detected tracks is modified.

5.4. Space Charge

That space charge build-up is potentially a serious problem is illustrated by the following naive calculation:

Assume 200 tracks per event and an average track length of 1 m. This yields $2 \cdot 10^4$ cm of track per event. If there are 40 ion pairs per cm (minimizing ionizing) there will be $8 \cdot 10^5$ primary electrons. Assume a detector collection efficiency of 100% and a gas multiplication of 10^4 at the anode. The total positive ion production at the endcap is then $8 \cdot 10^9$ positive ions per event. The drift velocity of the positive ions is about 0.16 cm/μs so that they take 1.25 *s* to drift across the 2 m TPC. During this time there will be $1.25 \cdot 10^4$ events at a collision rate of 10^4 per second. This leads to a steady state situation with 10^{14} positive ions in the chamber, or $1.6 \cdot 10^{-5}$ coulomb. If we assume that this charge is uniformly distributed throughout the volume of the TPC, we can apply Gauss's law to find that there will be an enormous radial field, $E_r \simeq 10^5$r Volts/m (where r is the radius in m), compared to the 10^4 Volts/m longitudinal field applied to drift electrons.

In order to carry out a proper calculation, we have taken into account the effect of mirror charges in the walls of the detector, the effect of the Frisch grid introduced to reduce the amount of positive ion feedback, and the effect of a gating grid introduced to prevent drift electrons from unwanted events from reaching the sense wires.

The grid system is shown in Fig. 5.8, which depicts the electric field lines with the gating grid open (a) and closed (b) [Am 85b]. Consider first the situation with the gating grid open. Since all the field lines in the drift region pass through the gating grid, it is totally transparent to drift electrons. The same is

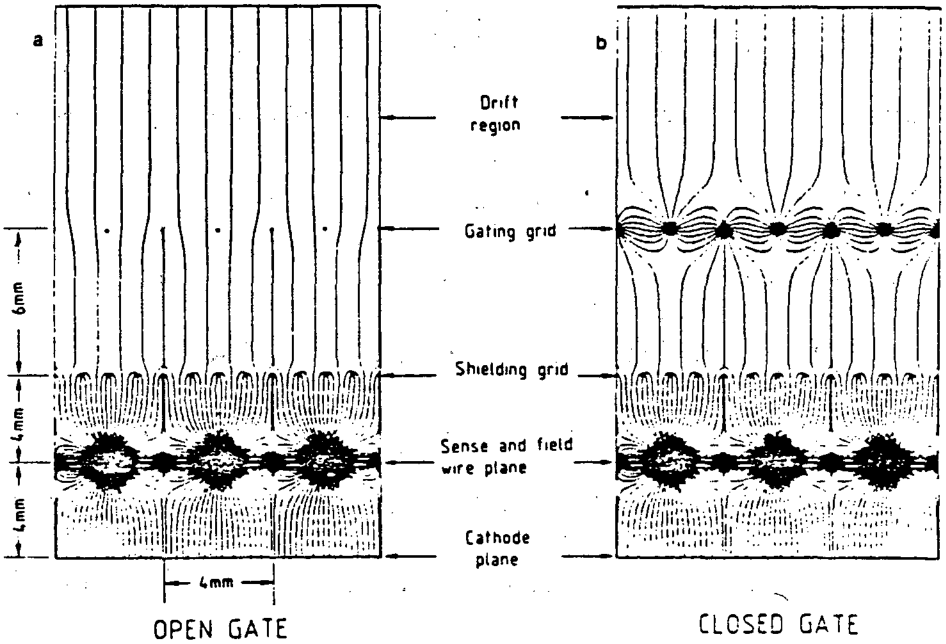

Fig. 5.8. Grid configuration and field map for (a) gating grid open and (b) gating grid closed [Am 86].

true of the shielding (Frisch) grid. However, the returning positive ions, produced in the avalanches at the sense wires, are mostly captured on the shielding grid. The transparency of the combination of shielding grid and open gating grid is given by the ratio of the field strengths in the drift region and in the region inside the shielding grid, and is typically 0.07.

The gating grid is normally closed, with the voltage raised and lowered on alternating wires, as shown in Fig. 5.8(b). In this condition it is completely opaque to both electrons and positive ions. This has been verified at the level of 10^{-3} [Am 85b]. The gating grid is opened after a desired event occurs, and held open for the 40 μs drift time of the TPC. the combined effect of the two grids is that events occurring when the gating grid is closed produce only the positive ions generated in the primary tracks. Events occurring when the gating grid is open produce positive ions at the sense wires at about 10^4 times the number of drift electrons. Of these only about 7% reach the drift volume. The average number of positive ions in the drift volume (assuming a steady beam) is therefore given by:

$$1.25\, N_0\ R\ \left(1 + 0.07\, AN/R\right) \tag{5.4}$$

Here N_0 is the average number of positive ions produced in the primary tracks, per event; the factor 1.25 is the number of seconds required for a positive ion to drift through the TPC; R is the number of events per second; A is the gas multiplication; and N is the number of triggers per second.

We now consider an event rate $R = 10^4$/s. It is unlikely that higher rates would normally be used, since even for $R = 10^3$/s there would be a probability of 8% that one or more additional events would occur during the 40 μs preceding or following the trigger, producing extra tracks in the event which is read out. For a trigger rate of $N = 1$ per second (such that every read out event could be stored on tape) the additional positive ions returning from the sense wires are negligible (7%). For a trigger rate of $N = 100$/s, assuming a factor of 100 for preselection of events before data storage or for additional data compression, the overall number of positive ions in the chamber would still be only 8 times greater than the primary ionization, the effect of which will be calculated below.

The number of positive ions assumed in our "naive" calculation is fairly realistic for Au+Au. While the average event will have only about 50 tracks rather than the 200 used in the estimate, many of the tracks will be several times minimum ionizing. Space-charge build-up for Ar+KCl will be reduced by a factor of 5 compared with Au+Au. We have not considered the "clumpiness" of the positive ion distribution generated at the sense wires, in which each event for which the gating grid was opened generates a plane of positive ions about 6 cm thick which drifts backwards through the chamber at 0.16 cm/μs. The "shadow" tracks in this plane could produce perturbations of subsequent events at particular values of z which would be known from the times of previous triggers.

We have calculated the effect of the primary ionization 1.25 $N_0 R$ in Eq. 5.4 by solving Poisson's equation in the volume of the detector, following the procedure of G.J. Van Dalen [Va 81]. For an event rate $R = 10^4/s$ and $N = 0$ we obtain the distribution of potential lines shown in Fig. 5.9. The effect of a radial electric field was presented in Eq. 4.11, in terms of the integral $\int_z^{-1} E_r \, dz$, which is at most 2 volts. Since E_z is about 100 V/cm, the maximum radial displacement is therefore 0.004 mm, which is negligible, largely as a result of the reduction by a factor of 50 produced by the magnetic field. Longitudinal displacement is more important, reaching a maximum of 0.2 mm, but this is still small compared with the longitudinal accuracy of the chamber, which is of the order of $\sigma = 1$ mm for a single measurement (see Table 4.1).

The use of a gating grid means that a small part of the chamber is not useful: if it takes 2 μs to open the grid (e.g., 1 μs to make an electronic decision and 1 μs to open it) 10 cm of track at the back of the chamber would be lost, since the drift velocity is about 5 cm/μs.

5.5. Dynamic Range of the MWPC

The dynamic range required in TPC's for collider physics is relatively small: for example, the ALEPH TPC is designed to accept signals up to only five times minimum ionizing. In this section we discuss the response of the MWPC's to the heavily-ionizing particles to be encountered in the EOS TPC. In Section 5.6 we discuss the dynamic range of the readout electronics.

In order to obtain sufficiently large signals from minimum-ionizing particles it is necessary to operate the MWPC's at high gas multiplication, of the order of 10^4. This is required for accurate position measurements, as we shall now show

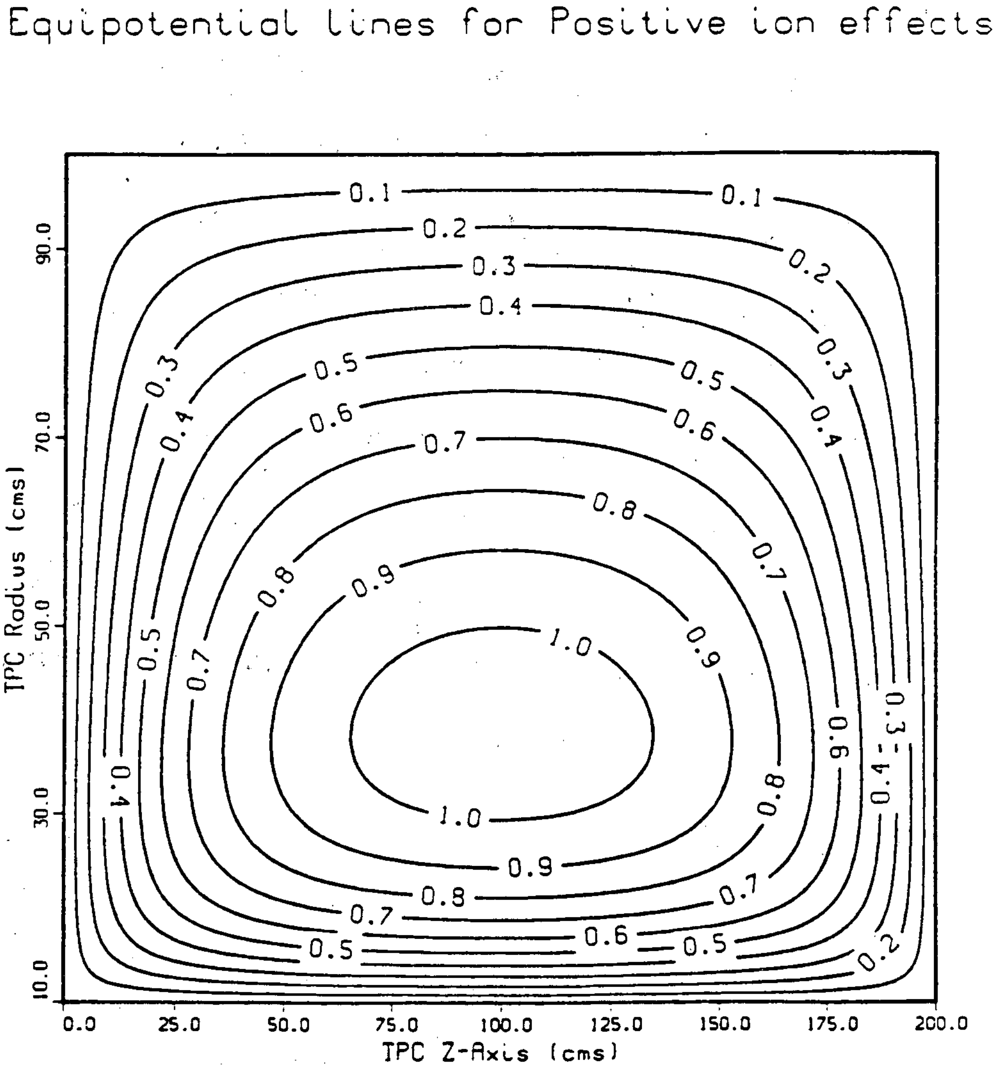

Fig. 5.9. Equipotential lines (1 contour interval corresponds to 0.2 volts) due to the presence of positive ions in the TPC volume. The calculation is for an event rate of 10^4/sec, shows only the primary ionization. The total ionization can be obtained using Eq. 5.4.

(this analysis is similar to one presented for the ALEPH TPC).

Consider a minimum-ionizing particle that produces 40 electrons/cm, crossing a pad row of width 1 cm. Anticipating our needs, the gas multiplication be 10^4, so that 400,000 electrons are produced on the wires. One half of this signal is induced on the cathode, about 60% of that is on the central pad, and about 50% of the charge is collected within the integration time of the preamplifier. The net signal for 1 cm of track is 60,000 electrons. Since the rms noise on the preamplifier is likely to be about 600 electrons equivalent, the signal-noise ratio is about 100. We have calculated that this signal-noise ratio yields a position accuracy of between 30 and 100 μ, depending on whether the track falls on the dividing line between two pads or on the center of one pad. The intrinsic spatial accuracy of the TPC is between 100–200 μ depending on location of the track in the chamber. Thus, if the spatial accuracy is not to be limited by noise, a gas multiplication of about 10^4 is needed.

We now investigate the performance of proportional counters at gas multiplications up to 10^4 or so. In doing so we have found review articles by West [We 53] and Sauli [Sa 84] particularly useful. Hanna, Kirkwood, and Pontecorvo [Ha 49] have investigated the limits of gas multiplication in a 77% Au 23% CH_4 mixture at atmospheric pressure. By companying the signals obtained from electrons of 2.8 keV, 17.4 keV, and 250 keV they found that the limiting factor in determining the linearity of response was not the value of the gas multiplication, but the total number of electrons in the avalanche. For their detector (100 μ

wire diameter, 2.5 cm cathode diameter) the response was "linear within experimental accuracy of 2% up to a critical value of gas multiplication M_c above which the width suddenly increased and lack of linearity was apparent." They found that $EM_c \simeq 100$ MeV, where E is the energy deposited in the detector by the primary radiation, but that "the condition is certainly less stringent when the original ionization is spread over a large distance." Benjamin, Kemshall and Redfern [Be 68] found that for a 90% Au 10% CH_4 mixture at atmospheric pressure the same result held for 60-keV γ rays and 585 keV protons, with $EM_c \simeq 93 \pm 3$ MeV. Their wire diameter was 60 μ.

Hanna [Ha 50] using roughly collimated alpha particles, noticed that "below the region of saturation, a symmetrical distribution of pulses was obtained. As saturation set in, the pulse distribution broadened at first and then, at higher voltages on the counter, the distribution became asymmetrical with a pronounced tail on the high energy side. This behavior could be explained in terms of a variation of multiplication factor with track orientation. Those tracks with a large projection in the direction of the wire are least affected by saturation and so give rise to the high energy tail."

More recently, Mori, Uno and Watanabe [Mo 82a] studied saturation effects for X-rays in a proportional counter filled with methane. They found that saturation is more serious at a given gas multiplication when the pressure is increased, or when the wire diameter is reduced, and proposed a microscopic description of the process. Mori and Watanabe [Mo 82b] also studied the response to alpha particles, at gas multiplications both below and above the critical value. they, like earlier workers, found that non-linearity becomes serious above about $EM_c \simeq 100$ MeV.

Figure 5.10 shows their results. The gas multiplication for alpha particles is given by:

$$M_\alpha = M \frac{M_\alpha}{M} \tag{5.5}$$

where M is the "true" gas multiplication obtained for very small energy losses, and M_α / M is the attenuation of the α signal. For M above about 100, M_α / M begins to deviate from unity, with the attenuation being more serious for α tracks at 0° (perpendicular to the wire) than at 40°. For $M = 10^4$, M_α / M is about 0.2 at 40° and about 0.05 at 0°. At $M \sim 3.10^4$ a sudden jump occurs and the angular effect reverses itself, with the 0° pulse height increasing a factor of 20 while the 40° pulse height remaines unchanged. By $M = 10^6$ the 0° and 40° signals are nearly equal again, with $M_\alpha / M \sim 3.10^{-3}$.

In the EOS TPC, rates of energy loss equal to those of low-energy alpha particles (about 2 MeV/cm) will be encountered. While the beam pipe stops alpha particles below 600 MeV/c, alphas with 700 MeV/c will still retain enough energy to cross the chamber. As they emerge from the beam pipe, such alphas are about 140 times minimum ionizing. At the end of its range the alpha is about 1500 times minimum ionizing. In addition, we can expect occasional particles of higher charge and therefore greater rate of ionization to be produced, either from the target or from secondary collisions in the TPC.

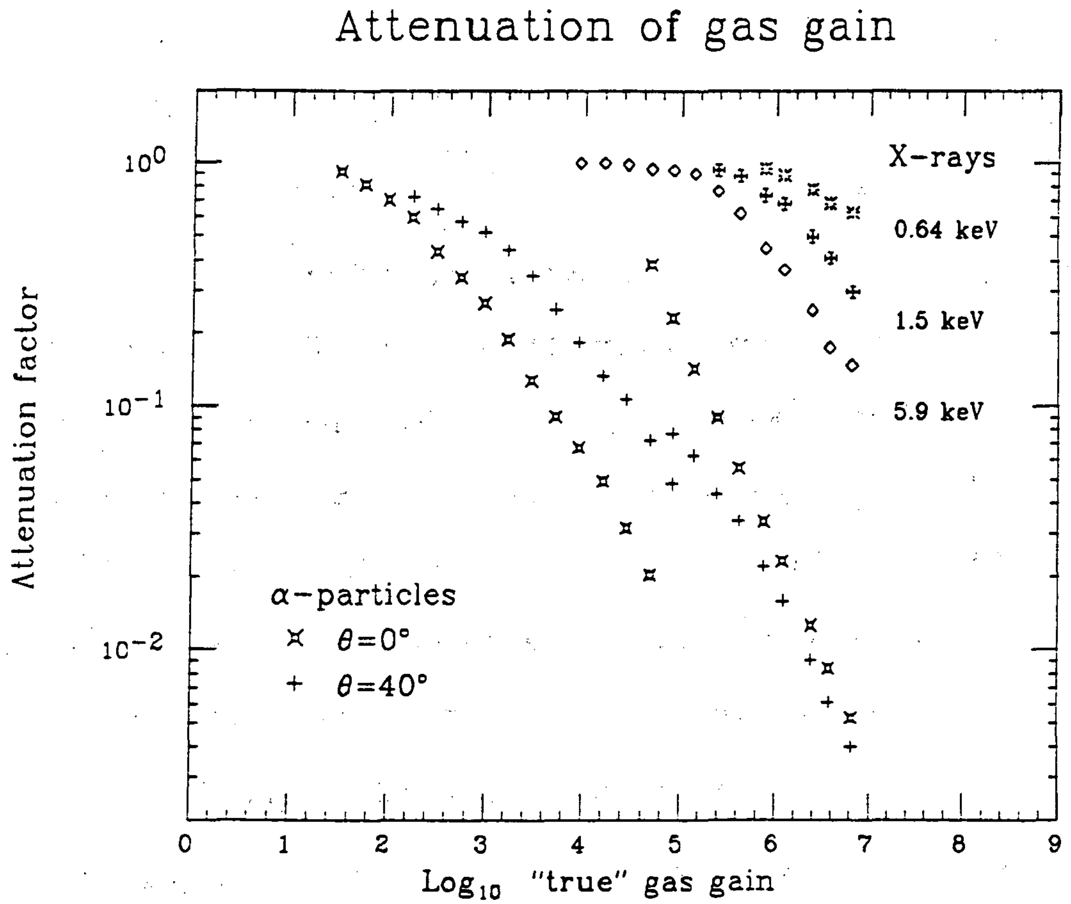

Fig. 5.10. Attenuation of gas gain for X-rays and α-particles, adapted from [Mo 82a].

The results of Mori and Watanabe [Mo 82b] show that we can reasonably consider operating at a gas multiplication $M = 10^4$. The breakdown phenomenon observed for tracks at 0° does not occur until $M \sim 3 \cdot 10^4$. Furthermore, they were still able to operate their counters at an equivalent gas multiplication M up to 10^7 or more. Nevertheless, the saturation effect is serious, about 0.1 at $M = 10^4$. Sauli [Sa 84] has suggested that since TPC's can measure the angle of a track it may be possible to make corrections to some extent for the angular dependence of the attenuation. The attenuation in itself is of no great consequence, and may indeed help by limiting the dynamic range needed in the electronics. However, associated effects may cause problems. Among these are the possibility of large fluctuations in dE/dx measurements, of damage to the wires as a result of heavy discharges or sparking, or of increased polymerization and deposits on the wires.

Further study of these questions is essential to determine better the phenomenology of MWPC response to heavily ionizing particles, for standard gases. Studies of Ar-CH_4 and Ar-C_2H_6 mixtures by Behrends and Melissinos [Be 81] have shown that the region of linearity can be extended by reducing the proportion of Ar in the gas mixture. They also found that CH_4 is more effective than C_2H_6 in reducing the saturation. These observations may indicate directions of study in order to understand and minimize any deleterious effects.

5.6. Dynamic Range of the Electronics

If we accept the saturation data of Mori and Watanabe [Mo 82b], discussed in the previous section, we can expect signals ranging from 13 MeV (1.3 keV/cm for minimum ionizing particle, multiplied by a gas gain $M = 10^4$) up to 4000 MeV (2 MeV/cm for slow alpha particles, multiplied by a gas gain $M = 10^4$, and an attenuation factor M_α / M of about 0.2), i.e., a dynamic range of about 300. This represents a considerable challenge for the design of the electronics. We address here only the amplitude-to-digital converters (ADC's).

In Section 5.5 we showed that the rms noise should not be more than about 1% of the minimum ionizing signal. Similarly the digitization error introduced by the finite channel width of the ADC should not be more than 1%. This implies that the signal for minimum ionizing particles should be located in channel 100 / $\sqrt{12}$, i.e. 29, or higher. For the desired dynamic range of 300 this requires a 13- or 14-bit ADC. At the upper end of the range the resolution of such an ADC would be 300 times better than needed, and needless expense would be incurred. Fortunately, Hallgren and Verweij [Ha 80] have devised a way of producing a non-linear response (logarithmic would be ideal) to extend the dynamic range of an ADC without the expense or data acquisition time involved if the number of bits is increased. The method has been used, for example in the UA1 experiment at CERN, and some units are commercially available, which operate at speeds up to 100 MHz.

The method involves driving the reference chain of a flash ADC with part of the input signal. If V_i is the input signal and V_b is the reference voltage, the normal response $2^{N-1}\ V_i \,/\, V_b$, where N is the number of bits in the ADC, becomes:

$$2^{N-1} \frac{V_i}{a\ V_i + V_b} \tag{5.6}$$

where a is a constant determined by the values of certain resistors. The normal full-scale input voltage $V_{imax} = V_b$ becomes

$$V_{imax} = \frac{V_b}{1 - a} \tag{5.7}$$

while the relative channel width $\Delta V_i \,/\, V_i$ is given by

$$\frac{\Delta V_i}{V_i} = \frac{1}{2^{N-1}} \left(a \sqrt{\frac{V_i}{V_b}} + \sqrt{\frac{V_b}{V_i}} \right)^2 \tag{5.8}$$

If we set this equal to $\sqrt{12}/100$, satisfying our limit on the digitization error, for $V_i = V_{imax}$, we obtain an expression for a:

$$a = 1 - \frac{100}{2^{N-1}\sqrt{12}} \tag{5.9}$$

The digitization error will be less than $\sqrt{12} \,/\, 100$ for all inputs between V_{imax} and $V_{imin} = V_{imax}\ (1-a)^2/a^2$. This defines the usable dynamic range for a given value of N and hence a , derived from Eq. 5.9.

For a 1% digitization error, an appropriate solution is for a 9-bit ADC extended to approximately 13 bits by setting $a = .9718$, for a dynamic range of 279. The same result can be obtained for a 2% digitization error using an 8-bit

ADC extended to 12 with $a = .9435$, and so on. The original version of such a device [Ha 80] had 6 bits extended to 9. A commercially available unit [Le] has 6 bits extended to 8, and is planned for 8 bits extended to 10. The demands of the EOS TPC are somewhat greater.

5.7. Comparison with Other Time Projection Chambers

The EOS TPC has a great deal in common with the PEP-4, ALEPH and DELPHI TPC's. Table 5.1 shows a comparison of some of the principal design parameters of these detectors.

The PEP-4 TPC, which has operated successfully for several years, uses a gas pressure of 8 atmospheres, which serves to increase the dE/dx signal, and to reduce diffusion. We have felt that the advantages of operation at atmospheric pressure outweigh these advantages, in our application.

The single-ended configuration of the EOS TPC is appropriate for the physics involved. A double-ended TPC would have electronics downstream, where we have striven to reduce the amount of material. The inner radius of the EOS TPC is made small enough to achieve good acceptance of the "fireball" particles and yet large enough to permit addition of fragmentation detectors at a later stage.

Table 5.1. Comparison of some design parameters of TPCs.

	Field	Configuration	Length	Inner radius	Outer radius	Space points per track	Sense wires per track
PEP-4	1.4 T	double-ended	2 × 1 m	0.2 m	1.0 m	15	183
ALEPH	1.5 T	double-ended	2 × 2.2 m	0.38 m	1.7 m	21	340
DELPHI	1.2 T	double-ended	2 × 1.35 m	0.3 m	1.1 m	16	192
EOS	1.5 T	single-ended	2 m	0.1 m	0.9 m	80	160

	No. of pads	No. of wires	Wire to pad distance	Pad spacing	Sampling rate
PEP-4	13824	2196	0.4 cm	0.8 cm	10 MHz
ALEPH	∼41000	∼6000	0.4 cm	0.67 cm	12.5 MHz
DELPHI	20184	2256	0.4 cm	∼0.7 cm	15 MHz
EOS	∼25000	∼960	varies	varies	5 MHz

The large number of space points per track (measured using the pads) in the EOS TPC is dictated by the requirement of good multihit capability, and of good dE/dx resolution (also achieved using the pads). The number of pads in the EOS TPC is comparable to those in the other detectors. Our multihit calculations showed that a larger number is necessary if the pad size is uniform, but use of a variable pad size reduces the number to its present value.

Finally, the sampling rate has been set for the EOS TPC using a criterion similar to that used for determining the size of the pads. It is probable that a detailed study of fluctuations, which has not yet been carried out, will dictate a higher sampling rate. We would adopt this reluctantly, because of the proportional increase in the data to be transferred and analyzed.

Chapter 6

6. Time - of - Flight Array

6.1. Objectives

The addition to the TPC of plastic scintillation detectors for time-of-flight measurement serves two primary purposes: to provide particle identification information, and to provide a fast trigger for the TPC. For particle identification, the scintillators provide time-of-flight information that resolves the dE/dx ambiguities illustrated, for example, in Figure 4.10. Away from the ambiguities it increases the confidence level of the particle discrimination, enhancing that achieved by dE/dx measurement. As a fast trigger for the TPC, some obvious choices are a minimum bias trigger, a multiplicity trigger, and a planarity trigger to select events with a particular azimuthal orientation or cylindrical symmetry.

The inside of the magnet, shown in Fig. 1.1, will be lined with a cylindrical arrangement of plastic scintillation detectors segmented azimuthally, referred to as the "barrel array". Downstream from the TPC (3.1 meters from the target) will be a planar array of scintillation detectors, the "downstream array". Combined, the barrel and downstream arrays subtend 89% of 4π.

In this chapter we discuss first the operation of the barrel array and downstream array. We discuss the problem of double hits in the scintillators and how to alleviate it. Next we examine the particle identification achieved by the time-of-flight array alone, and in combination with dE/dx measurement. Finally, we discuss two other options which we have considered to obtain a velocity measurement for each particle: the ring imaging Cherenkov detector and the planar spark counter.

6.2. The Barrel Array

The inside of the magnet will be lined with scintillators, each 3.6m long, with a light guide and photomultiplier tube at each end. The cross section of each scintillator is determined in thickness by the desire to achieve sufficient light output while avoiding an excessive number of nuclear interactions and in width by the desire to achieve as great azimuthal segmentation as possible. The proposed cross section is 2 cm thick and 1 ° wide (1.75 cm at 1 m radius). A smaller cross section than this will cause light collection problems. To simplify construction, 36 of the scintillator elements will be bevelled to a trapezoidal cross section. The remaining 324 segments will be rectangular in cross section and the whole barrel assembly will be a 36 sided polygon.

Pilot U (Nuclear Enterprises) scintillation plastic and R2083 (Hamamatsu) phototubes are being tested as a prototype scintillation detector element. Our timing results will depend on our choice of light guide geometry, and prototyping will determine precisely what time resolution will be achievable. Our expected time-of-flight resolution is 400 ps FWHM, ($\sigma = 170$ ps) based upon reported resolutions measured in other large time-of-flight arrays using similar hardware.

Table 6.1 compares the properties of some existing time-of-flight detectors with this project.

A schematic of one of the scintillator elements is shown in Figs. 6.1 and 6.2. For the geometry shown, the pulse heights PH_L and PH_R in the left and right phototubes; respectively, are given by [Ge 77]:

$$PH_L = G_L L_o \exp(-(s + x)/D) \tag{6.1}$$

(6.1)

$$PH_R = G_R L_o \exp(-(s - x)/D) \tag{6.2}$$

where

D = light attenuation distance

$2s$ = length of scintillator

x = position at which the particle strikes the scintillator, measured from the centre

G_L, G_R = gains of the left and right phototubes

Table 6.1
Comparison of some large TOF arrays.

Project	Length of scintillator barrel (m)	Thickness of scintillator (cm)	Width of scintillator (cm)	Phototube used	Scintillation plastic	Achieved fwhm (ps)
EOS	3.1	2.0	1.75	R2083	Pilot U	400*
Argus	2.2	2.0	9.3	RCA 8575	NE110	528
MPS	1.83	5.08	15.24	XP2020	Pilot F	354
Mark III	3.2	5	15	XP2020	Pilot F	424
Topaz	4.0	4.1	12.7		BC412	472

*expected

Table 6.1 compares the properties of some existing time-of-flight detectors with this project.

A schematic of one of the scintillator elements is shown in Figs. 6.1 and 6.2. For the geometry shown, the pulse heights PH_L and PH_R in the left and right phototubes; respectively, are given by [Ge 77]:

$$PH_L = G_L L_0 \exp(-(s + x)/D) \qquad (6.1)$$

(6.1)

$$PH_R = G_R L_0 \exp(-(s - x)/D) \qquad (6.2)$$

where

D = light attenuation distance

$2s$ = length of scintillator

x = position at which the particle strikes the scintillator, measured from the centre

G_L, G_R = gains of the left and right phototubes

Table 6.1
Comparison of some large TOF arrays.

Project	Length of scintillator barrel (m)	Thickness of scintillator (cm)	Width of scintillator (cm)	Phototube used	Scintilation plastic	Achieved fwhm (ps)
EOS	3.1	2.0	1.75	R2083	Pilot U	400*
Argus	2.2	2.0	9.3	RCA 8575	NE110	528
MPS	1.83	5.08	15.24	XP2020	Pilot F	354
Mark III	3.2	5	15	XP2020	Pilot F	424
Topaz	4.0	4.1	12.7		BC412	472

*expected

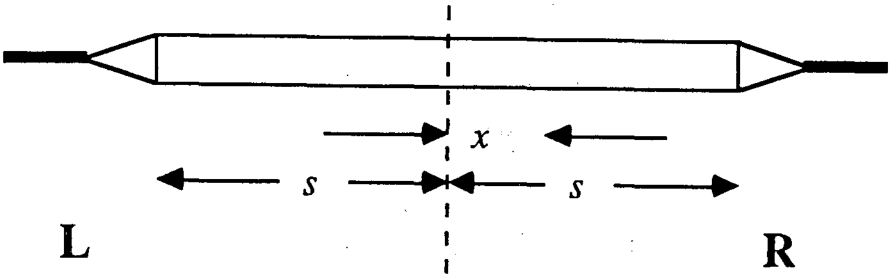

Fig. 6.1. Schematic of a barrel scintillator element. L and R refer to the photomultiplier tubes at the left and right ends. s is the half-length of the scintillator, and x is the distance from the center to the position of the charged particle.

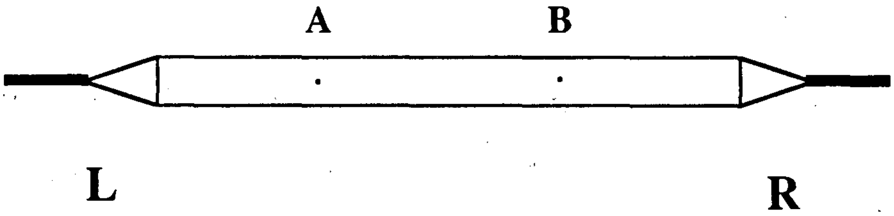

Fig. 6.2. Two charged particles, A and B, can hit a single scintillator element.

L_o = light produced in the scintillator.

Combining the two equations 6.1 and 6.2 gives:

$$x = \ln(PH_R / PH_L) + C_1 \tag{6.3}$$

and

$$L_o + C_2 \sqrt{PH_L \times PH_R} \tag{6.4}$$

where C_1 and C_2 are constants depending on G_L, G_R, s, and D.

By making time measurements of a single particle in the scintillator, the observed arrival times T_L and T_R in the left and right photomultiplier tubes are given by:

$$T_L = T_a + (s + x)/v \tag{6.5}$$

$$T_R = T_a + (s - x)/v \tag{6.6}$$

where

T_a = particle arrival time in the scintillator, and

v is the velocity of light in plastic ($= c/n$, where n, the refractive index of the plastic $\sim$ 1.5.

If we assume that only one particle strikes a scintillator, and position information is obtained from the TPC, T_a can be found from Eq. 6.5 or from Eq. 6.6. The two independent measurements should yield the same result if the assumption is correct. Then combining these two equations gives:

$$T_a = (T_L + T_R)/2 - s/v \tag{6.7}$$

$$x = (T_L - T_R)v/2 \tag{6.8}$$

The arrival time T_a is determined from Eq. 6.7 with better accuracy than from Eq. 6.5 or Eq. 6.6 alone, while the particle position obtained from pulse height information (Eq. 6.3) and from timing information (Eq. 6.8) should verify the position determined by the TPC.

6.3. The Downstream Array

For collisions at 1.8 GeV/A, roughly 50% of the participant charged particles will strike the downstream array. Thus 360 downstream scintillator elements are required in order that the multiple hit probability in a given scintillator element is roughly equal in the barrel array and in the downstream array.

Considerable flexibility is available for the design of this array. The flight path could be increased, but the distance of 3.1 m provides adequate resolution and helps simplify particle tracking from the TPC into the scintillators. However, multiple scattering in the end plate of the TPC is found to be sufficient that associating individual tracks with given elements of the downstream array would be difficult. A solution to this problem would be to extend the TPC to the end of the magnet so that its end plate would be close to the scintillators and multiple scattering in it would not cause appreciable lateral displacements of the tracks. The high voltage electrode of the TPC would be replaced by a mesh, and the extra volume of the TPC would not be used for any measurements.

The configuration of the downstream array also presents a variety of options such as an array of slats with a phototube at each end (as in the Plastic Wall) [Bad 82] or an array of rectangular elements with air light guides (as in the Streamer Chamber array). The design of the downstream array will have to be done in close coordination with the detailed design of the magnet, since the possible locations of phototubes in the fringe field may be the controlling factor. We will attempt to increase the number of scintillators in the downstream array substantially above the 360 used in the barrel. This will help alleviate the multiple hit problem, which is discussed for the barrel array in the next section.

6.4. Double-Hit Resolution

For a U-U collision at 1 GeV we expect 100 particles on the average to strike the downstream array and equal number to hit the barrel array. Assuming we have segmented the scintillators appropriately we find, for 360 detectors in each array, the probability of clean measurement of a specific particle is 0.761. The TPC will inform us when a multiple hit situation occurs, so that the particles involved can either be rejected cleanly, or analyzed using momentum and dE/dx information only. This will be useful in most instances.

We now consider, for the barrel array, the possibility of extracting useful timing information for scintillators that are hit twice in one event. Consider two particles from a given event that arrive in the same scintillator, but at different locations, as shown in Fig. 6.2. Leading-edge-timing electronics will allow the time measurement of the first light front to arrive at the photo-cathode of a given photomultiplier tube, given that the second light pulse arrives a sufficient amount of time later.

There are two situations that need to be investigated:

(*a*) The first light front to arrive at each photomultiplier tube comes from the particle nearest to it in the scintillator. Then the arrival times of both particles can be determined from Eqs. 6.5 and 6.6, each with an accuracy a factor of $\sqrt{2}$ worse than for single hits, since only a single photomultiplier tube is used for each.

(*b*) The first light front to arrive at each photomultiplier tube comes from the same particle (the one with the smaller T_a, see Eq. 6.8). Here all timing information on the second particle is lost, but the timing of the first particle should be equal to that obtained for single hits.

These situations can be discriminated by calculating x in Eq. 6.7. If the result is consistent with the position of one of the two particles as measured by the TPC, then case (*b*) is true; otherwise case (*a*) is true.

Monte Carlo calculations show that for 1.8 GeV/A Ar+KCl case (*a*) and its logical complement occur with varying probability, depending on the assumption for the minimum time separation ("offset") needed between two consecutive light fronts at a photo-cathode in order that the first is measured successfully. The results of these calculations are shown in Table 6-2. 1000 double hits, or 2000 particles, were calculated for each value of the offset.

Table 6.2
Monte Carlo simulation of 1000 double hits in
a barrel scintillator element.

offset(ns)	(i)	(ii)	(iii)	(iv)
0	551	304	145	0
0.5	435	222	120	223
1.0	349	167	90	394
2.0	215	96	52	637
3.0	127	64	31	778
6.0	8	30	10	952

where

$$(i) \equiv (A \text{ arrives first in } L) \cdot (B \text{ arrives first in } R)$$

$$(ii) \equiv (A \text{ arrives first in } L) \cdot (A \text{ arrives first in } R)$$

$$(iii) \equiv (B \text{ arrives first in } L) \cdot (B \text{ arrives first in } R)$$

$$(iv) \equiv \overline{(i) \text{ or } (ii) \text{ or } (iii)}$$

We expect that a realistic value for "offset" is 0.5 ns, which we would like to confirm with prototype scintillator studies. Thus, by using leading-edge-timing electronics we may recover roughly 61% of the double-hit particles in the barrel scintillators.

Using these results for both Au+Au central collisions and Ar+KCl central collisions we can calculate the overall efficiency of the barrel array for time-of-flight measurements. In Au+Au central collisions, 76% of the particles are measured clearly as single hits, 21% occur as double hits, and 3% occur as higher multiplicity hits. The overall efficiency is 89% (76% + 61% × 21%). In Ar+KCl central collisions there is a dramatic improvement: 94.3% of particles are cleanly measured as single hits, and an additional 3.8% are extracted as shown above from the double hits for a total of 98.1% of all particles.

We are investigating methods of extracting time information for the remaining double-hit particles. Waveform digitization is a straightforward, but formidable approach, since it implies a sampling rate greater than 1 GHz. This may be too costly compared to the potential physics return.

6.5. Particle Identification by Time-of-Flight

Figure 6.3 serves as a reminder of the ambiguity problem in the particle identification by dE/dx. It shows the discrimination between pions and other particles obtained using the TPC alone. Figure 4.10 shows the discrimination for kaons.

Figure 6.4 shows time of flight spectra calculated for the barrel array at 30°, in the reaction Ar+KCl at 1.8 GeV/A (see Table 3.1) which we have used as a test case. It shows that the time of flight spectra do not lend themselves to a simple cut to separate any two particles in the barrel, except to make a rough cut between pions and protons. The pion spectrum terminates at about 7 ns because particles with a transverse momentum less than 225 MeV/c can never reach the barrel, because of spiraling (see section 4.2). The figure also emphasizes the large ratio between the proton and kaon yields which is our most difficult problem in particle identification.

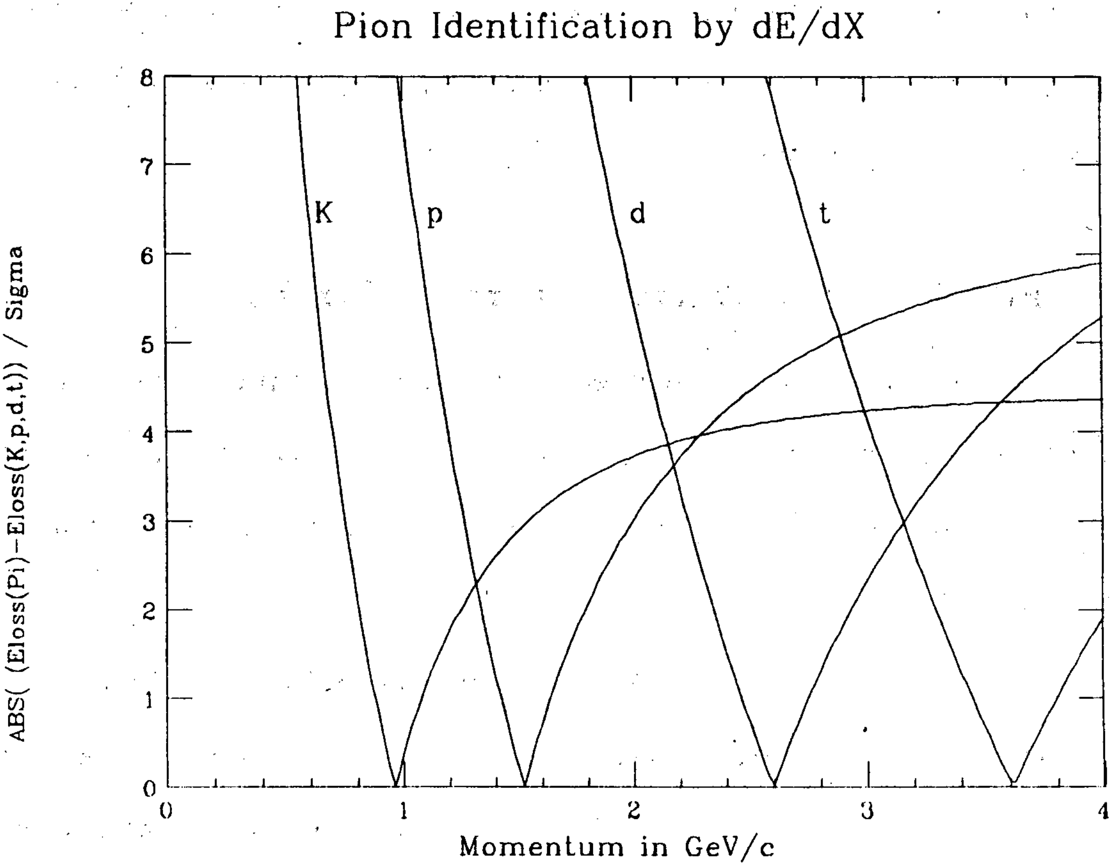

Fig. 6.3. Difference in the energy loss between pions and kaons, protons, deuterons, and tritons as a function of momentum. The curves are normalized to the expected rms error of the energy loss in the TPC.

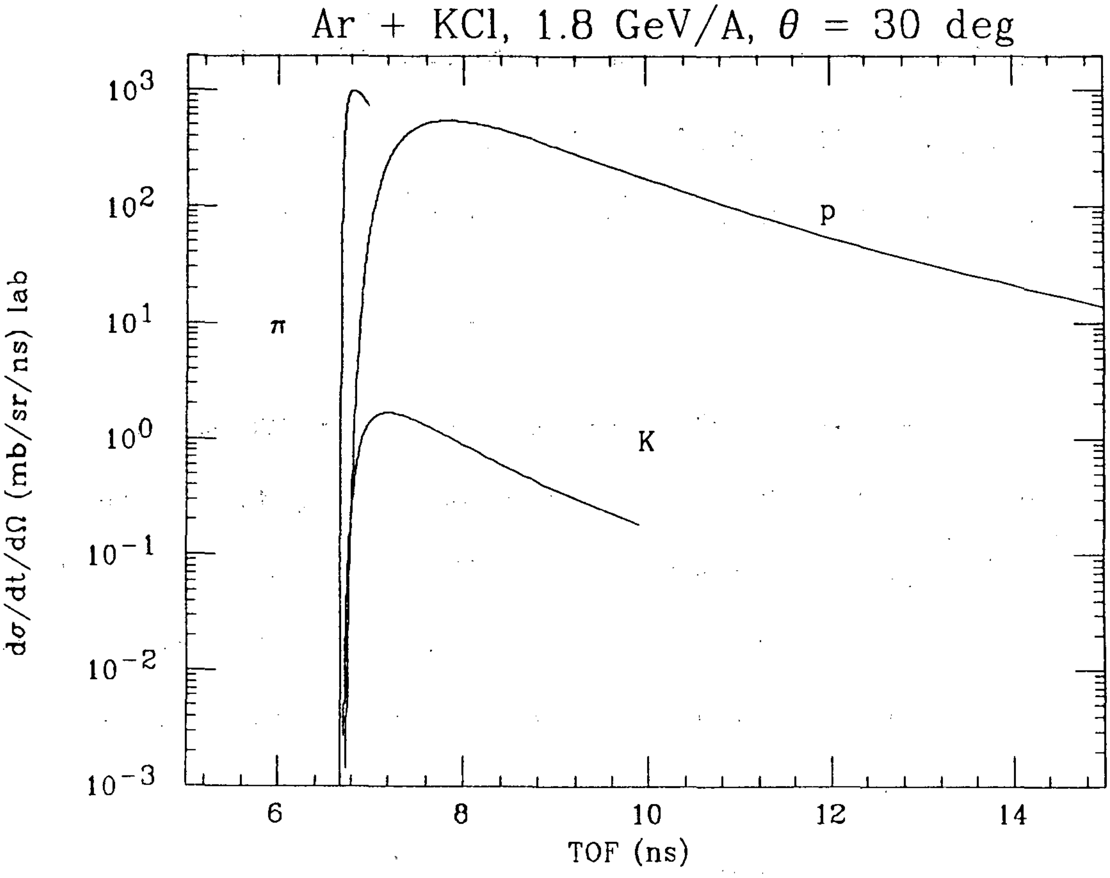

Fig. 6.4. Cross section for pions, kaons, and protons versus time of flight for 1.8 GeV/A Ar+KCl events, at $\theta = 30^o$.

Figure 6.5 shows the time-of-flight differences which we expect to achieve at $\theta = 17.9\,^\circ$, (the most forward angle on the barrel array) normalized to the timing resolution (σ = 170 ps), and plotted as a function of momentum. For pions and kaons we are mainly concerned with momenta below 2 GeV/c. Protons extend up to 6 GeV/c and alphas to 9 GeV/c (see Figs. 3.1 and 3.2).

We have calculated, for the Ar+KCl reaction, the ratios of cross sections multiplied by the survival fraction of decaying particles,

$$SF = \exp \frac{-L}{\beta\gamma L_0}$$

where $L_0 = c\,\tau$ and τ is the mean lifetime, for $\theta = 17.9\,^\circ$ and $\theta = 90\,^\circ$, respectively. The results for $\theta = 17.9\,^\circ$ were shown in Fig. 3.3. We have taken these ratios into account to determine the maximum momentum for which kaons are separated from pions and protons, and pions are separated from protons. More precisely, we demand at least 2σ (3σ) separation between particles that have equal cross section, and for a cross section ratio of 1 : n we demand the confidence level [Pa 86] to be n times lower. The results are shown in Table 6.3. It is clear from Figs. 3.1 and 3.2 that for momenta for which the cross section $d\sigma/dpd\Omega$ is greater than 10^{-4} mb/(sr·MeV/c) kaons and pions will be separated from each other and from the protons. Note that the π/K upper limits depend strongly on the different shapes of the momentum distributions for pions and kaons, resulting from the different fireball temperatures.

Table 6.4 shows the momenta below which protons, deuterons, ^{3}H (and ^{3}He) and ^{4}He will be separated in the downstream array. Thus the downstream

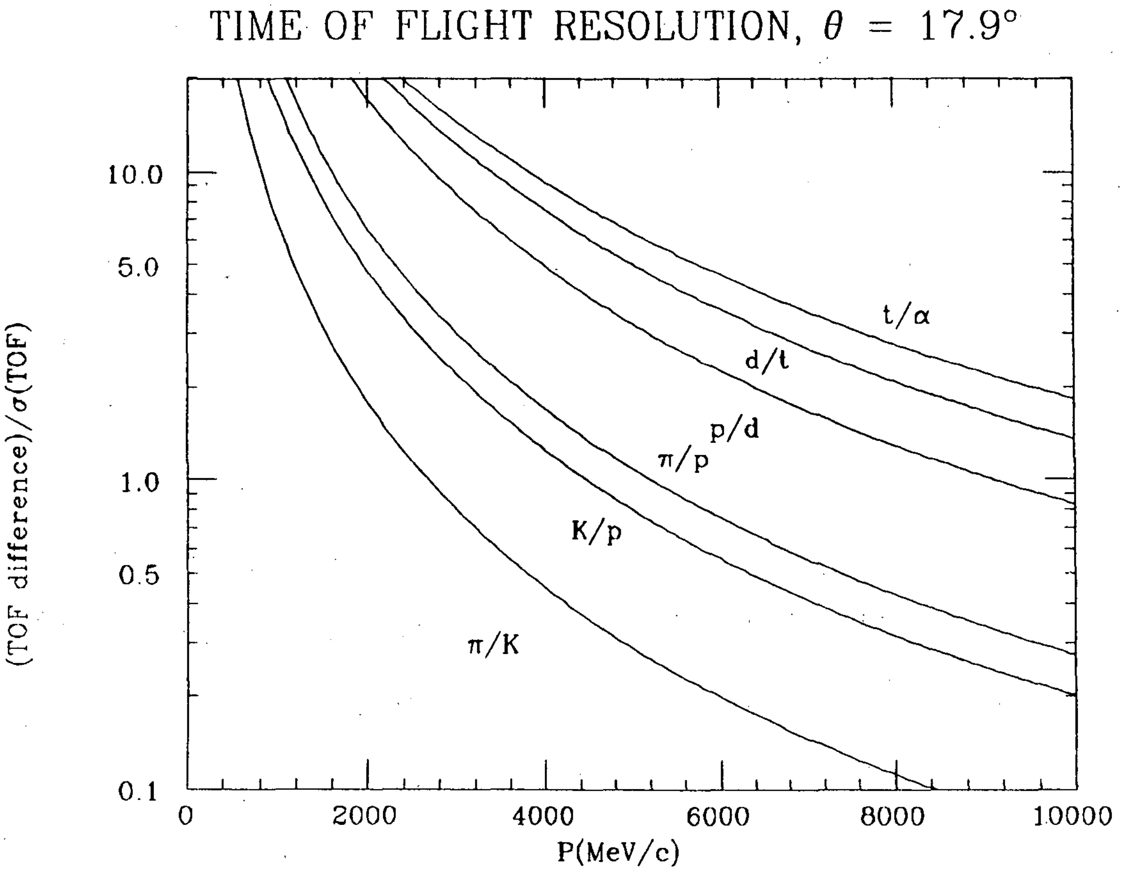

Fig. 6.5. Time of flight difference for pairs of particles normalized to the expected TOF resolution (170 ps).

Table 6.3
The maximum momentum for which two different particles are separated by at least $2\sigma(3\sigma)$ in time of flight at $\theta = 17.9^\circ$ and 90°.

	$p_{\max}(lab)$ GeV/c			
	2σ		3σ	
	90°	17.9°	90°	17.9°
π/K	1.0	1.6	0.85	1.3
K/p	1.1	2.2	1.0	2.0
π/p	1.3	2.5	1.1	2.3

scintillators will resolve almost the entire range of laboratory frame momenta for which $d\sigma/dpd\Omega$ is greater than 10^{-4} mb/(sr·MeV/c). The cross section ratios vary relatively slowly as a function of θ between 4° and 18°. Also the straight-line flight path decreases by only 5% over the same angular range. Therefore the separation of pions and kaons from each other and from protons is expected to be equivalent to that in the barrel at $\theta = 18^\circ$ (see Table 6.2).

Figure 6.6 summarizes in the form of a nomogram the effect of combining dE/dx (from the TPC) and time-of-flight information. The ordinate shows the dE/dx differences between pairs of particles, divided by the standard deviation of

Table 6.4
The momentum below which two different particles are separated by $2\sigma(3\sigma)$ in the downstream time-of-flight array.

	$p_{\max}(lab)$ GeV/c	
	2σ	3σ
p/d	5.2	4.6
d/t	6.7	6.0
t/α	7.7	7.0

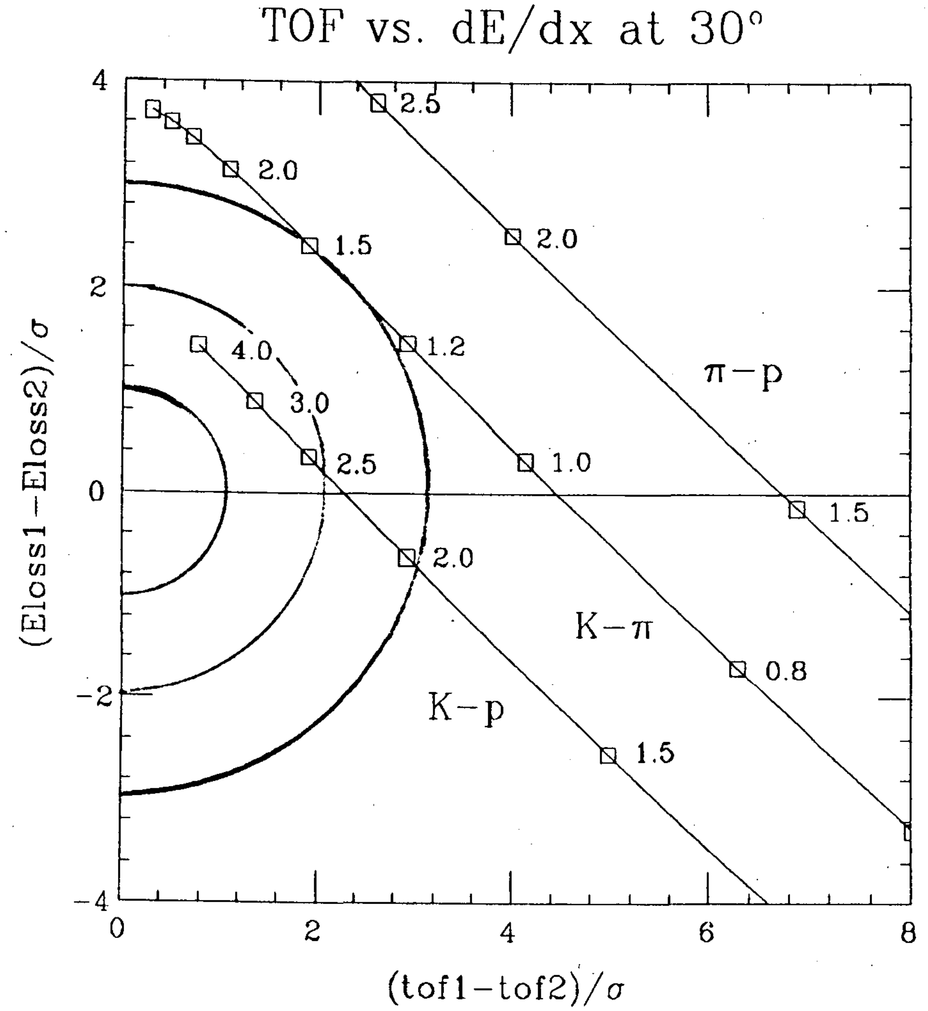

Fig. 6.6. Time of flight difference and E_{loss} difference between pairs of particles, normalized to the respective resolutions, at $\theta = 30^o$. The sloped lines represent the separation of pairs of particles, as marked. The numbers on the lines are the momenta of the particles in GeV/c. The circles have radii of 1σ, 2σ and 3σ, where $(radius)^2 = \sigma_{tof}^2 + \sigma_{Eloss}^2$.

a single measurement, for $\theta = 30°$. The abscissa similarly shows time-of-flight differences, normalized to the measurement uncertainty, σ=170 ps. The circles show 1σ, 2σ, and 3σ separation for dE/dx and time-of-flight measurements combined. The particle momenta are indicated on the lines for $K-p$,$K-\pi$ and π–p differences. For $K-p$ separation we see that a combined 3σ is exceeded for momenta up to 2.0 GeV/c, where the cross section is below our measurement threshold of 10^{-4}mb/sr · MeV/c. At 1.5 GeV/c either dE/dx or time-of-flight can be used. The $K-\pi$ and π–p separations exceed 3σ for all momenta. A similar plot for $\theta = 90°$ shows that dE/dx or time-of-flight will suffice separately at all momenta expected to be encountered.

Figure 6.7 shows a scatter plot of dE/dx versus time-of-flight for simulated Ar + KCl events at 30° and momentum 1.4 GeV/c (the protons have been reduced in number by a factor of 12). It shows clearly the value of the time-of-flight measurement, without which the pions and kaons would be confused.

6.6. Alternative Methods

Plastic scintillators have been chosen to supplement the TPC for several reasons. The scintillators are economical of space, their technology is well known, and construction methods are easy and well-established. The simple electronic readout is convenient to use to generate a fast trigger for the overall detector. On the other hand, the sensitivity of the photomultipliers to magnetic fields causes problems. In particular, to keep the phototubes in regions of low magnetic field we are forced to use the barrel array geometry with its limited segmentation

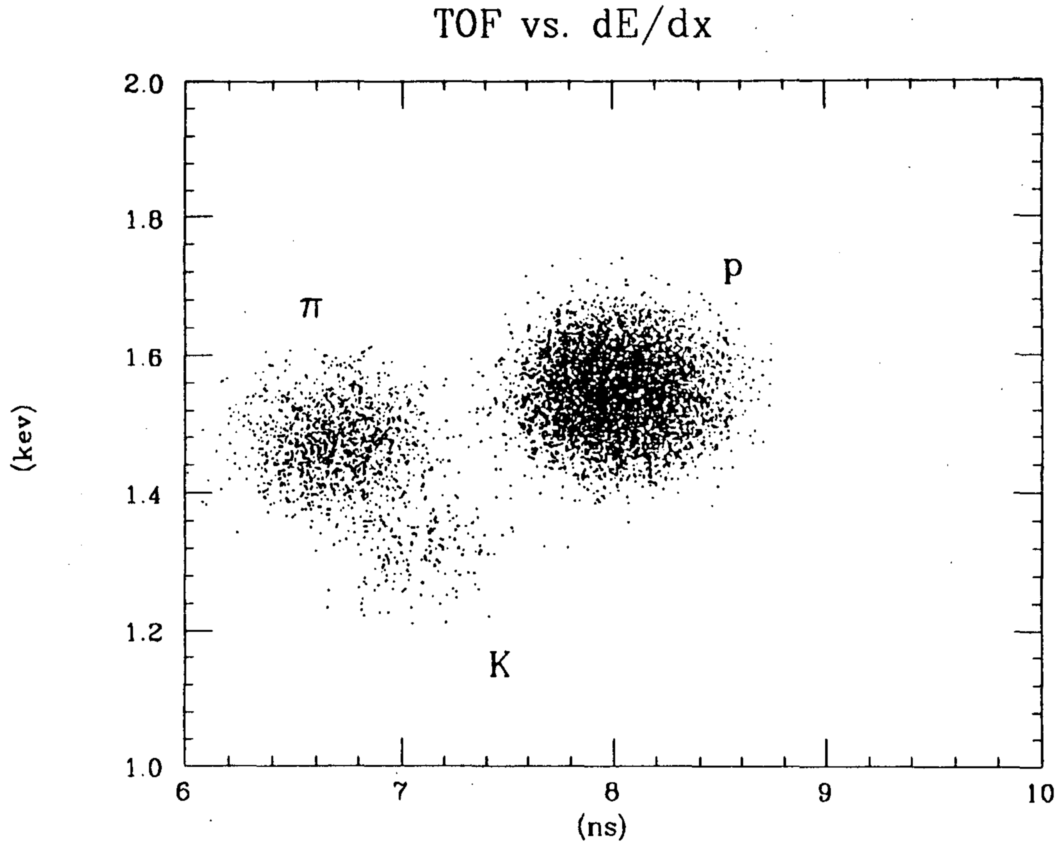

Fig. 6.7. Scatter plot of E_{loss} versus time of flight for pions, kaons, and protons in Ar+KCl events at 1.8 GeV/A at $\theta = 30°$, and $p = 1.4$ GeV/c. The protons have been reduced in number by a factor of 12.

capability. Furthermore, to obtain sufficient timing resolution, we need to use very expensive phototubes and pay great attention to the choice of light guide geometry. We have therefore examined other possibilities which are in principle capable of better resolution both in space and in velocity, specifically the use of ring imaging Cherenkov detectors and of planar spark counters.

Ring imaging Cherenkov detectors [Se 77] are in use or under construction for a variety of high-energy physics experiments (e.g., OMEGA [Ap 86] and DELPHI [De 84] at CERN, SLD [As 86] at SLAC, and E605 [Ad 83] at Fermilab). They consist of a Cherenkov radiator medium, which for our application would be a liquid such as FC-72 [3M] (perfluorohexane, C_6F_{14}, $n = 1.277$), and an ultraviolet photon detector consisting of a multi-wire proportional chamber with an admixture of TMAE [An 81] (tetrakis dimethyl amino ethylene) which has a high quantum efficiency in the UV range. Since no focussing of the Cherenkov light would be used the resolution is determined by the thickness of the liquid radiator. We find that 1 cm of FC-72 and a spacing of 11.5 cm between radiator and detector would give excellent sensitivity and velocity discrimination. To arrive at these figures we required a mean number of 8 photoelectrons at threshold (a 99% probability of at least 3) and 3σ K-π separation up to 1.5 GeV/c. The mean number of photoelectrons for $\beta \rightarrow 1$ is 23. The overall thickness of the detector would be about 20 cm. The disadvantages of this method are several. The device is at least as complex to construct and operate as the TPC itself. Pattern recognition is difficult for our high-multiplicity events. Finally there are light-loss problems associated with total internal reflection of some of the UV photons for particles forward of $\theta = 71^\circ$.

Planar spark counters [Fu 85] provide an alternative time-of-flight method with timing resolution potentially much better than can be achieved with large scintillators. They consist, typically, of two plane-parallel electrodes separated by a 1.0 mm gap filled with an argon-hydrocarbon mixture at 10 atm. A voltage of about 5 kV is applied across the gap, in which a streamer discharge is induced by any charged particle. To localize the discharge region, and prevent the capacitative discharge of the whole counter, the anode is made of high resistivity semiconducting glass. The resulting size of the discharge area is of the order of the gap width. A signal of several volts into 50 ohms, with rise time $\sim$ 100 ps, provides timing resolution with $\sigma <$ 100 ps. In addition, position measurements with an accuracy comparable to the gap width can be obtained. Planar spark counters of size 10 cm × 1 m are presently being tested [Og 86] at SLAC under realistic running conditions. The technology appears very promising. The main objections to its use are two-fold. First, the time spectrum is not gaussian below about 1/10 of the maximum, having a broad tail on each side. Secondly, and perhaps acceptable for our application, the time resolution deteriorates at high count rates. Both these effects need further study to understand their origin.

Chapter 7

7. Detection of Secondary Vertices

7.1. Location of Vertex

One of the advantages of tracking detectors is their ability to recognize particles which do not emerge from the primary vertex. The Λ^0 is produced in a few per cent of central collisions at the maximum Bevalac energy. It can be recognized through its decay into $p\ \pi^-$ which occurs with 64.2% probability. The decay length $c\,\tau$ is 7.89 cm. The $K_s{}^0$ is also expected to be seen, and recognized through its decay into $\pi^+\pi^-$ with 68.6% probability and decay length $c\,\tau$ of 2.68 cm. In order to investigate the ability of the EOS detector to measure secondary vertices, we have carried out a Monte Carlo calculation of Λ^0 production. We assumed 2.1 GeV/A for the beam energy and a thermal distribution of Λ^0 with a temperature of 100 MeV.

Table 7.1 shows the locations calculated for the Λ^0 decay vertex, relative to the target. These figures show, for example, that 90% of all the Λ^0 decay within a distance of 22.1 cm downstream from the target. Similarly 90% of the Λ^0 decay within a cylinder of radius 8.70 cm. Only 3.5% of the Λ^0 survive beyond the 10 cm radius of the beam pipe.

Table 7.1. Fraction of Λ^0-particles that decay within a given distance of the target in the radial and downstream directions.

Fraction	Downstream	Radial
10%	0.91 cm	0.28 cm
50%	5.92 cm	1.92 cm
90%	22.10 cm	8.70 cm

Another calculation showed that in 86% of charged decays both the proton and pion from the Λ^0 decay emerge from the beam pipe where they can be measured. This represents 56% of all Λ^0 decays.

Initially, we attempted to design the TPC so that the Λ^0 would decay within its volume, with the intention of recognizing the decay vertex from the hit pattern. However, the track density in the region containing the Λ^0 decays is too great. Nevertheless, the ability of the TPC to reconstruct the vertices from the precise position and momentum measurements made at larger radii turns out to be excellent.

7.2. Pattern Recognition

For the remainder of our investigation, we ignored the effect of the magnetic field to simplify the study of pattern recognition. The Λ^0 decay pattern is then as illustrated in Fig. 7.1. The proton and pion tracks, extrapolated back, miss the vertex by δ_p and δ_π respectively. Table 7.2 shows the probability that δ_p or δ_π will be less than various distances. We note that because the proton carries

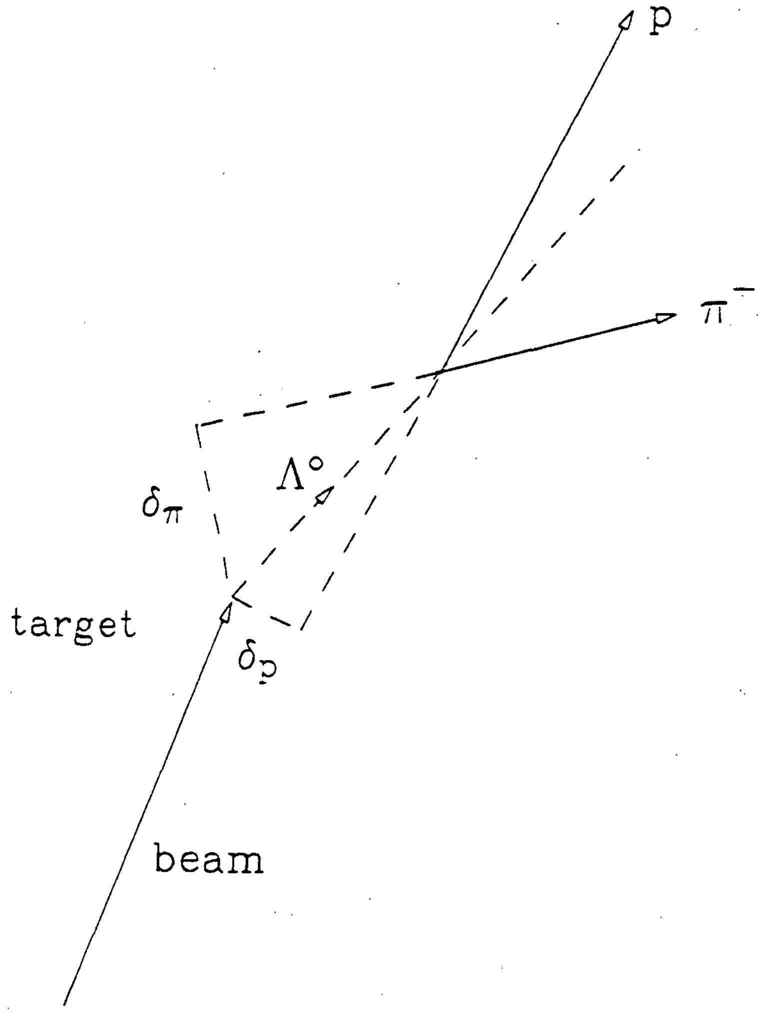

Fig. 7.1. Production of a Λ^0 and of its decay via the channel $\Lambda^0 \rightarrow \pi p$.

most of the momentum of the Λ^0, it makes a smaller angle with the Λ^0 direction than the pion does, so that δ_π is usually much larger than δ_p .

Table 7.2. Fraction of Λ^0 particles that decay with δ_p and δ_π less than the given values.

Fraction	δ_p	δ_π
10%	0.11 cm	0.38 cm
50%	0.46 cm	2.58 cm
90%	1.70 cm	11.60 cm

The fraction of the decays that can be measured depends on our ability to tell whether the values of δ_p and δ_π in Table 7.2 are different from zero. We adopted a conservative value of 0.6 mm for the uncertainty in these quantities, based on the accuracy of position measurement in the TPC and allowing for extrapolation back to the target position. Then requiring 3σ deviation from zero for both δ_p and δ_π removes 25% of the remaining Λ^0, for an overall efficiency of 42%.

Finally, a random choice of a proton and a pion among the large number produced in a typical event might simulate a Λ^0. We considered a sample event with 121 protons and 30 pions, a total of 3630 possible combinations. To estimate the effectiveness of a mass reconstruction as a selection criterion, we first determined our resolution in Λ^0 effective mass by including multiple scattering and energy loss for the decay particles. The full width was about 5 MeV. Of the 3630 possible $p\,\pi$ pairs only 5 fell in that mass range. When we further require that both proton and pion should appear to originate more than 3 s.d. from the target, this number is reduced by the factor 7.3 10^{-6}, to 3.6 10^{-5} per event[†]. There would be one spurious Λ^0 for about every 500 true Λ^0, after allowing for Λ^0 detection efficiency.

Thus the combination of mass reconstruction and vertex recognition enables us to measure Λ^0 with good efficiency and high discrimination against spurious combinations.

[†] This does not include the additional restriction that the Λ^0 candidate reconstructed from the two tracks should appear to originate from the target.

Chapter 8

8. Data Acquisition and Analysis

8.1. Interaction Rates

In Section 5.4 we examined the intrinsic capability of the TPC to handle high event rates. For Au+Au, Eq. 5.4 and the subsequent discussion showed that event rates up to $10^4/s$ are feasible, provided that the TPC trigger rate is kept below about $10^2/s$. We also noted that in most experiments the event rate would be kept below about $10^3/s$ because of the $40\mu s$ sensitive time of the TPC. In this section we describe a typical Au+Au experiment, showing that the overall performance of the system is excellent. In sections 8.2 and 8.3 we examine the rates at which data can be recorded and analyzed, as well as the problem of data storage.

The overall experimental configuration is shown in Fig. 8.1. A is an upstream scintillator used to define the presence of a beam particle and to provide a start signal for the time-of-flight system. For a scintillator of nominal thickness 0.01 cm, the energy loss will be 125 MeV, yielding excellent timing. B is a veto detector to reject particles from beam interactions in A (0.2% probability). C is the time-of-flight scintillator array for the TPC. D is a 0.01 cm thick, 1 cm diameter, scintillator 5 m downstream from the target to reject non-interacting beam particles (used only for near-central collisions).

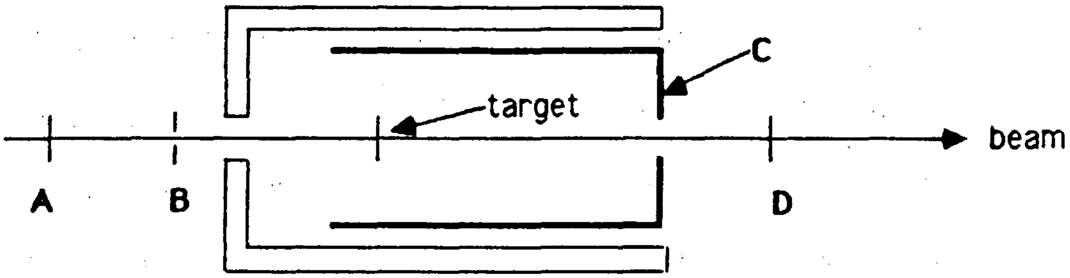

Fig. 8.1. Scintillators involved in a triggering scheme for the TPC. A and D are thin scintillators, B has a hole in it, and C is the time of flight array.

The first level trigger for the TPC is $A\bar{B}C\bar{D}$ with special conditions imposed on C (the time-of-flight array). Depending on the trigger pattern stored in the hardware lookup tables, this second level trigger can be a minimum bias trigger or a central trigger defined by high multiplicity. Other constraints could be considered, such as azimuthal isotropy (central collisions) or planarity. Other external second level triggers could be added. A strange particle trigger would be very valuable, and the design of one is under study.

Consider a gold target of thickness 0.058 g/cm^2 and a gold beam of 10^6/sec at 1.0 GeV/A. The total interaction cross section is given by $\sigma_{int} = \pi(1.15\, A_1^{1/3} + 1.15\, A_2^{1/3})^2 \times 10^{-26}$ cm^2 which is 5.6×10^{-24} cm^2 for this case. The interaction probability in the target is 10^{-3}. The collision rate is 10^3/sec, of which about 10^2/sec can be considered near-central.

The target thickness is chosen to minimize the number of interactions of secondary particles in it, as well as the probability of two beam interactions. For a central Au+Au collision there will be about 350 secondary hadrons (200 of them charged) and about 40 photons from π^0 decay (see Table 3.1). We take the cross-section for hadrons interacting with gold as $1.9 \cdot 10^{-24}$ cm^2. This gives about 0.1 secondary hadronic interactions. The target thickness is 0.009 radiation lengths. Hence there will be about 0.4 photon conversions in the target on the average. Interactions in the beam pipe and in the gas are less serious than those in the target since they will easily be recognized in the TPC. We estimate that for the above central event there will be approximately one secondary interaction in the beam pipe and field cage, and another in the gas, while there will be an average of 0.2 photon conversions in the beam pipe and field cage, and 0.7 in the gas. These values are all acceptable.

At a collision rate of 10^3/sec there is an 8% probability that one or more additional events will occur during the $40\mu s$ preceding or following the TPC trigger event. These will be seen in the TPC data, where the additional events will reconstruct to displaced vertex locations. If the vertices are much closer than 1 cm (±200 ns) it will be difficult to separate them. However, there are many opportunities to suppress such events in the trigger or to tag them in the readout, to reduce the probability of an unrecognized second interaction in the target to less than $2 \cdot 10^{-7}$.

8.2. Data Transfer and Storage

The large amount of information collected by the TPC presents formidable problems for data transfer, storage, and analysis.

Consider the information associated with one central Au+Au event. The TPC has about 25,000 pads and 200 time bins for each.[†] There are thus 5,000,000 pixels to be read out. Obviously suppression of zeros will be necessary. A single track falls in a maximum of 150 time bins and for each time bin signals will be generated on 4–9 pads (we will assume 6.25 pads on the average). The number of non-zero pixels to be read out is therefore about $200 \times 150 \times 6.25$, i.e. 187,500, for

---

[†] These time bins of 200 ns each correspond to a drift length of 1 cm, which is about equal to the FWHM of longitudinal diffusion for tracks near the target position. In the absence of dE/dx fluctuations this optimizes the accuracy of the z measurement. However, such fluctuations are significant and can cause significant errors in the transverse measurement [Bar 82]. In order to record sufficient information to make the necessary corrections it may be necessary to increase the sampling rate by a factor of about two, as was done for PEP-4, ALEPH, and DELPHI. A detailed analysis for EOS has not yet been carried out.

a central Au+Au event with 200 tracks. After zero suppression, each pixel will require two 32-bit words (8 bytes) including 23 bits for identification, 10 bits for the (non-linear) ADC, and overhead. An analogous calculation for the wires yields 80,000 pixels, for a total of 267,500 non-zero pixels. Allowing for a possible increase in the time sampling rate, we may have as many as 1,000,000 32-bit words (4 Mbyte) per event.

Fastbus is advertised as having a capacity of 10–30 MHz of 32-bit words. We know of no one who has exceeded the lower of these figures, so we adopt it. The data rate is then 40 Mbyte/s, limiting us to a rate of 10 Hz for central Au+Au events, assuming infinite bandwidth for source and sink.

Three possibilities have been considered for data storage: optical laser disks, 6250 BPI magnetic tapes and magnetic disks.

(*a*) Optical laser disks have considerable potential as a storage medium (2 Gbyte/disk), but data transfer is slow (250 Kbyte/s). It is by no means certain to what extent future improvements in this technology will change the situation.

(*b*) One 6250 BPI tape can store data at 800 Kbyte/sec in streaming mode and has a capacity of 140 Mbyte. These are both serious limitations. We will focus on Au+Au central collisions, where it will take 5 seconds to record one event, and where the tape will hold 35 events. Even at this slow rate, the tape would have to be changed every 3.5 minutes (allowing for the 6-second pulse rate of the Bevalac and one event per pulse).

(*c*) A fixed magnetic disk can accept information at about 2 Mbyte/s, i.e., one event every 2 seconds, and it can store 2 Gbyte, or 500 events. One disk will be filled in 50 minutes at one event per Bevalac pulse. However, this can only be used as temporary storage, and backup on to tape will be necessary. We estimate that it takes 90 min to back up a disk on to magnetic tapes (using tape accelerator technology). Thus three disks operating in parallel would be needed. The end product would still be about one 6250 BPI tape every 3.5 minutes, containing 35 central Au+Au events. Optical laser disk storage (one disk every 50 min) would be greatly preferable, but the slow write speed would still require several magnetic disks in parallel.

8.3. Data Analysis

Reducing the amount of information to be transferred per event would be valuable to reduce the amount of storage needed and, more important, to create the capability to record several events per one-second-long Bevalac pulse. Some on-line data reduction either in hardware or in software will certainly be considered to devise intelligent triggers for the TPC and/or to make selective read out of events. Major efforts along these lines would require experience with the detector and with event analysis prior to implementation.

Data analysis consists of the many processes that have to be carried out before an event is specified in terms of individual particles, each identified and having a measured momentum. These processes include track recognition, extraction of position coordinates and dE/dx along the track, momentum determination and particle identification. There are many corrections to be made for relative calibration of electronic channels, non-linearities, variations of pressure and temperature, electron attachment, etc., which can be made at the beginning of the analysis, and others such as corrections that depend on the angle at which a projected track crosses a wire, or on dE/dx fluctuations, that may need an iterative approach. We adopt an estimate of the analysis rate from the ALEPH collaboration: 0.2 s/track [Ma 86] using a VAX 11/780 computer, and a linear dependence on the number of tracks per event.

The assumption of a linear dependence is appropriate for any continuous tracking detector. Once a track has been found its analysis proceeds by steps along the track until its end, or else until analysis is no longer possible. Our streamer chamber experience is a good guide: there we have found that for particle multiplicities up to 200 or more measurement time is approximately proportional to the number of tracks. At high multiplicities extra time is required to disentangle close tracks, but this is a small part of the total. With streamer chambers, the response to situations of increasing complexity, where linearity of measurement time begins to break down, has been to improve the chamber resolution by use of image intensifiers, lower voltages, etc., until the problem is linear again. The EOS TPC is a further continuation of this development, designed for good track separation over most of its volume. It will be necessary to resort to least-squares fitting for track separation less than 10% of the time. Of course, it will always be possible by additional investment of analysis time to extract some more information. However, such further analysis will give rapidly diminishing returns, and would not be undertaken except in the most unusual situations.

The ALEPH estimate yields 40 seconds for the analysis of a 200-track event, using a VAX 11/780. We do not have a firm basis for modifying this number. On the one hand, faster computers are already available, and several analysis computers could be operated in parallel. On the other hand, achieving such speeds implies a thoroughly well organized, optimized, and standardized analysis procedure which will take a great deal of effort for us to develop. In considering these questions we have found that the problems of data acquisition, storage, and analysis for EOS have a great deal in common with those anticipated for detectors at the SSC [Fi 85]. The study group on computing needs for that project [Ba 84] concluded that an event rate of about one per second would be the maximum that could be utilized.

Based on one event per Bevalac pulse, we estimate that in 7 days of Bevalac beam time we could acquire 100,800 Au+Au central events. These would take about 2 months of cpu time to analyse, and would yield $2 \cdot 10^7$ charged particles, including $1.2 \cdot 10^6$ π^+, $2.4 \cdot 10^6$ π^-, 4000 K^+, 4000 Λ^0, and 200 K^-. An equivalent amount of analysis time for Ar+KCl would yield about the same total number of charged particles, but the yields of created particles would be higher, namely about $4.8 \cdot 10^6$ pions, $1.7 \cdot 10^4$ K^+, $1.7 \cdot 10^4$ Λ^0, and 900 K^-. Such a body of data would surely produce a qualitative advance in our understanding of relativistic nucleus-nucleus collisions.

Acknowledgements

The plan to construct a new 4π-detector to extend the physics of the Streamer Chamber and Plastic Ball originated in a workshop held by the Bevalac Users Association in the summer of 1984, under the chairmanship of A. Sandoval. They recommended construction of "a continuous tracking detector with magnetic field." A subsequent series of meetings within LBL's Nuclear Science Division focussed attention on a time projection chamber supplemented by a time-of-flight array, with the dimensions adopted for this study. Major contributions to these discussions were made by J. Carroll (UCLA), J.W. Harris, P. Lindstrom, A.M. Poskanzer, H.-G. Ritter, L.S. Schroeder, and T.J.M. Symons.

In the preparation of the present report, we have received valuable and essential support from several graduate and undergraduate students who have brought a variety of skills and fresh insights to our effort, as well as congeniality and hard work. We extend our warmest thanks to them: John Biderbost, Stephen Chung, and Choon Kim, of U.C. Berkeley, and Patrick Simon of Michigan State University (now at Princeton University).

We could not have reached this design without extensive reference to the experience of others, or without their ready willingness to pass it on to us. D. Nygren and the many members of the PEP-4 TPC project have never hesitated when we needed help, and we have found their TPC Notes an essential reference source. Other experts who have gone out of their way to assist us are: C.R. Gruhn of LBL, H.J. Hilke, J. May, and F. Sauli of CERN, and S. Majewski of the University of Florida.

In the preparation of the present report, we have received insight on specific technical aspects from R. Jared, W. Mueller and H. Wieman of LBL, and from H.H. Gutbrod of GSI. G. Roche, of LBL, introduced the GEANT program to us. G. Fai of Kent State University and J. Randrup of LBL provided valuable advice on their event simulation program. We have had helpful discussions with A. Ogawa of SLAC conerning planar spark counters.

Martin Wilson, John Ross, and the staff of Oxford Instruments, Ltd., shared their knowledge and experience with us, and performed preliminary design work on the magnet. R. Reimers, of LBL, advised us on location and installation of the detector at the Bevalac.

We are especially grateful to R. Stock and H. Stoecker of the University of Frankfurt for providing inspiration and new ideas over a long period of time. We thank M. Gyulassy of LBL for constantly forcing us to think of the underlying physics.

Finally, we thank the LBL Word Processing Staff, especially Valerie Kelly, for their professional work, as well as their patient willingness to accommodate revision after revision in good spirit.

This work was supported by the Director, Office of Energy Research, Division of Nuclear Physics of the Office of High Energy and Nuclear Physics of the U.S. Department of Energy under Contract DE-AC03-76SF00098.

References

[AA 86] Four recent issues of Physics Reports provide an excellent and up-to-date review of relativistic nucleus-nucleus collisions at Bevalac energies:
L.P. Csernai and J.J. Kapusta, Entropy and Cluster Production in Nuclear Collisions, Phys. Rep. **131**, 223 (1986);
R. Stock, Particle Production in High Energy Nucleus-Nucleus Collisions, Phys. Rep. **135,** 259 (1986);
H. Stoecker and W. Greiner, High Energy Heavy Ion Collisions-Probing the Equation of State of Nuclear Matter, Phys. Rep. **137**, 277 (1986);
R.B. Clare and D. Strottman, Relativistic Hydrodynamics and Heavy Ion Reactions, Phys. Rep. **141,** 177 (1986).

[AB 83] An overview of the Time Projection Chamber Technique is provided by AIP Conference Proceedings **108** (1983), and
R. Madaras and P. Oddone, Physics Today **37**, 36 (August 1984).
Descriptions of the PEP-4 TPC, ALEPH, and DELPHI projects are given in [Ma 78], [Bl 84] and [De 84] respectively.

[Ad 83] M. Adams et al., Nucl. Inst. Meth. **217**, 237 (1983).

[Ai 83] H. Aihara et al., IEEE Trans. Nucl. Sci., **NS-30**, 76 (1983).

[Ai 86] J. Aichelin, A. Rosenhauer, G. Peilert, H. Stoecker, and W. Greiner, University of Frankfurt preprint **UFTP-188/1986** (1986). We thank H. Stoecker for permission to quote extensively from this preprint prior to its publication.

[Al 80] W.W.M. Allison and J.H. Cobb, Ann. Rev. Nucl. Part. Sci. **30**, 253 (1980).

[Am 85a] S.R. Amendolia, Nucl. Inst. Meth. **A235**, 296 (1985).

[Am 85b] S.R. Amendolia et al. Nucl. Inst. Meth. **A239**, 192 (1985).

[Am 86] Amendolia et. al. Nucl. Inst. Meth. **A244**, 516 (1986).

[An 81] D.F. Anderson, IEEE Trans. Nucl. Sci. **NS-28**, 842 (1981).

[Ap 86] R.J. Apsimov et al., Nucl. Inst. Meth. **A241,** 339 (1986).

[As 86] V. Ashford et al., IEEE Trans. Nucl. Sci. **NS-33**, 113 (1986).

[Ba 78] G. Battistoni, E. Iarocci, G. Nicoletti and L. Trasatti, Nucl. Inst. Meth. **152**, 423 (1978).
E. Iarocci, Nucl. Inst. Meth. **217**, 30 (1983).
F. Kagino, A. Abashian, and K. Gotow, Nucl. Inst. Meth. **A245**, 507 (1986).

[Ba 84] J. Ballam et al., "Computing Needs at the SSC," unpublished (1984).

[Bad 82] A. Baden et al., Nucl. Inst. Meth. **203**, 189 (1982).

[Bar 82] A. Barbaro-Galtieri, in "Proc. of Int. Conf. on Instrumentation for Colliding Beam Physics" **SLAC-250**, 46 (1982).

[Bat 82] G. Battistoni, P. Campana, V. Chiarella, U. Denni, E. Iarocci and G. Nicoletti, Nucl. Inst. Meth. **202**, 459 (1982).

[Be 68] P.W. Benjamin, C.D. Kemshall and J. Redfern, Nucl. Inst. Meth. **59**, 77 (1968).

[Be 81] S. Behrends and A.C. Melissinos, Nucl. Inst. Meth. **188** (1981) 521.

[Bl 84] W. Blum, Nucl. Inst. Meth. **225**, 557 (1984).

[Br 84] R. Brockmann et al., Phys. Rev. Lett. **53**, 2012 (1984).

[Br 85] R. Brun et al., "GEANT3 Users Guide," **CERN DD/EE/84-1** (1985).

[Bry 84] D. Bryman et al., AIP Conf. Proc. **108**, 12 (1984).

[Ca 82] M. Calvetti in "Proc. of Int. Conf. on Instrumentation for Colliding Beam Physics" **SLAC-250** (1982).

[Cl 76] A.R. Clark et al., "Proposal for a PEP Facility based on the Time Projection Chamber" (1976).

[De 84] P. Delpierre, Nucl. Inst. Meth. **225**, 566 (1984).

[Do 85] K.G.R. Doss et al., Phys. Rev. **C32**, 116 (1985).

[Er 77] V.C. Ermilova et al., Nucl. Inst. Meth. **175**, 297 (1980).

[Fa 83] G. Fai and J. Randrup, Nucl. Phys. **A404**, 551 (1983).

[Fi 85] A. Firestone, in "Workshop on Experiments for the Relativistic Heavy-Ion Collider," Brookhaven National Laboratory (1985).

[Fu 85] N. Fujiwara, A. Ogawa, Yu. Pestov, and R. Sugahara, Nucl. Inst. Meth. **240,** (1985).

[Ge 77] J.V. Geaga et al., Nucl. Inst. Meth. **141**, 263 (1977).

[Gr 86a] C.R. Gruhn et al., Nucl. Inst. Meth. **A247**, 460 (1986).

[Gr 86b] C.R. Gruhn, private communication (1986).

[GS 86] GSI-LBL Streamer Chamber collaboration, private communication (1986).

[Gy 79] M. Gyulassy et al., Phys. Rev. **C20**, 2267 (1979).

[Ha 49] C.G. Hanna, D.H.W. Kirkwood, and B. Pontecorvo, Phys. Rev. **75**, 985 (1949).

[Ha 50] G.C. Hanna, Phys. Rev. **80**, 530 (1950), and private communication (1953) quoted in the article by D. West [We 53].

[Ha 71] R. Hagedorn, **CERN 71-12**, eq. 7.7 (1971).

[Ha 80] B. Hallgren and H. Verweij, IEEE Transactions in Nuclear Science **NS-27** 333 (1980).

[Ha 81] J.W. Harris et al., Phys. Rev. Lett. **47**, 229 (1981).

[Ha 85] J.W. Harris et al., Phys. Lett. **153B**, 377 (1985).

[Ha 86] J.W. Harris et al., Lawrence Berkeley Laboratory Report **LBL-22003** (1986).

[Hi 83] H.J. Hilke, AIP Conference Proceedings **108**, 196 (1983); A. Peisert, ibid., 208.

[Ka 86] F. Kajino, A. Abashian and K. Gotow, Nucl. Inst. Meth. **A245**, 507 (1986).

[La 80] F. Lapique and F. Piuz, Nucl. Inst. Meth. **175**, 297 (1980).

[Le 82] I. Lehraus in "Proc. of Int. Conf. on Instrumentation for Colliding Beam Physics" **SLAC-250**, (1982).

[Le 83] I. Lehraus, Nucl. Inst. Meth. **217**, 43 (1983).

[Le] Le Croy Research Systems Corporation, System DL-300, Flash ADC.

[Lu 82] T. Ludlam in "Proc. of Int. Conf. on Instrumentation for Colliding Beam Physics" **SLAC-250**, (1982).

[Ma 78] J. Marx and D. Nygren, Physics Today **31**, 46 (Oct. 1978).
R. Jared et al., IEEE Trans. **NS-29**, 57, 282 (1982).
D. Landis et al., IEEE Trans. **NS-29**, 573 (1982).
M. Ronan et al., IEEE Trans. **NS-29**, 427 (1982).
H. Aihara et al., IEEE Trans. **NS-30**, 76, 162 (1983).

[Ma 86] G. May, private communication (1986).

[Mo 82a] C. Mori, M. Uno, and T. Watanabe, Nucl. Inst. Meth. **196**, 49 (1982).

[Mo 82b] C. Mori and T. Watanabe, Nucl. Inst. Meth. **204**, 149 (1982).

[Na 81a] S. Nagamiya et al., Phys. Rev. **C24**, 971 (1981).

[Na 81b] S. Nagamiya, in "Proc. 5th High Energy Heavy Ion Study," **LBL-12652**, p. 141 (1981).

[No 86] R. Novotny, private communication, (1986).

[Og 86] A. Ogawa, private communication, (1986).

[Pa 86] Particle Data Group, Phys. Lett. **170B**, 53 (1986).

[Sa 77] F. Sauli, Principles of operation of MWPC, **CERN 77-09** (1977).

[Sa 80] A. Sandoval et al., Phys. Rev. Lett. **45**, 874 (1980).

[Sa 84] F. Sauli, AIP Conference Proceedings **108**, 171 (1984).

[Sa 86] F. Sauli, private communication, (1986). Much of Section 5.3 is based on a draft report prepared by F. Sauli discussing this and other options which we have considered.

[Schn 82] S. Schnetzer et al. Phys. Rev. Lett **49**, 989 (1982).

[Se 77] J. Seguniot and T. Ypsilantis, Nucl. Inst. Meth. **142**, 377 (1977).

[Sh 84] M. Shapiro, Thesis, University of California, Berkeley, **LBL-18820** (1984).

[Si 79] P.J. Siemens and J.O. Rasmussen, Phys. Rev. Lett. **42**, 880 (1979).

[Va 81] G.J. Van Dalen, TPC-UCR-81-2 (1981);
G.J. Van Dalen, TPC-UCR-82-3 (1982).

[Va 82] G.J. Van Dalen, TPC-UCR-82-1 (1982);
G.J. Van Dalen, TPC-UCR-81-2 (1981).
H. Iwasaki et al., AIP Conf. Proceedings **108**, 214 (1984).

[We 53] D. West, Progress in Nuclear Physics **3**, 18 (1953), ed. O.R. Frisch, Pergamon Press (London).

[Za 84] W.A. Zajc et al., Phys. Rev. **C29**, 2173 (1984).

[3M] 3M Corporation, St. Paul, Minnesota.

LAWRENCE BERKELEY LABORATORY
TECHNICAL INFORMATION DEPARTMENT
UNIVERSITY OF CALIFORNIA
BERKELEY, CALIFORNIA 94720